

Electronic Thesis and Dissertation Repository

9-4-2018 10:30 AM

Hydrogen Production by Photocatalytic Water Splitting Under Near-UV and Visible Light Using Doped Pt and Pd TiO₂

Bianca Rusinque, *The University of Western Ontario*

Supervisor: de Lasa, Hugo, *The University of Western Ontario*

A thesis submitted in partial fulfillment of the requirements for the Master of Engineering Science degree in Chemical and Biochemical Engineering

© Bianca Rusinque 2018

Follow this and additional works at: <https://ir.lib.uwo.ca/etd>

 Part of the [Catalysis and Reaction Engineering Commons](#)

Recommended Citation

Rusinque, Bianca, "Hydrogen Production by Photocatalytic Water Splitting Under Near-UV and Visible Light Using Doped Pt and Pd TiO₂" (2018). *Electronic Thesis and Dissertation Repository*. 5662.
<https://ir.lib.uwo.ca/etd/5662>

This Dissertation/Thesis is brought to you for free and open access by Scholarship@Western. It has been accepted for inclusion in Electronic Thesis and Dissertation Repository by an authorized administrator of Scholarship@Western. For more information, please contact wlsadmin@uwo.ca.

Abstract

Photocatalysis is a promising methodology for hydrogen production. It involves the use of an unlimited source of energy, sunlight, and a semiconductor material to split the water with zero carbon emissions.

This Master's thesis reports high efficiencies in terms of hydrogen production via water splitting using 2.0v/v% ethanol as scavenger, platinum and palladium as noble metals on TiO₂ photocatalysts at three metal loadings (1.0, 2.5 and 5.0wt%). Both near UV and visible light were used in the studies developed. These photocatalysts were synthesized using a sol-gel method whose morphological properties were enhanced due to the presence of soft template precursors. Experiments were carried out in the Photo-CREC Water reactor II. This novel unit offers symmetrical irradiation allowing precise irradiation measurements for macroscopic energy balances. In all cases hydrogen production followed a zero-order reaction.

Optimal quantum efficiencies were achieved under near UV light, reaching a significant 30.8%. The doped TiO₂ photocatalysts were also studied under visible light obtaining a valuable 1.2% of quantum efficiency. In order to achieve this, the prepared semiconductors were photoreduced and activated with near-UV light.

Keywords

Photo-CREC-Water II Reactor, Platinum, Palladium, TiO₂, Hydrogen production, Photoreduction, Visible light, Quantum Yield.

Acknowledgments

I thank God for giving me the strength not to despair in difficult times.

I would like to thank my supervisor Dr. Hugo de Lasa, for offering his expertise, knowledge, support and guidance in the development of this work. I am grateful for his helpful comments, suggestions and constructive criticism throughout this entire project. To Dr. Salvador Escobedo for being my mentor, for sharing with me his valuable knowledge, teachings, for his continuous support, suggestions, collaboration and friendship.

My gratitude to Dr. Pastor Solano for his help, advice and technical support. To my lab coworkers and friends Abdu, Adriana, Amanda, Cesar, Cindy, Imtiaz, Jose, Maureen, Mario, Nicolas, Orelie, Paco, Samira and Sandra. Thank you for your friendship, for offering me advice, and supporting me through this entire process.

I am grateful to my family for their advice, motivation and constant support. Thank you to my Mom and Dad and to my two sisters Michelle and Ashly. Thanks for your never-ending encouragement. I could not be more blessed for having you in my life. To my aunt Vilma for always being there for me and for being the best aunt I could have had. To Myriam Delgado and Julian Acosta for opening the doors of your home and family. Eternally grateful to you.

I would like to thank my boyfriend Aidan Collins for being so supportive, for his many constructive suggestions and very interesting discussions. Thanks for being my best friend and company. To my dear friends Jony, Vanessa and Phillip for their company and valuable friendship.

To my grandma who is with me from heaven and who I will always remember love and carry in my heart.

Table of Contents

Abstract	i
Keywords	i
Acknowledgments.....	ii
Table of Contents	iii
List of Tables	vi
List of Figures	viii
Appendices.....	xiii
Nomenclature	xiv
Chapter 1	1
1 Introduction	1
Chapter 2.....	5
2 Literature Review.....	5
2.1 Hydrogen Production	5
2.2 Photocatalysis	7
2.2.1 Catalytic Cycle.....	7
2.3 Water Splitting	9
2.4 Semiconductor or Photocatalyst	10
2.4.1 Semiconductor preparation	11
2.4.2 Titanium Dioxide (TiO ₂).....	12
2.4.3 Doped Photocatalyst	16
2.5 Light source	17
2.6 Sacrificial Agent	18
2.7 Photocatalytic Reactor	18
2.8 Quantum Yield (QY)	19

2.9	Conclusions.....	21
2.10	Scope of the Research.....	22
	Chapter 3.....	23
3	Equipment, Materials and Synthesis Methods.....	23
3.1	Photo-CREC Water II Reactor.....	23
3.2	Lamp characterization.....	25
3.3	Synthesis Methods	27
3.3.1	Sol-gel Methodology	28
3.3.2	Copolymers	29
3.3.3	Catalyst Preparation	32
3.4	Conclusions.....	35
4	Photocatalyst Characterization.....	36
4.1	N ₂ physisorption.....	36
4.2	Pulse Hydrogen Chemisorption	44
4.3	X-Ray Diffraction	46
4.4	Band gap	50
4.5	Conclusions.....	56
	Chapter 5.....	57
5	Macroscopic Radiation Energy Balance (MREB).....	57
5.1	Methodology	57
5.2	Macroscopic Radiation Balance	58
5.3	Near-UV-light MREB.....	61
5.4	Visible light MREB	63
5.5	Conclusions.....	64
	Chapter 6.....	65

6	Hydrogen Production Yields and By-products	65
6.1	Photocatalytic Mechanism	65
6.2	Hydrogen Production under Near-UV Light	68
6.2.1	Effect of Copolymer P-123 and F-127 on Hydrogen Production	69
6.2.2	Effect of Platinum and Palladium on Hydrogen production.....	71
6.2.3	Effect of Catalyst Concentration on Hydrogen Production	73
6.2.4	Effect of Photo-CREC Water II Atmosphere. Argon and CO ₂	74
6.2.5	Effect of Sacrificial Agent Concentration on Hydrogen Production	78
6.2.6	By-products Formation during the Photocatalytic Hydrogen Production	79
6.3	Hydrogen Production under Visible Light.....	81
6.3.1	Photocatalysts Photoreduction	83
6.4	Conclusions.....	87
	Chapter 7.....	88
7	Quantum Yield (QY) evaluation.....	88
7.1	Effect of noble metals (Pt and Pd) on Quantum Yields under UV light.....	88
7.2	Effect of catalyst concentration on Quantum Yields under Near UV light	90
7.1	Effect of noble metals (Pt and Pd) on Quantum Yields under Visible light.....	92
7.2	Conclusions.....	96
8	Conclusions and recommendations.....	97
8.1	Conclusions.....	97
8.2	Future work.....	98
	Bibliography	100
	Appendices.....	113
	Curriculum Vitae	116

List of Tables

Table 1 Renewable Energy Technologies.....	2
Table 2 Hydrogen production methods.....	5
Table 3 Comparison Homogeneous and Heterogeneous catalysis	7
Table 4 Properties of Anatase, Rutile and Brookite of TiO ₂	13
Table 5 Light sources in photocatalytic water splitting	17
Table 6 Quantum Yield definition in terms of OH [·] radicals and photon absorbed	20
Table 7 Quantum Yield definitions.....	20
Table 8 Quantum Yield for Hydrogen Production	20
Table 9 PCW-II Dimensions.....	25
Table 10 Surface area and pore diameter using templates F-127 and P-123.....	40
Table 11 Surface area and pore diameter using Platinum and Palladium.....	42
Table 12 Pore size distribution range.....	43
Table 13 Chemisorption analysis. Metal dispersion and crystallite size	45
Table 14 Anatase and rutile content in the photoactive materials	49
Table 15 Optical band gap for photocatalyst modified by Pt and Pd	54
Table 16 Absorbed Photon Rates on TiO ₂ Photocatalysts, at Different Metal Loadings, under UV-Light. Notes: Photocatalyst Concentration: 0.15g/L, P _o =8.46E-06 Einstein/s with 96% radiation transmitted through Pyrex glass tube. All reported data are average values of 3 repeats. Standard deviation: ±3.5%.....	61

Table 17 Rate of absorbed photons at different catalyst concentrations under UV-Light. Notes: Photocatalyst: 1.0wt%Pd-TiO ₂ , P ₀ =8.46E-06 Einstein/s with 96% radiation transmitted through Pyrex glass tube. All reported data are average values of 3 repeats. Standard deviation: ±4.0%.....	62
Table 18 Absorbed Photon Rates on TiO ₂ Photocatalysts, at Different Metal Loadings, under Visible light. Notes: Photocatalyst Concentration: 0.15g/L, P ₀ = 9.56E-06 Einstein/s with 96% radiation transmitted through Pyrex glass tube. All reported data are average values of 3 repeats. Standard deviation: ±2.4%.....	63
Table 19 Redox Reactions for Water Splitting over TiO ₂	67
Table 20 Proposed reaction mechanism of CO ₂ reduction	77
Table 21 Quantum Yield for the Pd/Pt-TiO ₂ photocatalyst when using 0.15g/L.	89
Table 22 Quantum Yield for 1.0wt% Pd -TiO ₂ photocatalyst at different photocatalyst concentrations. All reported data are average values of 3 repeats. Standard deviation: ±4.0%.....	91
Table 23 QYs% for Pd-TiO ₂ and Pt-TiO ₂ Photocatalysts at Different Metal Loadings (1.0, 2.5, and 5.0wt%) under: a) Visible light irradiation only, b) Using Near-UV Light followed by Visible Light irradiation. All reported data are average values of 3 repeats. Standard deviation: a) ±3.0% and b) ±2.4%	92

List of Figures

Figure 1 Sources of Renewable Energy in Canada.....	1
Figure 2 Hydrogen energy sources	3
Figure 3 Applications of Titanium Dioxide.....	12
Figure 4 Band gap energies for some common semiconductors materials.....	15
Figure 5 Formation of photogenerated electron-hole pairs under sunlight.....	15
Figure 6 Photocatalytic water splitting with Pt.....	16
Figure 7 Schematic diagram of the Photo-CREC Water II Reactor	24
Figure 8 UV lamp irradiation spectrum	25
Figure 9 Visible lamp irradiation spectrum	26
Figure 10 UV and visible lamp axial distribution.....	27
Figure 11 Hydrolysis and condensation of the copolymer over TiO ₂	28
Figure 12 Schematic diagram of the formation of the synthesized mesoporous TiO ₂	30
Figure 13 Pluronic F-127 structure	31
Figure 14 Pluronic P-123 structure	32
Figure 15 Catalysts preparation according to sol-gel methodology	33
Figure 16 Catalyst Preparation Process	34
Figure 17 BET and BJH. Process description.....	37

Figure 18 N ₂ Adsorption-Desorption Isotherms for Mesoporous TiO ₂ using Pluronic F-127, Calcined at 500°C. a) TiO ₂ , b) 1.0wt%Pt-TiO ₂ , c) 2.5wt%Pt-TiO ₂ and d) 5.0wt%Pt-TiO ₂	39
Figure 19 N ₂ Adsorption-Desorption Isotherms for Mesoporous TiO ₂ using Pluronic P-123, Calcined at 500°C. a) TiO ₂ , b) 1.0wt%Pt-TiO ₂ , c) 2.5wt%Pt-TiO ₂ and d) 5.0wt%Pt-TiO ₂	41
Figure 20 N ₂ Adsorption-Desorption Isotherms for Mesoporous TiO ₂ using Pluronic F-127, Calcined at 500°C. a) TiO ₂ , b) 1.0wt%Pd-TiO ₂ , c) 2.5wt%Pd-TiO ₂ and d) 5.0wt%Pd-TiO ₂	42
Figure 21 BJH pore size distribution plot for 1.0wt%Pd-TiO ₂ -500°C F-127	44
Figure 22 XRD Diffractograms of catalyst doped by Pt. XRD overlapped for comparison. A = anatase, R= Rutile, Pt=Platinum	47
Figure 23 XRD Diffractograms of catalyst with Pd. XRD for anatase, rutile and undoped TiO ₂ are reported as a reference for comparison. XRD overlapped for comparison. A = anatase, R= Rutile, Pd=Palladium	48
Figure 24 XRD Diffractograms for the Pd Doped TiO ₂ after 6h of Photocatalytic Water Splitting. XRD for anatase, rutile and undoped TiO ₂ are reported as a reference for comparison: A = anatase, R= Rutile, Pd=Palladium	50
Figure 25 UV-vis absorption spectra Mesoporous materials at 1.0, 2.5 and 5.0wt%Pt ...	51
Figure 26 UV-vis absorption spectra Mesoporous materials at 1.0, 2.5 and 5.0wt%Pd ..	51
Figure 27 Band Gap Calculation using the Tauc Plot Methodology and the Straight Line Extrapolation for the following Photocatalysts: a) TiO ₂ , b) 1.0wt%Pt- TiO ₂ , c) 2.5wt%Pt-TiO ₂ and d) 5.0wt%Pt-TiO ₂	52

Figure 28 Band Gap Calculation Using the Tauc Plot Methodology and the Straight Line Extrapolation for the following Photocatalysts: a) TiO ₂ , b) 1.0wt%Pd- TiO ₂ , c) 2.5wt%Pd-TiO ₂ and d) 5.0wt%Pd-TiO ₂	53
Figure 29 Effect of metal loading on the optical band gap.....	54
Figure 30 Photo-CREC Water-II Reactor with Optical Fibre Sensors in Place for Transmitted Radiation Measurements	58
Figure 31 Macroscopic radiation balance around TiO ₂	59
Figure 32 Transmitted radiation at different catalyst concentrations. TiO ₂ doped with 1.0wt%Pd.....	62
Figure 33 Hydrogen Reactions Steps using TiO ₂ as Photocatalyst and Ethanol as Scavenger	66
Figure 34 “In Series-Parallel” Reaction Network for Hydrogen Production using Ethanol as Scavenger.....	68
Figure 35 Cumulative Hydrogen Volume using Templates (a) P-123 and (b) F-127 at different Platinum Loadings (1.0, 2.5 and 5.0wt%). Conditions: Photocatalyst concentration 0.15g/L, 2.0 v/v% ethanol, pH=4 ± 0.05 and near-UV Light. Standard deviation: (a) ±5.0% and (b)±4.0%.....	70
Figure 36 Cumulative Hydrogen Volume using Co-Catalysts (a) Pt and (b) Pd at Different Platinum Loadings (1.0, 2.5 and 5.0wt%). Conditions: Photocatalyst concentration 0.15g/L, 2.0 v/v% ethanol, pH=4 ± 0.05 and near-UV Light. Standard deviation: (a)±4.0% (b)±3.0% respectively.....	71
Figure 37 Cumulative Hydrogen Production using 1.0wt% Pd-TiO ₂ at Different Catalyst Concentrations (0.15, 0.30, 0.50 and 1.0 g/L). Conditions: 2.0 v/v% ethanol, pH=4 ± 0.05 and UV Light. Standard deviation: ±4.0%.....	73

- Figure 38 Cumulative Hydrogen Production using xPd-TiO₂ (x=1.0, 2.5 And 5.0wt%) and Under: Two Atmospheres a) argon and (b) CO₂. Conditions: Photocatalyst concentration 0.15g/L, 2.0 v/v% ethanol, pH=4 ± 0.05 and near-UV Light. Standard Deviation: (a) ±3.0%, (b)±3.4% respectively. 74
- Figure 39 CO₂ Production using 1.0wt% Pd-TiO₂ and Under Two Atmospheres: (a) Argon (b)CO₂. Conditions: Photocatalyst concentration 0.15g/L, 2.0 v/v% ethanol, pH=4 ± 0.05 and UV Light. Standard Deviation: (a) ±4.6%, (b) ±3.5%. 75
- Figure 40 CO₂ and CH₄ Volume using 1.0wt% Pd-TiO₂ under a CO₂ atmosphere. Reaction Conditions: Photocatalyst concentration 0.15g/L, 4.0 v/v% ethanol, pH=4 ± 0.05 and UV Light. Standard Deviation: (a) ±4.6%, (b) 4.2%. 76
- Figure 41 Schematic of TiO₂ photocatalyzed reaction for CO₂ photoreduction 77
- Figure 42 Ethanol Volume in the Liquid Phase under a CO₂ Atmosphere using 1.0wt% Pd-TiO₂. Conditions: Photocatalyst concentration 0.15g/L, 4.0 v/v% ethanol, pH=4 ± 0.05 and near-UV Light. Standard deviation: ±6.5% 78
- Figure 43 Hydrogen Volume Using 1.0wt% Pd at 1.0, 2.0 and 4.0%v/v Ethanol. Conditions: Photocatalyst concentration 0.15g/L, argon atmosphere, pH=4 ± 0.05 and UV Light, R= repeat. Standard deviation: ±6.5%. 79
- Figure 44 Hydrocarbon Profiles of a) Carbon dioxide (CO₂), b) Methane (CH₄), c) Ethane (C₂H₄O) and d) Acetaldehyde (C₂H₆) at 1.0wt% Pd. Conditions: Photocatalyst concentration 0.15g/L, 2.0 v/v% ethanol, argon Atmosphere, pH=4 ± 0.05 and UV Light. Standard Deviation: (a)±4.1%, (b) ±4.7%, (c) ±5.1%, (d) ±6.3%. 80
- Figure 45 Ethanol Changes with Irradiation Time. Conditions: Photocatalyst concentration 0.15g/L, argon atmosphere, 2.0 v/v% ethanol, pH=4 ± 0.05 and UV Light. Standard deviation: ±3.0%. 81
- Figure 46 Cumulative Hydrogen Volume Produced when using Co-Catalysts (a) Pt and (b) Pd at Different Loadings (1.0, 2.5 and 5.0wt%). Conditions: Photocatalyst concentration: 0.15g/L, 2.0 v/v% ethanol, pH=4 ± 0.05 and visible light. Standard deviation: ±3.0% ... 82

- Figure 47 Cumulative Hydrogen Volume using Co-Catalysts (a) Pt and (b) Pd at Different Platinum Loadings (1.0, 2.5 and 5.0wt%). Conditions: Photocatalyst concentration: 0.15g/L, 2.0 v/v% ethanol, pH=4 ± 0.05, visible light and near-UV photoreduction. Standard deviation: ±2.4% 84
- Figure 48 Byproduct Changes with Irradiation Time: a) Carbon dioxide (CO₂), b) Methane (CH₄), c) Ethane (C₂H₆) and d) Acetaldehyde(C₂H₄O) at 1.0%w/w Pd. Conditions: Photocatalyst concentration: 0.15g/L, 2.0 v/v% ethanol, argon atmosphere, pH=4 ± 0.05 and visible light. Standard deviation: (a) ±7.0%, (b) ±5.5%, (c) ±5.2%, (d) ±6.3%. 85
- Figure 49 Ethanol Concentration Changes with Irradiation Time. Conditions: Photocatalyst concentration: 0.15g/L, argon atmosphere, 2.0 v/v% ethanol, pH=4 ± 0.05 and visible light. Standard deviation: ±3.5% 86
- Figure 50 QY% at various irradiation times under UV light and 0.15g/L of photocatalyst concentration using co-catalysts Pt (a) and Pd (b) at different Platinum loadings (1.0, 2.5 and 5.0wt%). Standard deviation on repeats: ±4.5%. 90
- Figure 51 QY% at Various Irradiation Times using Near-UV irradiation and 0.15, 0.30, 0.50 and 1.00 g/L of photocatalyst Concentrations. Note: a) 1.0wt%-Pd on TiO₂ b) Standard deviation on repeats: ±4.0%. 91
- Figure 52 QY% at various irradiation times using a 0.15g/L of photocatalyst concentration under Visible Light only. Note: Photocatalyst involved Pt and Pd on TiO₂ at Different metal loadings (1.0, 2.5 and 5.0wt%). All reported data are average values of 3 repeats. Standard deviation on repeats: 3.0% 94
- Figure 53 QY% at various irradiation times, under Visible Light, and using a 0.15g/L of photocatalyst concentration. Notes: a) Pt and Pd on TiO₂, studied with different noble metal loadings (1.0, 2.5 and 5.0wt%) and b) Photocatalysts were photo-reduced using Near-UV for 1 hour. All reported data are average values of 3 repeats. Standard deviation on repeats: 2.4% 95
- Figure 54 Lamps Irradiation spectrum: a) Near UV light, b) Visible light 114

Appendices

Appendix A: Eav Average Photon Energy**Error! Bookmark not defined.**

Appendix B: Quantum Yield calculation..... 115

Nomenclature

CO ₂	Carbon dioxide
CH ₄	Methane
C ₂ H ₆	Ethane
C ₂ H ₄ O	Acetaldehyde
c	Speed of light (3.0E8 m/s)
D _p	Pore diameter (cm)
e-	Electron
h+	Hole
h	Planck's constant (6.63E-34 J/s)
E _{bg}	Energy band gap (eV)
E _{av}	Average Energy of a photon (kJ/mol photon)
F-127	Poly (ethylene oxide)/poly (propylene oxide) / poly (ethylene oxide)
H ₂ PtCl ₆	Chloroplatinic Acid
H•	Hydrogen radical
H ₂ O	Water
I(λ)	Intensity of light (W/cm ²)
OH-	Hydroxide ions
OH•	Hydroxide radicals
P-123	Poly (ethylene glycol)-block-poly (propylene glycol)-block-poly (ethylene glycol)
P _o	Rate of photons emitted by the BLB Lamp (einsteins/s)
P _a	Rate of absorbed photons (einstein/s)
P _{a-wall}	Rate of photons absorbed by the inner Pyrex glass (einstein/s)
P _{bs}	Rate of backscattered photons exiting the system (einstein/s)
Pd	Palladium
PdCl ₂	Palladium II chloride
PEO	Poly (ethylene oxide)
Pfs	Rate of forward-scattered radiation (einstein/s)

P_i	Rate of photons reaching the reactor inner surface (einstein/s)
P_{ns}	Rate of transmitted non-scattered radiation (einstein/s)
PPO	Poly (propylene oxide)
P_t	Rate of transmitted photons (einstein/s)
Pt	Platinum
$q(\theta, z, \lambda, t)$	Net radiative flux over the lamp emission spectrum ($\mu\text{W}/\text{cm}^2$)
t	Time (h)
TiO_2	Titanium dioxide
V	Total volume of the gas chamber (5716 cm^3)
W	Weight (g)
wt%	Weight percent (% m/m)

Greek symbols

θ	Diffraction angle, also scattering angular angle (o)
λ	Wave length (nm)
ϕ	Efficient quantum yield (%)

Acronyms

BJH	Barrett–Joyner–Halenda model
BLB	Black Light Blue lamp
BET	Brunauer-Emmett-Teller Surface Area Method
CB	Conduction Band
DP25	Degussa P25 (TiO_2)
MREB	Macroscopic Radiation Energy Balance
PCW-II	Photo CREC Water II reactor
STP	Standard Temperature and Pressure (273 K and 1 atm)
UV	Ultra Violet
VIS	Visible
VB	Valence Band
bg	Band gap
0	Basal state

Chapter 1

1 Introduction

The continuous use of fossil fuels has augmented urban air problems in industrialized cities exceeding the legislated allowable health limits and resulting in numerous pollution related diseases. As well, new technologies are needed to reduce the foreseen incremental global carbon emissions which will reach up to 9.8 billion tons by 2020[1].

Given the above, the world community realizes the necessity of alternative energy sources while providing sustainable lifestyles for its populations[2]. In this respect, some countries such as China, India, USA, Brazil, Nigeria, Indonesia and Canada have already implemented the use of renewable sources of energy, responding to the current environmental problems and energy demands[3]. Specifically for Canada, Figure 1, wind and solar energy have had an important growth in the last few years[4]. According to Natural Resources Canada, 18.1% of Canada's total energy production comes from renewable energy.

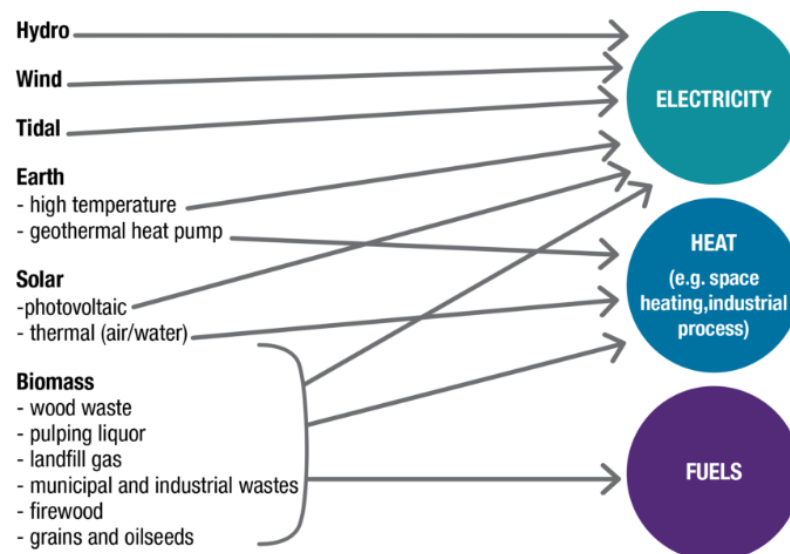


Figure 1 Sources of Renewable Energy in Canada [4]

Renewable energy sources have important intrinsic benefits as well as shortcomings. Their main advantages and disadvantages are listed in Table 1.

Table 1 Renewable Energy Technologies

Type of Renewable energy	Energy source	Advantages	Disadvantages	References
Hydropower	Generated using the mechanical energy of flowing water	-High level of reliability -Very low operating and maintenance costs - Easily adjusted to load changes	-High initial costs -Dependence on precipitation - Flooding of land and wildlife habitat -Displacement of people living in the reservoir area	[5][6]
Solar Power	Conversion of energy from the sun into electricity	-Low operating costs -Reliable source -Little maintenance costs	-Expensive solar panels -Solar energy collection dependent on sunshine	[7][8]
Wind Power	A wind turbine converts the kinetic energy of wind into mechanical energy	-Unlimited wind availability	-Expensive maintenance -Intermittency of wind -Noise, interference with radio and TV signals, and killing of migratory birds	[9]
Geothermal Power	Trap heat and steam form underground to generate electricity	-Continuous operation	-Limited access to geothermal locations -Limited amount of power -Difficult transportation of storage energy	[10]
Biomass	Organic materials can be turned into fuel to supply heat and electricity	-Supports agricultural and forest-product industries -Use of raw materials for products such as fuels and chemicals	-Limited resource as compared to fossil fuels -Land is occupied for growing biomass instead of using for food supply	[11]

Regarding the renewable energy sources described in Table 1 researchers have been recently investigating other clean and emission-free energy vectors that could replace fossil fuels. In this respect, hydrogen has attracted the attention in recent years given its great value. Hydrogen is a most abundant element on earth that could be extracted from a variety of feedstocks[12]. Besides its abundance, hydrogen offers a high calorific value (143 MJ/kg) and clean emissions. Hydrogen when burned with oxygen from air, releases water as the only byproduct [13][14]. While all this is very valuable for hydrogen as an environmentally friendly fuel, hydrogen still offers challenges for both storage and transportation.

Figure 2 presents some primary energy sources that could be utilized to produce hydrogen such as, wind, biomass and sunlight, through different technologies. These technologies could become more competitive than conventional approaches and may be employed to extract hydrogen from water[15]. According to the US Department of Energy, 400 billion cubic meters of hydrogen are produced worldwide per year using the steam reforming of natural gas. This is a high temperature and high pressure catalytic process, with carbon dioxide being a main by-product[16]

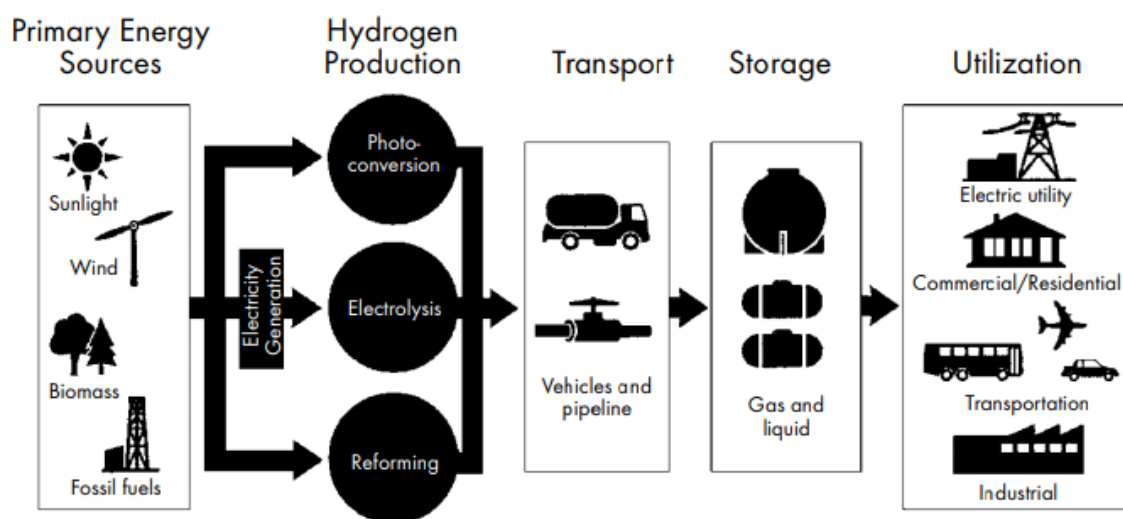


Figure 2 Hydrogen energy sources [16]

Besides reforming, water electrolysis offers another hydrogen production technology. In electrolysis, there is a high energy demand for water splitting. This energy is supplied in the form of electrical energy and can be produced from either fossil fuels or hydropower. Thus, in the case of using fossil fuels the overall process can be considered as a non-sustainable alternative. Water electrolysis presents as well, issues related to efficiency, maintenance costs, robustness, reliability and safety[17].

A promising method for hydrogen production is photocatalysis. Photocatalysis involves the use of sunlight to split water taking advantage of semiconductor generated electron-hole pairs. Today, this process is still non-viable given the low semiconductor efficiency under visible light [18].

In order to improve the photocatalytic water splitting processes, the photocatalysts must meet certain criteria including: a) suitable band gaps to absorb visible light from the sun, b) chemical stability under redox conditions, c) low cost, d) semiconductor recyclability, e) chemical resistance, f) safe hydrogen storage and g) adaptability for large-scale hydrogen production[19][20].

In this context, more research is needed to enhance water splitting[21]. This Master's thesis reports hydrogen formation via water splitting using 2.0v/v% ethanol as scavenger, and noble metal modified TiO₂ photocatalysts under UV and visible light. The prepared semiconductors are activated via near-UV irradiation. These photocatalysts create a significant opportunity to successfully address the challenges of water splitting for hydrogen production

Chapter 2

2 Literature Review

Hydrogen is a key energy carrier that will likely play an important role in the transportation sector by 2050[22]. It is considered as an environmentally friendly energy vector due to its zero CO₂ and zero noxious gas emissions when is produced from water. Hydrogen combustion releases much less pollutants to the atmosphere, than fossil fuels[23].

Through a water splitting process, hydrogen can be produced using water and sunlight as primary resources[24]. In this respect, by applying this technology, people can benefit from the earth's most abundant resource, water, as well as from sunlight radiation at no cost.

2.1 Hydrogen Production

Hydrogen is currently produced via different processes such as electrolysis, thermolysis, water splitting, gasification and biological processes. Table 2 reports the main methods for hydrogen production used today.

Table 2 Hydrogen production methods[25]

Method		Feedstock	Characteristics	References
Electrical				
Electrolysis		Water	Direct current is used to split water into O ₂ and H ₂	[26]
Plasma		Fossil fuels	Natural gas is passed through plasma arc to generate H ₂ and carbon soot	[27]
Thermal				
Thermolysis		H ₂ S	Thermal decomposition of H ₂ S at high temperatures	[28]
Thermo-chemical processes	Water splitting	Water	Convert sunlight into electron/hole pairs that will oxidize water	[29]
	Biomass conversion	Biomass	Fermentative hydrogen thermocatalytic conversion from biomass-based materials	[30]
	Gasification		Conversion of biomass into syngas	[31]
	Reforming		Conversion of liquid biofuels into H ₂	[32]
Photonic				
PV electrolysis		Water	PV panels are used to generate electricity	[33]

Table 2 (continued)

Method	Feedstock	Characteristics	References
Photocatalysis	Water	Water is split into H ₂ by using the electron-hole pair generated by the photocatalyst	[34]
Photoelectrochemical method		A hybrid cell produces current and voltage for absorption of light	[33]
Biochemical			
Dark fermentation	Biomass	Biological systems are used to generate H ₂ in the absence of light	[35]
Electrical + Thermal			
High temperature electrolysis	Water	Electrical and thermal energy to split the water at high temperatures	[36]
Hybrid thermochemical cycles		Electrical and thermal energy are used to drive cyclical chemical reactions	[37]
Coal gasification		Conversion of coal into syngas	[38]
Fossil fuel reforming		Fossil fuels are converted to H ₂ and CO ₂	[39]
Photonic + Biochemical			
Biophotolysis	Biomass & Water	Biological systems (microbes, bacteria, etc.) are used to generate H ₂	[40]
Photofermentation		Fermentation process activated by light	[41]
Artificial photosynthesis		Photosynthetic reaction center proteins used to oxidize water imitating photosynthesis to generate H ₂	[42]
Electrical + Photonic	Water	Photoelectrodes and external electricity are used electrolysis process splitting the water	[43]

Regarding photocatalytic water splitting, the topic of the present research, it has several intrinsic advantages over other hydrogen production techniques. It is a process that can be operated at low temperatures and utilizes durable, stable, efficient and relative inexpensive semiconductors[44]. However, water splitting still has some issues to be addressed such as enhancement of the efficiency photon utilization[45].

2.2 Photocatalysis

The combination of chemistry and catalysis that uses irradiation (ultraviolet, visible or infrared) to accelerate a chemical reaction is denominated “Photocatalysis”[46]. In photocatalysis, a semiconductor or photocatalyst material is utilized to promote chemical change[47]. In nature, one can find photosynthesis as a main example of a photocatalytic process, where chlorophyll acts as a photocatalyst. Chlorophyll captures sunlight converting water and CO₂ into oxygen and carbohydrates[48].

Catalytic processes can be classified into two main branches: a) homogeneous catalysis, where chemical species and photocatalyst are in the same phase (liquid phase generally) and b) heterogeneous catalysis, where catalysts and reagents are in a different phase (solid-gas, solid-liquid, gas-liquid)[49].

Table 3 reports some advantages and disadvantages of homogeneous and heterogeneous catalytic processes.

Table 3 Comparison Homogeneous and Heterogeneous catalysis[50]

Catalysis Type	Advantages	Disadvantages
Homogeneous	<ul style="list-style-type: none"> - Good contact between reactants - Higher selectivity (single activity site) - Simpler and quicker to work with at R&D stage 	<ul style="list-style-type: none"> - Catalyst recovery is very difficult and expensive, after reaction - Poor thermal stability
Heterogeneous	<ul style="list-style-type: none"> - Easy and cheap catalyst separation for reutilization - Good thermal stability 	<ul style="list-style-type: none"> - Lower selectivity (multiple active sites)

As shown in Table 3, one of the main potential advantages of the heterogeneous catalysis is the easy photocatalyst recovery, with this being particularly significant if it is considered the use of photocatalysts doped with noble metals as is the case of the present study[51].

2.2.1 Catalytic Cycle

To describe the photocatalytic reaction for hydrogen production, the process involves the following reaction steps[52][53]:

- a) *Reactant Transportation-Diffusion Step*. Transport of chemical species from the bulk of the fluid to the outer surface of the photocatalyst and from the outer photocatalyst surface to its inner surface via semiconductor pore.
- b) *Reactant Adsorption Step*. Reactant adsorption on a photocatalyst active site.
- c) *Electron/hole Pair Formation*. Photon absorption on a semiconductor surface with the formation of an electron/hole charge pair.
- d) *Photocatalytic Reaction*. Transformation of chemical species via chemical reactions between species and electrons or OH[•] radicals formed on semiconductor holes.
- e) *Product Species Desorption*. Desorption of products formed on the photocatalyst active sites.
- f) *Product Transportation-Diffusion Step*. Transport of formed products from the photocatalyst surface back into the fluid from the inner pore volume.

Thus, in photocatalysis, the availability of active sites is of critical importance as in conventional catalytic processes[54]. Active sites provide a lower energy path for the molecules to reorder their bonds and thus break and form new bonds, necessary for a chemical reaction[55]. In this respect, when the molecules are adsorbed on the surface, they always maintain a link to the active sites, forming reaction intermediates with lower energy barriers to be overcome and form the desired products[56].

However, in photocatalytic processes, the material selected as a photocatalyst should be able to promote the formation of electron/hole pair sites as well. This is a vital requirement for the photocatalytic reaction to proceed[57].

2.3 Water Splitting

Since 1950's, scientist have been trying to find a path to produce hydrogen and oxygen via water splitting. Thermodynamically, water splitting is an “uphill” endergonic process. This is not a spontaneous reaction at room temperature and pressure with a Gibbs free energy of +237.2kJ/mol and a standard redox potential ΔE equals to 1.23 eV[58].

Some of the proposed processes for hydrogen production are expensive and show a very poor efficiency for large-scale use. It has been proposed that major progress could be achieved using catalysts (semiconductors) or biological systems (plants, algae, bacteria) with the latter technology being least developed [59]. Photon activated semiconductors or photocatalysts interact with the substrate (water) and accelerate the photoreaction, producing photoproducts such as hydrogen and oxygen. Photon activation can be achieved via sunlight radiation [60]. However, this reaction may be hindered by chemical equilibrium. A sacrificial agent may be required to allow the photocatalytic reaction to occur, forming the desired photogenerated products such as hydrogen[61].

Thus, some specific steps should be considered for the photocatalytic process with sacrificial agents:

- a) Absorbed photons surpass the energy band gap of the semiconductor material generate excited electron-hole pairs[62].
- b) Photoexcited electron-hole pairs can be separated due to the sacrificial agent presence, allowing the formation of hydrogen with minimum electron-hole pair recombination[63].
- c) Hydroxyl groups from dissociated water, contribute in the h^+ electron vacant site the $OH\cdot$ radical formation and this $OH\cdot$ radical to the conversion of the scavenger[64].

According to the previous steps, unhindered chemical equilibrium for water splitting occurs following the reactions as listed below:

Water Dissociation	$\text{H}_2\text{O} \rightarrow \text{OH}^- + \text{H}^+$	Reaction 1
Semiconductor activation	$\text{Semiconductor} + \text{photon} \rightarrow \text{h}^+ + \text{e}^-$	Reaction 1
OH \cdot Radical Formation	$\text{OH}^- + \text{h}^+ \rightarrow \text{OH}\cdot$	Reaction 2
H \cdot Radical Formation	$\text{H}^+ + \text{e}^- \rightarrow \text{H}\cdot$	Reaction 3
Consumption of OH Radical	$\text{OH}\cdot + \text{organic scavenger} \rightarrow \text{CO}_2 + \text{H}_2\text{O}$	Reaction 4
Consumption of OH Radical	$2\text{H}\cdot \rightarrow \text{H}_2$	Reaction 5

In summary, to produce hydrogen via water splitting three (3) main components are required:

- a) A semiconductor or photocatalyst
- b) A light source (Photon)
- c) Sacrificial agent (organic species)

2.4 Semiconductor or Photocatalyst

A photocatalyst is a material that is capable of absorbing light and produces electron-hole pairs to accelerate the rate of a chemical reaction. Once the reaction cycle is complete, the photocatalyst is restored to its original state [65].

Mesoporous semiconductors have been considered for use in photocatalysis, given the following [66]:

- a) Favourable semiconductor electronic structure
- b) Adequate properties for light absorption
- c) Adequate electron transport properties
- d) Photo-semiconductor excitation
- e) Adequate for chemical species transport

The transport of chemical species to the active centers of semiconductors occurs via diffusion. Thus, the transport properties in a semiconductor, mainly chemical species diffusion, can be controlled by changing the semiconductor size, and shape of the pore network[67].

The BET (Brunauer-Emmett-Teller) method is typically used for determining pore volume and specific surface area. BET is based on the measurements of adsorption-desorption of N_2 . Semiconductors with small pores provide a large specific surface area, contributing to active dopant particle dispersion[68].

Metal oxides are the most well-known semiconductors given their high stability despite their low efficiency. These oxides can display the strong redox potential needed for water splitting reactions. Many metals have been used for this purpose such as TiO_2 , ZnO , Fe_2O_3 , WO_3 , $BiVO_4$ and $SrTiO_3$ [69][70][71].

In 1978, Fujishima and Honda demonstrated the value of using TiO_2 (rutile) and a platinum counter electrode under ultraviolet irradiation for water dissociation into hydrogen and oxygen. Since then, investigation has been performed in the area of this ground breaking research[72].

2.4.1 Semiconductor preparation

In the preparation of a heterogeneous catalyst, the first step is the production of a porous solid. This porous solid is usually obtained in the form of a gel by precipitation. After gel formation, additional steps include typically, calcination and reduction. It is thus, the precursor gel phase that mostly determines the structure and properties of the final catalyst[73].

Many parameters can be changed in each step of the photocatalyst preparation, using the sol-gel method. Such parameters are for example, texture, composition, homogeneity and structural properties of the formed solids[74]. This provides several advantages over other methods for catalyst preparation just as wetness impregnation given that one can control[75]:

- a) Composition and structure control of the photocatalyst (amorphous or crystalline)
- b) Particle size
- c) Reactivity on active sites with carefully engineered particle sizes
- d) Material synthesis

Given the versatility of the sol-gel method for the mesoporous catalyst preparation, it was adopted for the present study.

Four stages are recommended to be carried out during the sol-gel method: (1) hydrogel formation, (2) maturation, (3) solvent removal and (4) a heat treatment step[76]. Hydrogels are cross-linked polymers, which have three-dimensional open structures, where the primary units are held together either by chemical bonds, hydrogen bonds, dipolar forces or Van der Waals interactions[77].

2.4.2 Titanium Dioxide (TiO₂)

In a photocatalytic water splitting reaction, the semiconductor is key. Up to date, titanium dioxide (TiO₂) has been the most used material due to its stability, resistance to corrosion, cleanliness (no pollutant), availability in the nature and inexpensiveness compared to other semiconductors. This material has been widely used for many applications because of its oxidizing power for degradation of organic pollutants and microorganisms and for its affinity to water[78] (Figure 3).

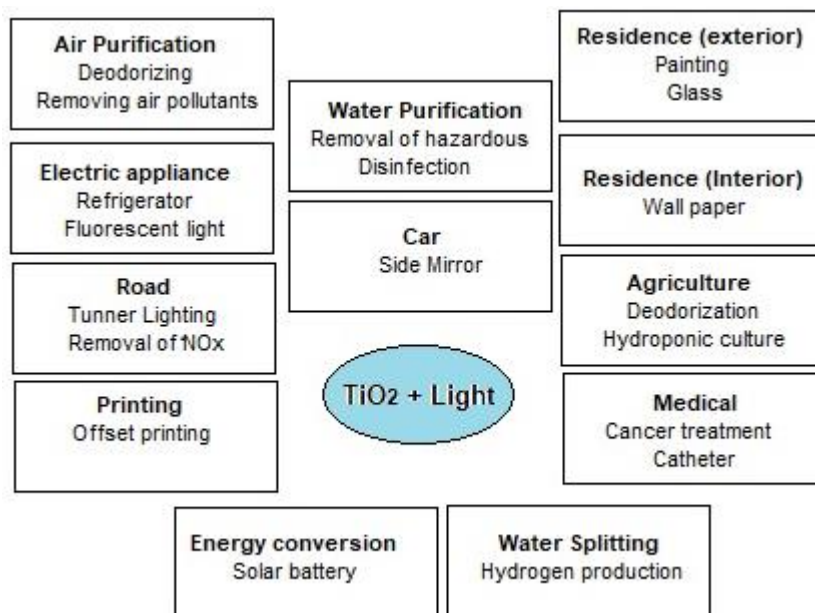
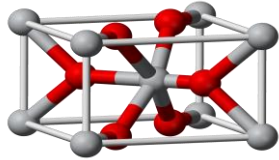
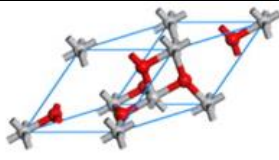
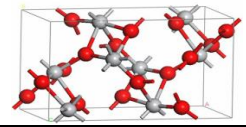


Figure 3 Applications of Titanium Dioxide [79]

2.4.2.1 TiO₂ structures

Titanium dioxide with a typical particle size of 10-15 nm, can be found in three allotropic phases: anatase, rutile, and brookite. Anatase displays superior photocatalytic properties whereas rutile exhibits a high thermodynamic stability. The presence of these three forms of TiO₂ is mainly determined by the synthesis method[80]. For instance, TiO₂ semiconductors may provide enhanced band gaps, refractive indexes and rates of charge transfer across interfaces, favouring photocatalytic activity according to the preparation method[81]. In all these respects, it appears that the anatase phase is the most suitable phase for water splitting. Table 4 shows some properties of these crystalline TiO₂ phases

Table 4 Properties of Anatase, Rutile and Brookite of TiO₂ [82]

Properties	Crystal Structure	Band Gap (eV)	Density (g/cm ³)	Refractive index(η_D)	Structure
Rutile	Tetragonal	3.05	4.27	2.609	
Anatase	Tetragonal	3.23	3.89	2.488	
Brookite	Orthorhombic	3.26	4.12	2.583	

2.4.2.2 Porosity

The surface properties of TiO₂ have a great influence on the semiconductor photocatalytic activity. Grain size, crystallization morphology, surface area and porosity among surface properties are the most important one[83]. The most common classification applied to pores in porous materials is related to their size, which is defined as the distance between opposite pore walls (width, d_p). Depending on their sizes, pores can be classified as ultramicropores ($d_p < 0.7\text{nm}$), micropores ($d_p < 2\text{ nm}$), mesopores ($2\text{nm} < d_p < 50\text{nm}$) and macropores ($d_p > 50\text{nm}$)[84].

Researchers agreed that mesoporous TiO_2 has a better performance in terms of catalytic activity due to its high specific area and uniform pore diameter. This is the result of the great influence of the TiO_2 pore structure on the adsorption of electrons, reagents and products on the surface area. Small pores contribute with a high specific surface area and therefore provide in principle, a better support for active metal sites[85].

Improving the photocatalytic activity of a semiconductor demands close control of the semiconductor pore morphology and of the size of the pores. Some polymers such as Pluronic® F-127 and Pluronic® P-123 which are formed by chains of ethylene oxide and propylene oxide, can contribute to TiO_2 synthesis as soft templates¹. These photocatalyst templates optimize the pore structure network during semiconductor preparation, enhancing pore size distribution and shape[86]. These polymeric templates will be object of study for the production of hydrogen and will be discussed in more detail in the following chapter.

2.4.2.3 Band gap

One of the most important properties of a photocatalyst, is its band gap. This energy level in a semiconductor is established by considering the difference between the top of the valence band (VB) and the bottom of the conduction band (CB). [87]. Then, the accurate band gap should be satisfied for the material to exhibit metallic conductivity. Band gap conductivities are shown in Figure 4.

¹ The soft template does not have a fixed rigid structure. It is easy to build and remove and is mostly used to produce various size, sharp structure of nanomaterials

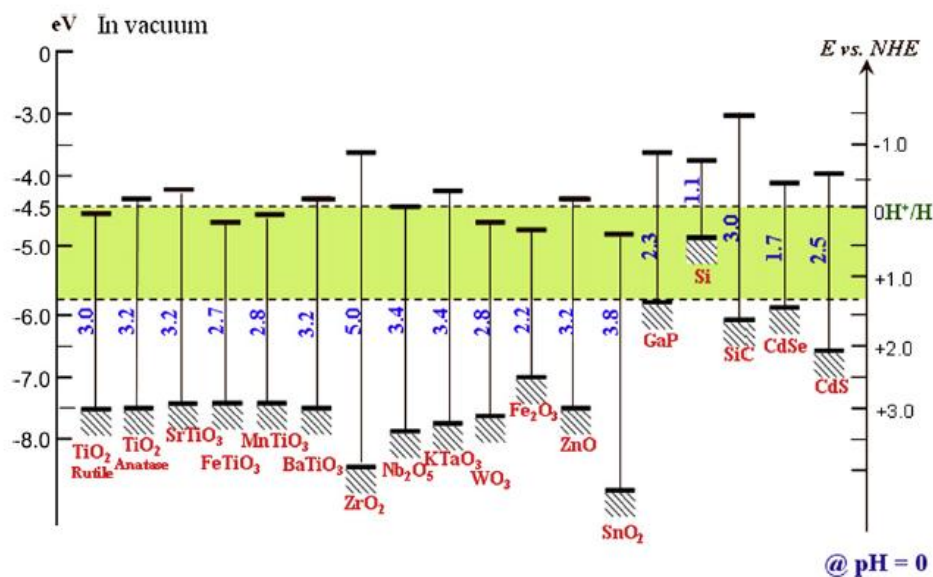


Figure 4 Band gap energies for some common semiconductor materials [88]

The photocatalytic properties of TiO₂ are derived from the generation of electron-hole pairs, which take place once the absorption of light has occurred at a specific band gap. The created holes in the VB are diffused onto the TiO₂ surface and react with the adsorbed water, producing hydroxyl radicals (OH[•]). These (holes + OH[•] radicals) oxidize the closest organic molecules on the TiO₂ surface. Furthermore, the electrons in the CB are reduced by reacting with the oxygen present to derive superoxide radical anions (O₂^{•-})[89].

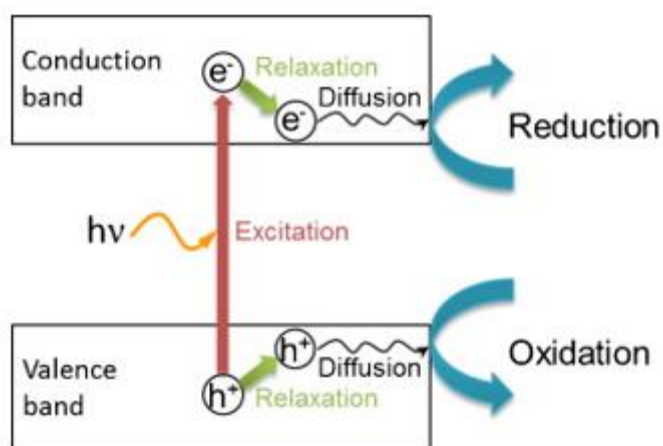


Figure 5 Formation of photogenerated electron-hole pairs under sunlight [90]

2.4.3 Doped Photocatalyst

The elemental doping of a photocatalyst refers to a semiconductor modification on the catalyst surface using a co-catalyst. This co-catalyst can be either a noble metal, a metal oxide or a metal hydroxide as well as a sensitizer using plasmonic materials. These elements increase the efficiency of the hydrogen evolution reaction, narrow the band gaps and improve the optoelectronic semiconductor properties. Their use could allow the activation of the TiO_2 by visible spectrum photons[91].

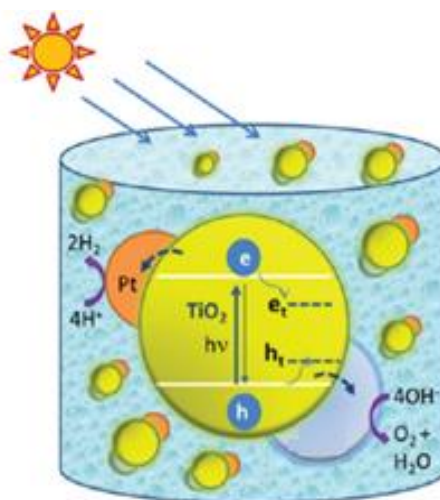


Figure 6 Photocatalytic water splitting with Pt [92].

Semiconductors are in principle based on their ability for both oxidation and reduction. They enable in principle the production of hydrogen and oxygen given the unfavourable thermodynamics of the water splitting reaction. In this respect, co-catalysts such as Pt, Pd, Ni, Ru, Rh, Ir and others, create additional active sites, facilitating the water splitting process, as shown in Figure 6[93].

Platinum and palladium, among other metals, have a lower Fermi level² compared to TiO_2 itself. This yields an effective transference of electrons to metal sites, in the CB level. This

² Fermi level is the term used to describe the top of the collection of electron energy levels at absolute zero temperature.

process decreases the recombination rate between the electrons and the holes, leading to enhanced photocatalytic reactions [94].

Palladium is a very attractive alternative to platinum. Pd displays a similar stability to the Pt but at much lower cost which is about 1/5 of the one for platinum. In the present work, both noble metals, Pt and Pd will be used to dope TiO₂ and analyze their effect on hydrogen production.

2.5 Light source

For semiconductor electron excitation, is required a short wavelength ultraviolet irradiation (250 – 350 nm). Most of the sun radiation is however, in the 400 nm to 650 nm range (visible light range), with the near-UV range only being a small fraction. Thus, the water splitting reaction does not happen naturally under these conditions[95].

Thus, improvements to the water splitting process are required in order to achieve better sunlight utilization efficiencies. With this end new photocatalysts are being considered as shown in Table 5. As well, new photoreactors are engineered to irradiate a large catalyst surface area uniformly and to avoid internal and external diffusion transport phenomena[96]. In this process, a light source adequate to promote the electron-hole pair formation is selected.

Table 5 Light sources in photocatalytic water splitting [97]

Photocatalyst	Light source	Wavelength (nm)
Pt, Cr, Ta on TiO ₂	Visible light	>420
Cu-Ga-In-S on TiO ₂	300W Xe	385- 740
Pt/C-HS-TiO ₂	Visible light	400-650
Pt-TiO ₂	Xe	320-400
Rh-La-SrTiO ₃	300W Xe	>420
Ni/ CdS/ C ₃ N ₄	300W Xe	>420
Au-TiO ₂	Visible light	>420
SrTiO ₃ :La,Rh/Au/BiVO ₄ :Mo	300W Xe	>420
CoO _x -B/TiO ₂ -TaON	150W Xe	>400
MoS ₂ /CuInS ₂	300W Xe	>420

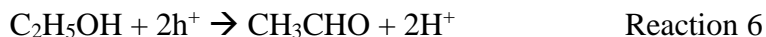
Regarding visible light lamps for water spitting, several types have been used such as 150 W Xenon arc, 300W Xenon cut-off filter and solar simulated radiation equipment with 300W and 15W mercury lamps. Concerning UV and visible light lamps, two types are used in this study, a 15 W BLB (Black Light Blue) for near UV and 15W Hg for Visible light, the BLB lamp has been used before according to the technical literature [98].

2.6 Sacrificial Agent

Heterogeneous photocatalytic hydrogen production has low efficiency due to the recombination of electro-hole pairs. In order to reach higher yields of hydrogen, electron donors are needed to perform as sacrificial agents preventing the mentioned recombination. Common sacrificial agents include methanol, triethanolamine, ethanol, acids and inorganic compounds[99].

Ethanol, as one of the most investigated sacrificial agents, provides high quantum efficiencies and will be used in this work as scavenger. The use of ethanol as a sacrificial agent is advantageous given that it can be easily produced from renewable biomass (fermentation processes), making it available and inexpensive. It is effective when it is used at low concentrations, due to the indirect oxidation of the hydroxyl radicals[100].

On the other hand, using this ethyl alcohol involves the formation of acetaldehyde as well as acetic acid as by-products during the generation of hydrogen via H^+ reduction following the below reactions[101].



2.7 Photocatalytic Reactor

Specific equipment is required for hydrogen production at room temperature and close to ambient pressure using photocatalysis as follows[102]:

- a) The glass section must be made with high UV and visible light transmittance materials. The borosilicate glass used has a transmittance above 90% with an absorption cut-off wavelength of 285 nm where the reaction can be carried out under low or room temperature.
- b) The fluid must be transparent to UV or visible light. Thus, the photocatalyst is the only phase absorbing radiation media.
- c) The various photoreactor materials shall be resistant to the chemicals used (e.g. ethanol) as well resistant to acid pH in the range of 4 to 7.
- d) The selected photocatalytic reactor has to be of the slurry type with the photocatalyst being uniformly suspended. It must have a high surface/volume reactor ratio and limited fouling effects.

To comply with these conditions for hydrogen production, a unique photoreactor unit designated as Photo-CREC Water II Reactor, was designed and developed at the Chemical Reactor Engineering Center (CREC)-UWO[103] . In Chapter 4, additional information about the technical characteristics of this unit is provided.

2.8 Quantum Yield (QY)

Photocatalytic reactors and photocatalysts can be ranked using a photonic efficiency equation as shown in Equation (1).

$$PE = \frac{\text{Rate of reactant molecules transformed}}{\text{Rate of incident photons}} \quad \text{Equation 1}$$

For the photoconversion of organic species in air and water, one can consider a quantum yield (QY) parameter. The quantum yield is defined as the rate of hydroxyl radicals ($\text{OH}\cdot$) consumed over the number of photons absorbed by the photocatalyst (Table 6). It describes the photochemical activity and the utilization of absorbed photons[104].

Table 6 Quantum Yield definition in terms of OH[•] radicals and photon absorbed[103]

Quantum Yield (QY)	$\frac{\text{No. of Consumed OH}^\bullet \text{ radicals moles}}{\text{No. of photons absorbed by the catalyst (Pa)}}$
--------------------	--

Some authors preferred a different QY parameter definition, as described in Table 7. However, the QY should be based on an assessment of photons absorbed instead of an efficiency calculation of incident photons[105]. This makes of the QY a more mechanistically meaningful parameter.

Table 7 Quantum Yield definitions [106][107]

Primary Quantum Yield	$\frac{\text{No. of pollutant molecules degraded from a primary process}}{\text{No. of photons absorbed}}$
Overall Quantum Yield	$\frac{\text{No. of pollutant molecules from a primary and second process}}{\text{No. of photons absorbed}}$
Apparent Quantum Yield	$\frac{\text{No. of pollutant molecules degraded}}{\text{No. of photons absorbed}}$
Global Quantum Yield (QE)	$\frac{\text{No. of pollutant molecules degraded from a primary process}}{\text{No. of photons entering the reactor}}$

For hydrogen production, a specific quantum yield can be considered as described in Table 8:

Table 8 Quantum Yield for Hydrogen Production[108]

Theoretical QY based on the moles of H ₂ produced	$QY_{H_2} = \frac{\text{moles of H}_2 \text{ produced}}{\text{moles of irradiated photons}}$
Overall QY for H ₂ production	$QY_{H^\bullet+OH^\bullet} = \frac{\text{moles of H}^\bullet + \text{moles of OH}^\bullet}{\text{moles of photons}}$
QY in terms of the moles of H [•] radicals produced or two times the moles of H ₂ produced	$QY_{H^\bullet} = \frac{\text{moles of H}^\bullet \text{ produced}}{\text{moles of photons absorbed by the photocatalyst}}$

Given the need of providing a mechanistically based analysis for the production of H₂ as attempted in the present study, the QY_{H•} as reported in

Table 8, will be used in the upcoming sections of the present manuscript.

2.9 Conclusions

Based on the above discussion of the technical literature, the following relevant conclusions can be provided:

- a) Significant progress is still required in the design and preparation of noble metal photocatalysts, to achieve high H₂ production efficiencies under UV and visible radiation.
- b) Research is needed to find suitable substitutes for Pt as the photocatalyst doping agent.
- c) Progress is still essential to evaluate the most promising photocatalysts for hydrogen production in the most advanced photoreactors units such as is the case of the Photo-CREC Water II Reactor. This would allow the calculation of macroscopic radiation balances and the rigorous evaluation of Quantum Yields.

2.10 Scope of the Research

Based on the literature, the following goals have been set for the present project Water splitting for hydrogen production using photocatalysis will be studied and addressed:

1. To analyze the impact of soft templates (Pluronic F-127 and Pluronic P-123) on mesoporous TiO₂ morphology and their influence for hydrogen production rates via photocatalysis.
2. To establish the performance of the different photocatalysts when utilizing noble metals on TiO₂ such as platinum and palladium using: a) UV-light and Visible light, b) different photocatalyst concentrations (0.15, 0.30, 0.50 and 1.00 g/L) and c) various metal loadings (1.0wt%, 2.5wt% and 5.0wt%).
3. To analyze the change of ethanol during the water splitting reaction under Argon and CO₂ atmospheres as inert gases.
4. To establish hydrogen production efficiencies using quantum yields ($QY_{H\bullet}$), based on the QY definition of the ratio of the hydrogen production rate over the photon absorption rate. The photon absorption rate will be determined using rigorously established macroscopic energy radiation balances.

Chapter 3

3 Equipment, Materials and Synthesis Methods

In this chapter, the use of the Photo-CREC Reactor II for a photocatalytic water splitting process will be described. The operation of the reactor as well as the function and effect of the light sources placed inside the unit, will be studied. Specific conditions for the operation of this unit, will be selected for this process. Furthermore, the methods to synthesize semiconductor materials, able to more efficiently contribute to hydrogen production will also be analysed.

3.1 Photo-CREC Water II Reactor

The Photo-CREC Water II (PCWII) operates as a slurry batch reactor unit. It is configured with two concentric tubes: an inner tube made from transparent borosilicate (Pyrex) and an outer tube made from opaque polyethylene. The fluorescent lamp is placed inside this inner Pyrex tube. Furthermore, the suspended photocatalyst flows in the annular space between the outer polyethylene tube and the inner Pyrex transparent tube. The PCWII unit is equipped with a storage feed tank where the photocatalyst suspension is always kept sealed under agitation. This tank has two (2) ports for periodic liquid and gas phase sampling[109].

Given that the material selected for the outer tube is opaque polyethylene, this minimizes radiation reflection. The external tube is equipped with seven (7) axially and equally spaced windows for irradiation measurements. The inner Pyrex tube only absorbs five percent (5%) of the UV or visible light emitted by the lamp. It also protects the lamp from the water. The lamp placed inside the Pyrex tube, provides a 15W UV light or 15 W fluorescent visible light[110].

The hydrogen storage/mixing tank is connected to a 60 Hz centrifugal pump which allows liquid recirculation in the Photo-CREC Water II unit concentric channel, where the photocatalytic reaction takes place. An electric circuit provides a 120V single phase to the lamp.

Figure 7 describes the main components of the Photo-CREC Water II unit: a) the Photo-CREC Water II Reactor, b) the centrifugal pump, c) the sealed storage tank, d) the electrical circuit powering the near-UV or visible light lamp.

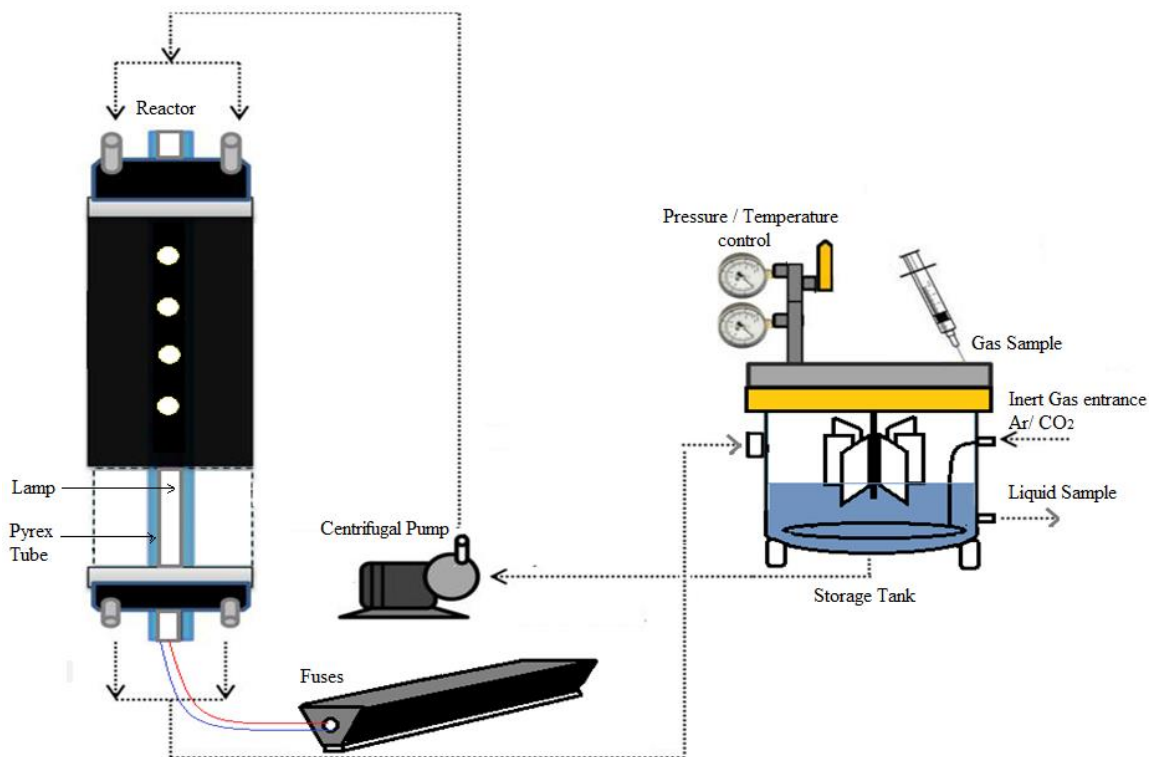


Figure 7 Schematic diagram of the Photo-CREC Water II Reactor[103]

The Photo-CREC Water II allows a well-mixed operation for both the liquid, as well as for the gas phase. This is the case given that the Photo-CREC Water II is equipped with a centrifugal pump as well as a sealed tank with a self-powered device. The Photo-CREC Water II Reactor is equipped with auxiliary ports and gauges to monitor pH, temperature, pressure, flow, as well as to take periodic liquid and gas samples. The sealed storage tank allows one to feed an inert gas such as Argon or CO₂. The centrifugal pump is a class B, 115V, 2.4A, 60 Hz and 3100 rpm unit and the electrical ballast was designed to operate at 120 VAC, 60 Hz and 0.75 A[111].

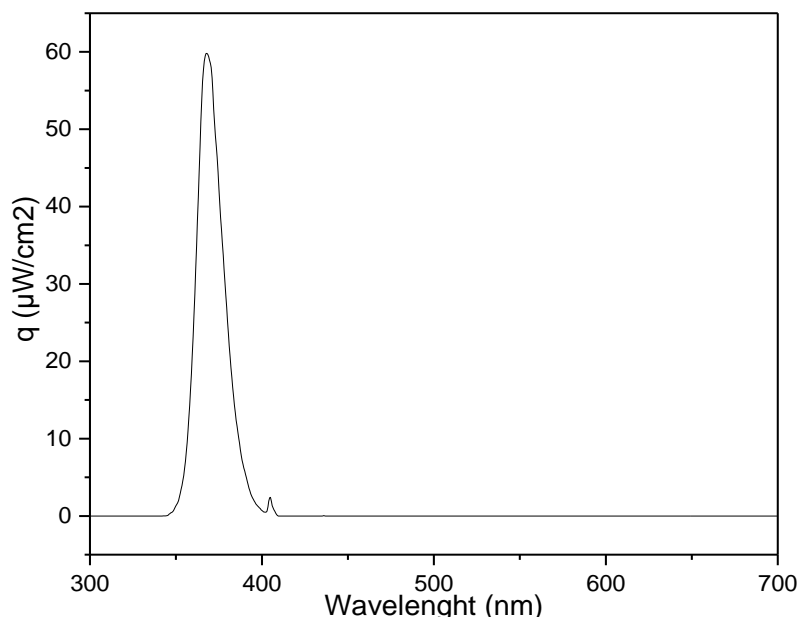
Table 9 PCW-II Dimensions

Component	Height (cm)	Inner radius (cm)	External radius (cm)
Pyrex glass	61	1.505	1.75
External Tube	45	1.75	4.5
Windows	-	-	0.5
H ₂ mixing/storage tank	21	22.5	31
Internal tank impeller	16.5	-	2.25

3.2 Lamp characterization

The emitted radiation spectra of the lamps used in Photo-CREC Water II were established using a Stellar Ney EPP2000-25 spectrometer. The Stellar Ney EPP2000-25 spectrometer was equipped with fibre optics to be able to effect radiation measurements in the 300-800 nm range, at variable distances and various locations of the PCWII unit. This spectrometer unit was also provided with a high speed parallel digitizer interface [112].

Figure 8 reports a typical spectrum measured with the Stellar Net EPP2000-25. One can observe that when using the polychromatic BLB Ushio UV lamp (15 W, 0.305 A, 55V), there is a spectral peak at 368 nm in the 300-420 nm emission range [113]. The observed output power of this lamp was 1.61W with an average emitted photon energy of 325.1 kJ/photon mole.

**Figure 8** UV lamp irradiation spectrum

Similarly, the Stellar Ney EPP2000-25 spectrometer was used to determine the irradiation spectrum of the mercury Philips visible light lamp, as shown in Figure 9. This cool white light lamp possesses a nominal input power of 15 W in the 300-700 nm range with an output power of 1.48W and an average emitted photon energy of 274.46 kJ/photon mole.

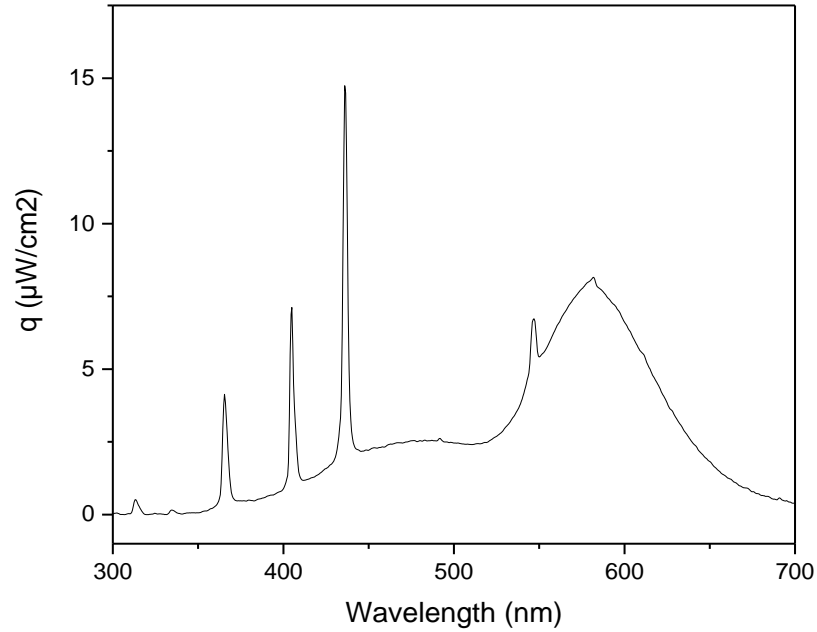


Figure 9 Visible lamp irradiation spectrum

The average emitted photon energy was calculated using the recorded irradiation spectra for both lamps and utilizing the following equation[114]:

$$E_{av} = \frac{\int_{\lambda_{min}}^{\lambda_{max}} I(\lambda) E(\lambda) d\lambda}{\int_{\lambda_{min}}^{\lambda_{max}} I(\lambda) d\lambda} \quad \text{Equation 2}$$

Where,

$$E(\lambda) = \frac{hc}{\lambda} \quad \text{Equation 3}$$

With h being the Planck constant (6.34E-34 J s/photon), c representing the speed of light in a vacuum (3.00E8 m/s²) and λ denoting the wavelength expressed in nanometers (nm) (See Appendix A).

The average photon energy absorbed by the photocatalyst has to be defined using the λ_{\max} or the equivalent E_{\min} (refer to Equation 3) required to supersede the TiO_2 band gap [115].

Regarding the PCWII, the axial distribution of the radiative flux is a parameter of major importance. With this end, axial measurements were carried out using the fibre optic system, the spectrophotoradiometers and PVC black collimators. These black collimators allowed us to consider only the transmitted radiation in the macroscopic radiation balances

Figure 10 reports the near-UV and visible lamp axial radiation distribution. One can observe that the radiation profile shows no significant changes in radiation levels in the central section of the PCWII. On the other hand, significant radiation decay can be seen approaching the endpoints of the lamp[116].

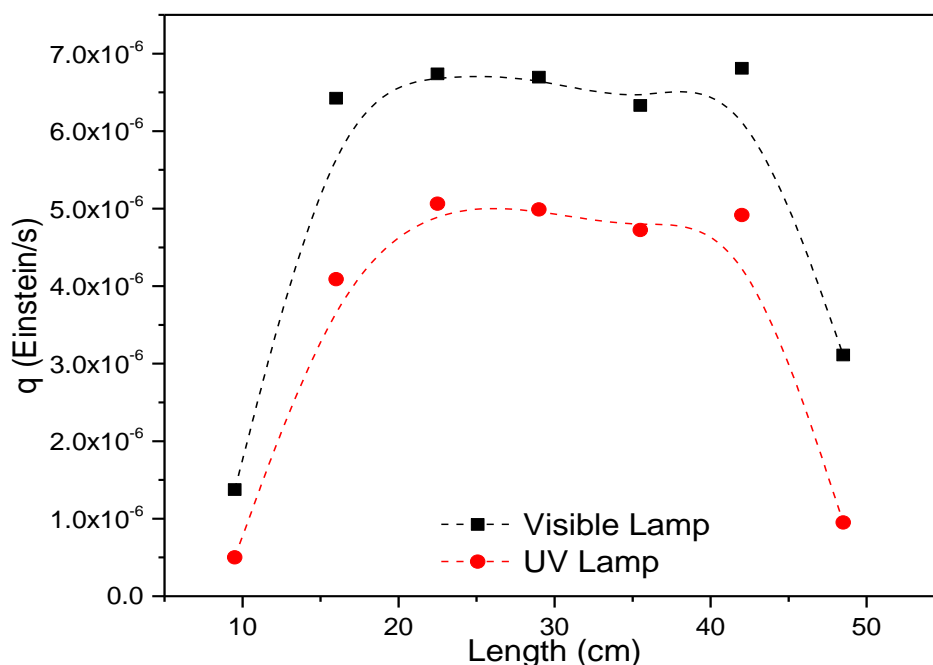


Figure 10 UV and visible lamp axial distribution

3.3 Synthesis Methods

Modifying semiconductor synthesis may lead to improvements in photocatalyst properties such as particle diameter and surface area. These changes may enhance photocatalytic activity. In this respect, a new sol-gel methodology could be one of the best approaches to

address this objective. Likewise, using a new template for photocatalyst preparation could lead to an important advancement in hydrogen production via water splitting.

3.3.1 Sol-gel Methodology

The sol-gel method is based on converting monomers into colloids (sol phase), promoting a gel structure formation [117]. The sol-gel method as shown in Figure 11, is initiated with the hydrolysis of a metal precursor. It is completed with species condensation, creating a 3D gel. The resulting 3D gel can then be subjected to a drying procedure forming a Xerogel[118].

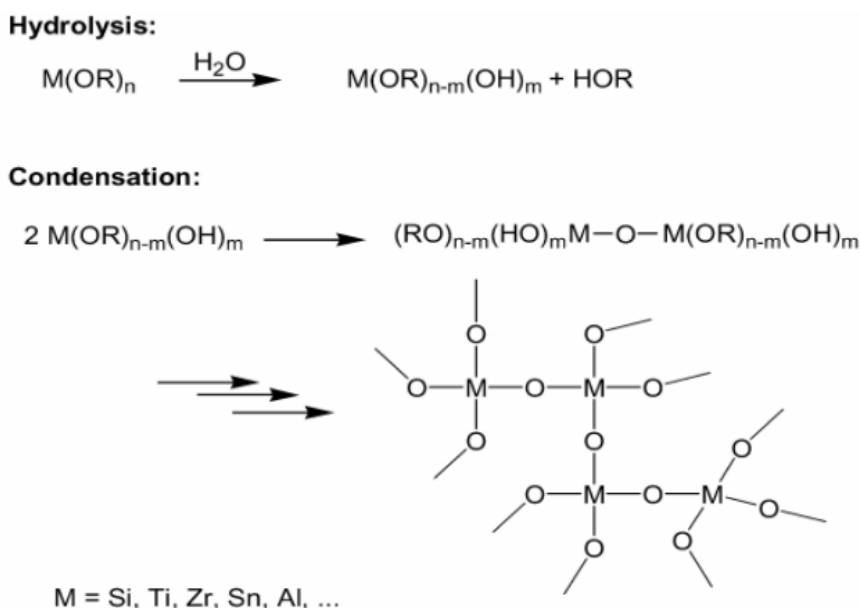


Figure 11 Hydrolysis and condensation of the copolymer over TiO₂

One can certainly use TiO₂ as a metallic precursor for the gel formation. As a result, spiral/linear chains of TiO₆ octahedrals are obtained after hydrolysis. The condensation of these structures leads to crystallite formation during the subsequent thermal treatment. Given that particle nucleation is quite homogeneous during colloidal deposition, this yields a well-controlled particle size, shape, surface area to volume ratio, and porosity[119].

To enhance the photocatalytic activity of the TiO_2 , a copolymer or template can be added to enlarge the surface area of the mesoporous material. This allows the formation of strong chemical bonds between the copolymer and the semiconductor[120]. Thus, the copolymer enhanced sol-gel methodology permits one to control the purity, homogeneity, and morphology of the TiO_2 .

3.3.2 Copolymers

These templates or copolymers can be either anionic surfactants, cationic surfactants or non-ionic surfactants. Cationic surfactants are used to prepare mesoporous silicates at high temperature, whereas anionic surfactants are utilized for aqueous synthesis of mesoporous alumina. Non-ionic surfactants meanwhile, can be employed to prepare disordered wormhole silicas (HMS, MSU) or ordered materials with uniform pore sizes under acidic conditions by sol-gel dip-coating[121].

For the effective preparation of an organized mesoporous structure of TiO_2 , it is important to choose the most suitable block copolymer. There are some copolymers available in the market such as Pluronic® P123 ($\text{PEO}_{20}\text{PPO}_{70}\text{PEO}_{20}$, EO = ethylene oxide, PO = propylene oxide, MW = 5800) and F127 ($\text{PEO}_{106}\text{PPO}_{70}\text{PEO}_{106}$, MW = 12,600). These copolymers are also called “thermoreponsive” as they change their structure with temperature [122].

Non-ionic surfactants are frequently used as templates. Pluronic P-123 and Pluronic F-127³ show a great ability to modify the morphology, porosity, surface area, particle size and crystallinity of the photocatalyst. Furthermore, the use of these templates positively affects the TiO_2 crystalline structure, enhancing the anatase phase, forming 1 to 15 nm crystallites[123]. Pluronic F-127 is used more frequently in the synthesis of spherical pores in a body-centered cubic structure whereas P-123 creates hexagonally ordered cylindrical pores.

³ P and F stand for the physical state of paste and flake

One of the main features of a copolymer is its polarity [124]. Pluronic P-123 and Pluronic F-127 have a central hydrophobic PPO chain and two hydrophilic PEO tails. By combining these copolymers with an organic component (ethanol) and a metallic precursor (TiO_2), the pores are created.

The pore size of a mesoporous material is initially dependent on the hydrophobic core diameter[125]. The organic compound enters the interface between the hydrophilic and hydrophobic chains. It attaches to the hydrophobic core due to the nonpolar nature, initially creating large pores. Therefore, ethanol plays an important role in the generation of a large-pore mesostructured TiO_2 matrix.

Figure 12 describes the formation of a semiconductor material, in this case case being a mesoporous photocatalyst. During the first phase, a hydrophobic block (PPO) is placed in a central location surrounded by the PEO tails (Figure 12a). Then, a second step takes place with PEO tails becoming attached to the TiO_2 in the network. PEO is now in between the PPO core and the TiO_2 matrix (Figure 12b). Following this, the PEO tails coordinate with a fraction of TiO_2 leaving a hybrid outer layer with a dominant TiO_2 composition (Figure 12c). Calcination of the resulting material yields TiO_2 with a mesoporous structure (Figure 12d)[126].

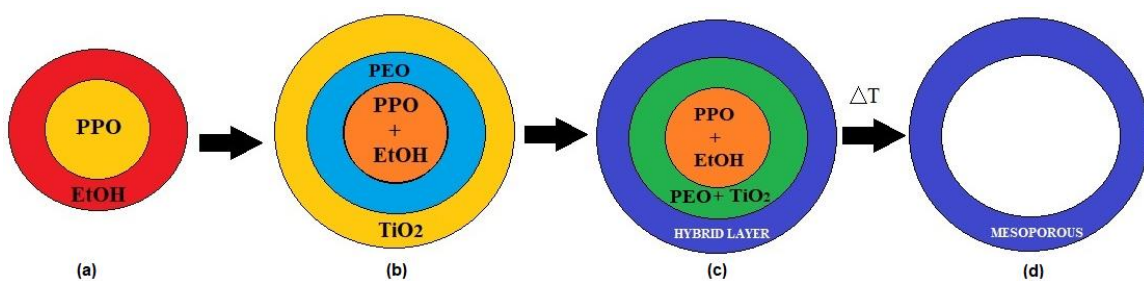


Figure 12 Schematic diagram of the formation of the synthesized mesoporous TiO_2

At these synthesis conditions, ethanol helps with the phase separation process while moving from Figure 12b structure to Figure 12c structure. This may occur given the large entropies and enthalpies for polymerization of the titanium species and ethanol interactions with other species[127].

As a result, micelles of the amphiphilic block copolymer are formed by evaporation-induced self-assembly (EISA) of the solvent (ethanol). This process enriches the surfactant and inorganic species, creating a 3D ordered pore structure at the substrate-liquid level. This results in a well-defined crystalline mesostructured photocatalyst. The thermal treatment of the photocatalyst leads to an ordered mesoporous titanium framework[128].

3.3.2.1 Pluronic F-127

Pluronics or Poloxamers are non-ionic surfactant poly (ethylene oxide)/poly (propylene oxide) / poly (ethylene oxide) (PEO-PPO⁴-PEO⁵) triblock copolymer. Pluronics permit the preparation of thermosensitive hydrogels with important properties being this liquid at low temperatures and solid at higher temperatures[129].

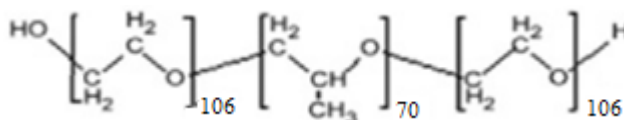


Figure 13 Pluronic F-127 structure

Pluronic F-127 was originally used in the pharmaceutical industry due to the ability of the PEO-PPO-PEO blocks to form “gels” for controlling the drug released. F-127 is also used for the separation of macromolecules such as DNA and proteins[130].

For the first time in 2010, Oveisi used the copolymer F-127 in TiO_2 to control the crystallinity and photocatalytical activity, obtaining a high surface area and an essentially pure anatase crystalline phase [131].

3.3.2.2 Pluronic P-123

Pluronic P-123 is a low-cost copolymer Poly (ethylene glycol)-block-poly (propylene glycol)-block-poly (ethylene glycol).

⁴ Hydrophobic segment. It is 30% of the block copolymer

⁵ Hydrophilic segment. It is 70% of the block copolymer

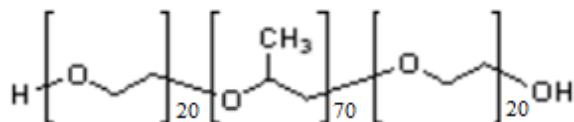


Figure 14 Pluronic P-123 structure

It is commonly used as a surface cleaner, as a defoamers in coatings and water treatment. It can also be used as a lubricant in metalworking, as an anti-foaming agent and as an extender for linear and cross-linked polyesters and polyurethanes. Among its multiple applications, it is used in the preparation and coating of Fe-W-C(O) nanoparticles by sol-gel technique, as well as sacrificial templates to prepare ZnS nanospheres and nanoporous silica[132].

Pluronic P-123 is hydrophobic at temperatures above 288K and soluble in water at temperatures below 288K. It leads to the formation of micelle consisting of PEO-PPO-PEO triblock copolymers[133].

3.3.2.3 Properties

Titanium dioxide is relatively flexible material. When it is combined with the copolymers, it can gain mechanical strength and toughness. Thermal stability could be also obtained[134]. On the other hand, Pluronic F-127 and P-123 may affect the TiO₂ (rutile, anatase, brookite) formed and consequently the crystallographic properties of the resulting TiO₂[135].

The three phases of TiO₂ (rutile, anatase and brookite) have a high refractive index. However, in the near-UV and visual wavelengths, titanium dioxide displays very poor light scattering [136]. The addition of the described polymers does not affect the refractive index of the TiO₂ [137].

3.3.3 Catalyst Preparation

Following the sol-gel methodology, the photocatalyst was prepared according to the steps reported in Figure 15.

Formation	Ageing	Solvents Removal	Thermal treatment
1. Dissolution of a precursor (metallic salt or alkoxide) in a solvent.		6. Drying the gel by removing the solvent	
2. Addition of an acid or base and the copolymer for hydrolysis and condensation	5. Gel Ageing		8. Powder photocatalyst
3. Ph adjustment			
4. Formation of a self-supported gel		7. Xerogel formation	

Figure 15 Catalysts preparation according to sol-gel methodology [138]

Regarding the specific materials used for the synthesis of a mesoporous photocatalyst, the following can be cited: a) Ethanol USP ($\text{CH}_3\text{CH}_2\text{OH}$) from commercial alcohols, b) hydrochloric acid (HCl , 37% purity), c) Pluronic F-127 and Pluronic P-123, d) Anhydrous citric acid, e) Titanium (IV) isopropoxide, f) Hexachloroplatinic acid hydrate ($\text{H}_2\text{PtCl}_6 \cdot x\text{H}_2\text{O}$, 99.9% purity) and g) Palladium (II) chloride (PdCl_2 , 99.9% purity). All the reagents were obtained from Sigma Aldrich.

The sol-gel phase is synthesized at room temperature, with this phase enhancing strong surface interactions between reagents. One should be aware that increasing temperature while the gel is being formed may have a negative impact on the TiO_2 specific surface area, pore size, with anatase grains being converted into rutile. All this decreases photocatalytic activity [131].

Figure 16 reports the detailed process of the catalyst preparation according to Guayaquil et, al proposed methodology[139].

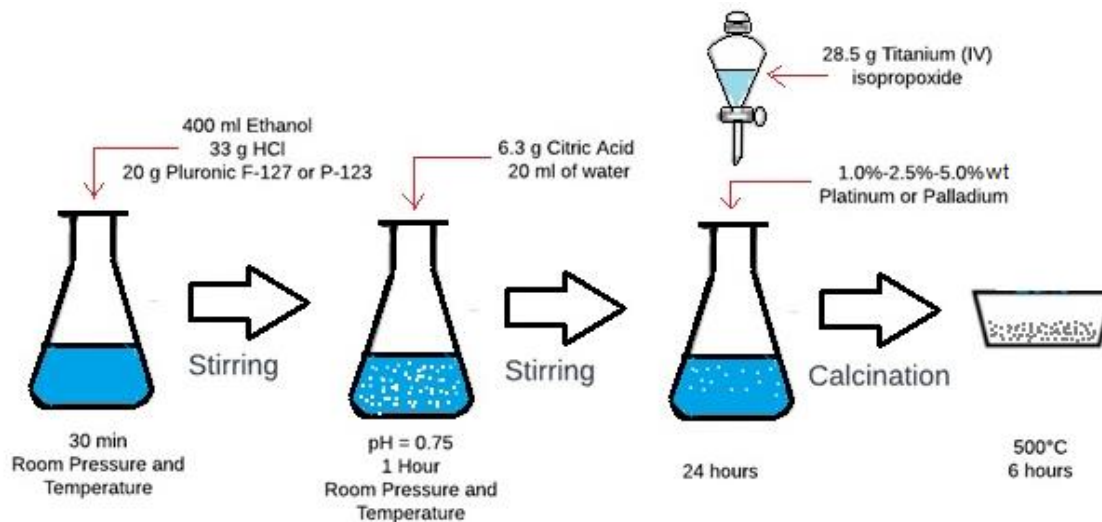


Figure 16 Catalyst Preparation Process

As illustrated in Figure 16, a metallic salt (Titanium isopropoxide) is dissolved in Ethanol, to control the hydrolysis process and the morphology. Ethanol acts a hydrophilic compound at room temperature and becomes attached to the PPO chain of the copolymer. This titanium-rich species behaves as a hydrophobic PEO tail. In order to confirm in a simple manner that titanium isopropoxide was formed, one can check the solubility of this compound in water[140].

Concerning the formation of anatase and rutile, their ratio is acidity dependent. Thus, the acidity of the solution has to be controlled using hydrochloric acid. Furthermore, the acidity of the solution also regulates the hydrolysis rate. Thus, citric acid can be employed to control the pH and to help functionalize the hydrophilic surface TiO_2 chains. This improves the particle binding to the ethylene oxide units (PEO) of the F-127 or P-123. Once the pH is controlled by the addition of both acids, hydrolysis occurs rapidly first, followed by a polymerization at a slower pace.

Regarding the physicochemical changes which take place during the 50-200°C temperature increase, one can notice that water and HCl evaporate. Finally, once 500°C is reached under air atmosphere, the organic base surfactant is removed via calcination.

3.4 Conclusions

The following are the conclusions regarding the materials and equipment section of the present MEdSc thesis:

- a) The Photo-CREC Water Reactor II provides a large irradiated area per unit volume and an effective contact area between the fluid and the photocatalyst.
- b) Near-UV and visible lamps used in this research, are adequate to activate both the Pd and Pt doped TiO₂, in the required spectral range.
- c) Noble metal doped TiO₂ photocatalysts can be synthesized using P-123 and F-127 templates and a sol-gel method. The method considered allowed us to control the purity, homogeneity, morphology, porosity, surface area, particle size and crystallinity of the catalyst.

Chapter 4

4 Photocatalyst Characterization

There are several techniques that can be used for the characterization of solid catalysts. These techniques allow the determination of the surface area, pore size distribution and pore size, phase composition, band gap, metal dispersion and metal crystallite size. These parameters help one to understand the photocatalytic activity of the system, the evolution of the photocatalyst during its preparation and its potential changes during utilization. More specifically and in the context of the present study, the following surface characterization techniques were used: a) specific surface area (BET), b) chemisorption, c) x-ray diffraction and d) UV-vis absorption

4.1 N₂ physisorption

The BET (Brunauer–Emmett–Teller) method is based on the nitrogen physisorption on a porous material. The obtained nitrogen equilibrium adsorption isotherm allows the calculation of the specific surface area (S_{BET}) at a given temperature. During BET, the catalyst is exposed to nitrogen, reaching an adsorption equilibrium between gas and solid phases. An adsorption isotherm is thus generated, as a result of the relationship between the relative vapour pressure and the adsorbed volume of gas [141].

Events taking place during a nitrogen sorption process at adsorption equilibrium, with an increasing P/P_0 , are described in Figure 17. Stage 2 of this figure represents the formation of the nitrogen monolayer, which is at the basis of the BET method. At these conditions with a nitrogen monolayer formed, a resulting sorbed volume of gas can be calculated. This gas sorbed monolayer is proportional to the total combined internal and external surface area.

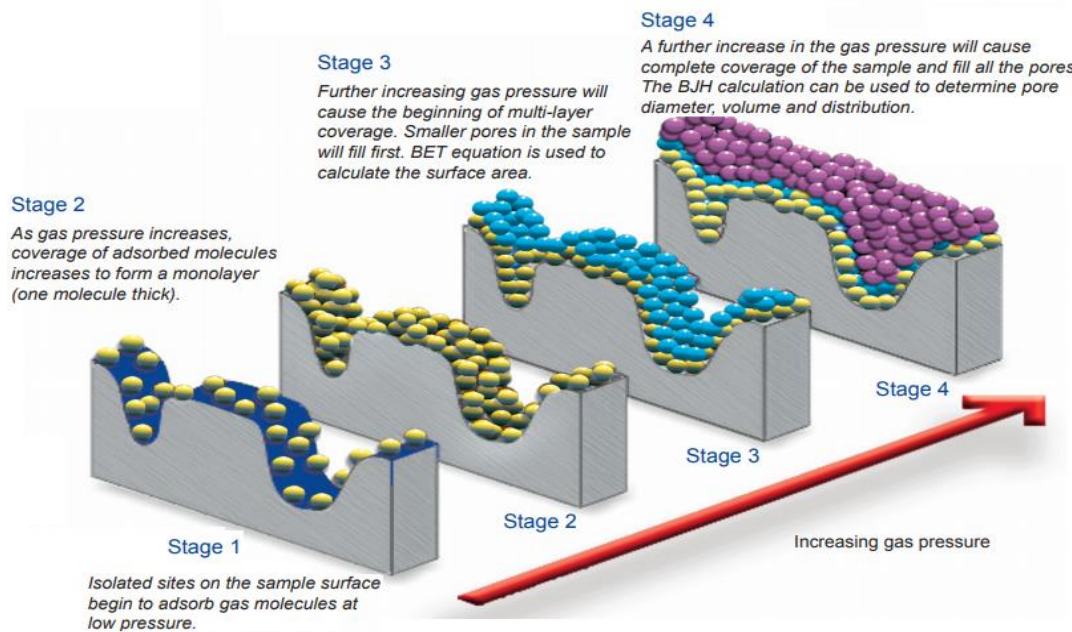


Figure 17 BET and BJH. Process description [142]

In the present study, photocatalyst surfaces areas were determined using a BET surface area analyzer (Micrometrics, ASAP 2010) at -195°C . Each photocatalyst was degassed at 300°C during a period of three (3) hours. Then, the sample was analyzed using nitrogen to generate the adsorption-desorption equilibrium isotherms and establish the isotherm inflection point. With these data, the corresponding surface areas at Stage 2 of Figure 17 were calculated.

The BET surface area is calculated based on the Equation 4:

$$S_{\text{BET}} = \frac{\text{CSA} \times (6.03 \times 10^{23})}{(22414 \text{ cm}^3 \text{ STP}) \times (10^{18} \text{ nm}^2)/\text{m}^2 \times (S + Y_{\text{INT}})} \quad \text{Equation 4}$$

Where,

CSA= analysis gas molecular cross-sectional area (nm^2), S= Slope ($\text{S g/cm}^3 \text{ STP}$) and Y-intercept ($Y_{\text{INT}} \text{ g/cm}^3 \text{ STP}$)

Furthermore, the estimation of the average pore diameter (D_p) was carried out using to BJH method (Barret, Joiyner and Halendaer) with experimental isotherms utilizing the

Kelvin model (Equation 5). The Kelvin equation establishes the P/P₀ relative pressure at which capillary condensation occurs in pores of a given size [143].

$$\ln \frac{P}{P_0} = - \frac{2\gamma V_M}{R_K RT} \cos\theta \quad \text{Equation 5}$$

Where,

P is the equilibrium pressure in atm, P₀ = pressure of vapour in atm, γ = liquid surface tension in N/m, V_M = molar volume of the condensed phase in cm³/mole, R_K = mean radius of curvature of the liquid meniscus in m, R = gas constant and T = temperature in K. For nitrogen, V_M=34.68 cm³/mol and γ =8.72x10⁻³ N/m. The contact angle $\theta=0$ [144][144].

As well, the V_p total photocatalyst pore volume can be calculated with the liquid nitrogen adsorbed at the P/P₀ relative pressure of 0.99 [128].

Figure 18 and Figure 19 report isotherms of type IV for the TiO₂ mesoporous materials studied. At the higher P/P₀ dimensionless pressures, one can observe a hysteresis loop, that shows a different adsorption and desorption isotherm path. This path occurs when pores are filled (adsorption) and pored are emptied (desorption)[144].

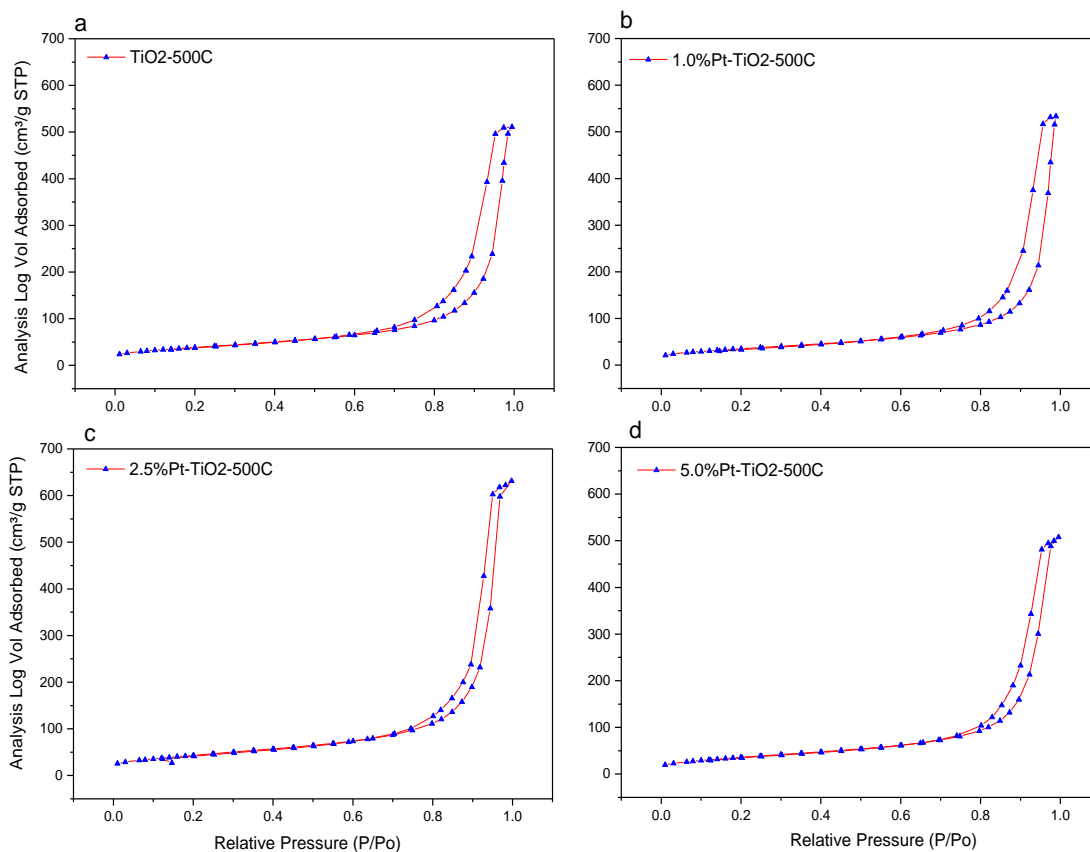


Figure 18 N₂ Adsorption-Desorption Isotherms for Mesoporous TiO₂ using Pluronic F-127, Calcined at 500°C. a) TiO₂, b) 1.0wt%Pt-TiO₂, c) 2.5wt%Pt-TiO₂ and d) 5.0wt%Pt-TiO₂

Table 10 also shows that the TiO₂ modified with Pt and prepared using the F-127 template displays an increased surface area versus the same photocatalyst synthesized with P-123. In terms of pore volume, the F-127 photocatalyst displays a larger porosity than P-123 and Degussa P-25.

Table 10 reports the specific surface area, the average pore diameter and the specific pore volume for mesoporous TiO₂ prepared using F-127 and P-123 templates. It is shown that when using templates such as F-127 and P-123, the morphological properties of TiO₂ are improved as follows: a) specific surface areas are increased, b) average pore diameters are augmented, c) specific pore volumes are increased. Furthermore, one can also notice that

the F-127-TiO₂, displays both higher porosity and specific surface area than the P-123-TiO₂. The shown data is the result of average values.

Table 10 Surface area and pore diameter using templates F-127 and P-123

Photocatalyst	S^{BET} (m² g⁻¹)	Dp^{BJH} (4Vp^{BJH}/S^{BET}) (nm)	Vp^{BJH} (cm³g⁻¹)
Anatase	10.70	7.34	0.05
Rutile	4.56	4.67	0.05
Degussa P-25	58.78	7.49	0.25
TiO ₂ -500C F-127	139.57	17.54	0.61
1.0%wtPt-TiO ₂ 500C F-127	127.60	17.88	0.57
2.5%wtPt-TiO ₂ 500C F-127	158.92	23.27	0.92
5.0%wtPt-TiO ₂ 500C F-127	133.11	22.27	0.75
TiO ₂ -500C P-123	111.49	20.13	0.56
1.0%wtPt-TiO ₂ 500C P-123	115.34	17.91	0.51
2.5%wtPt-TiO ₂ 500C P-123	110.04	22.57	0.62
5.0%wtPt-TiO ₂ 500C P-123	116.11	21.66	0.62

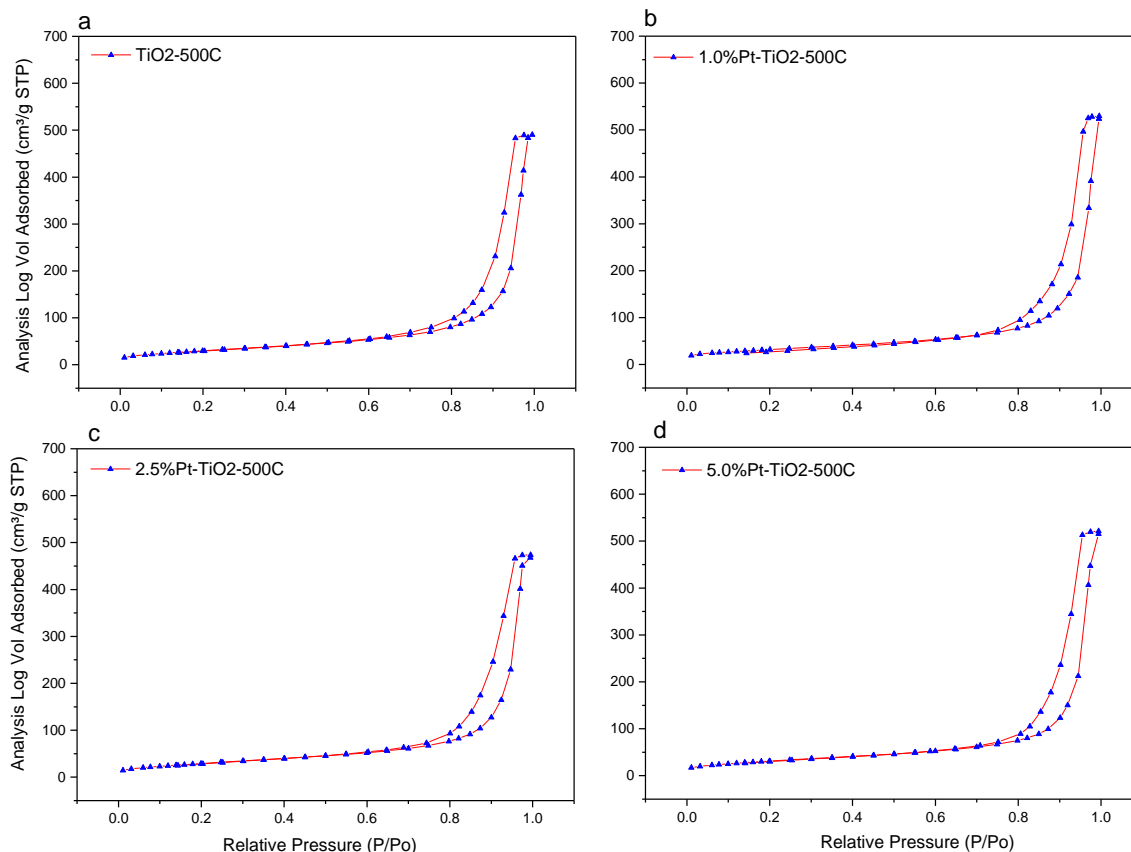
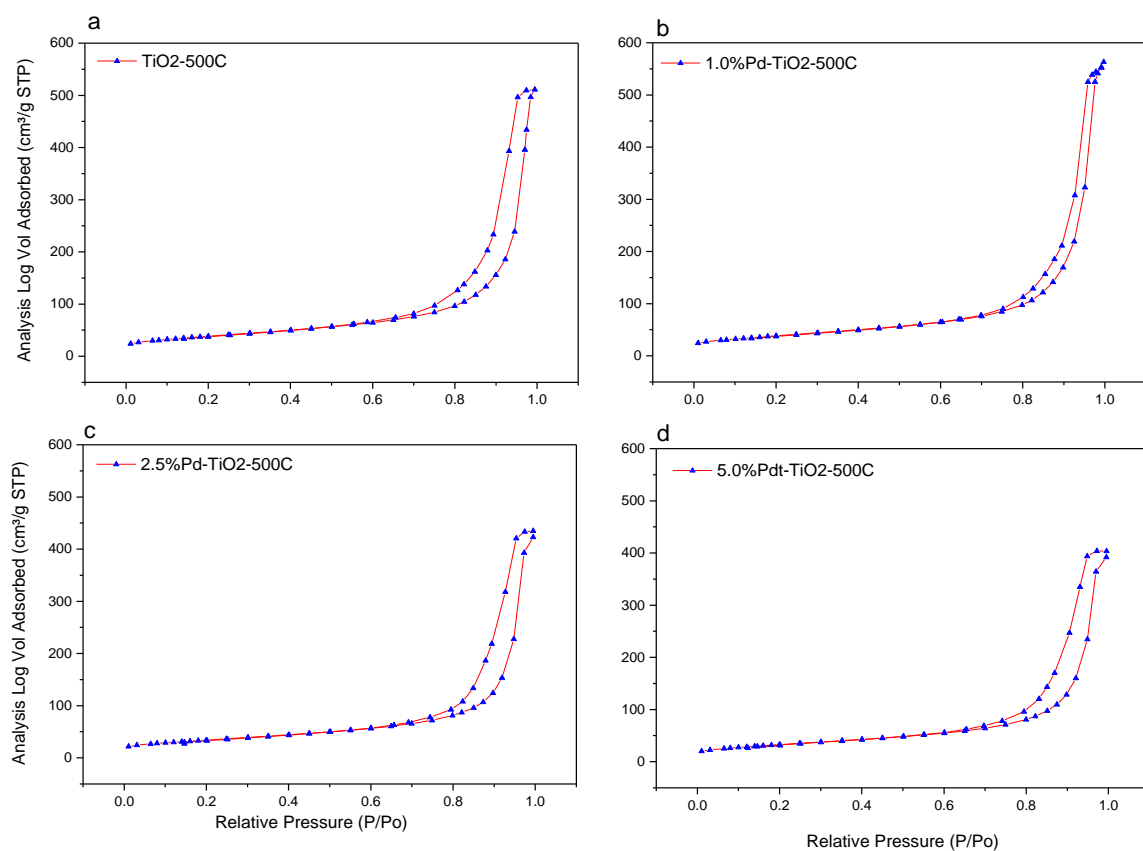


Figure 19 N₂ Adsorption-Desorption Isotherms for Mesoporous TiO₂ using Pluronic P-123, Calcined at 500°C. a) TiO₂, b) 1.0wt%Pt-TiO₂, c) 2.5wt%Pt-TiO₂ and d) 5.0wt%Pt-TiO₂

Table 11 compares the measured specific surface area (S_{BET}), the average pore diameter (D_p) and the pore volume (V_p) for the photocatalyst synthesized using the F-127 template as well as being modified with platinum and palladium. Best results were observed with the 1.0wt%Pd-TiO₂-500°C F-127 photocatalyst, as shown in Figure 20. This photocatalyst displays an increase of the specific surface area and in the specific pore volume when compared to Degussa P-25. For TiO₂ doped with palladium in excess of 1.0wt%, a reduction in specific surface area and a decrease in average pore diameter was attributed to a possible and moderate blocking of the TiO₂ pores with Pd [145]. The shown data is the result of average values.

Table 11 Surface area and pore diameter using Platinum and Palladium

Photocatalyst	S_{BET} ($\text{m}^2 \text{g}^{-1}$)	D_p^{BJH} ($4V_p^{\text{BJH}}/S_{\text{BET}}$) (nm)	V_p^{BJH} ($\text{cm}^3 \text{g}^{-1}$)
Anatase	10.70	7.34	0.05
Rutile	4.56	4.67	0.05
Degussa P-25	58.78	7.49	0.25
TiO ₂ -500C F-127	139.57	17.54	0.61
1.0wt%Pt-TiO ₂ 500C F-127	127.60	17.88	0.57
2.5wt%Pt-TiO ₂ 500C F-127	158.92	23.27	0.92
5.0wt%Pt-TiO ₂ 500C F-127	133.11	22.27	0.75
1.0wt%Pd-TiO ₂ -500C F-127	159.90	23.35	0.81
2.5wt%Pd-TiO ₂ -500C F-127	122.40	19.87	0.60
5.0wt%Pd-TiO ₂ -500C F-127	119.24	18.91	0.56

**Figure 20** N₂ Adsorption-Desorption Isotherms for Mesoporous TiO₂ using Pluronic F-127, Calcined at 500°C. a) TiO₂, b) 1.0wt%Pd-TiO₂, c) 2.5wt%Pd-TiO₂ and d) 5.0wt%Pd-TiO₂

The BJH method was used to determine the pore size distribution (PSD), by utilizing the desorption isotherm with N₂ as an adsorbate. Figure 21 reports a pore diameter distribution. In all cases, a bimodal pore volume distribution in the ranges reported in Table 12 was observed. One can notice that the largest pore sizes in the 16-35nm range were achieved with 1.0wt%Pd-TiO₂-500°C F-127.

Table 12 Pore size distribution range

Photocatalyst	Pore size distribution range (nm)
TiO ₂ -500°C P-123	6- 23
TiO ₂ -500°C F-127	9- 22
1.0wt% Pt-TiO ₂ 500C P-123	11-33
2.5wt% Pt-TiO ₂ 500C P-123	15-24
5.0wt% Pt-TiO ₂ 500C P-123	12-23
1.0wt% Pt-TiO ₂ 500C F-127	9 – 24
2.5wt% Pt-TiO ₂ 500C F-127	9 – 23
5.0wt% Pt-TiO ₂ 500C F-127	13 – 22
1.0wt% Pd-TiO ₂ -500C F-127	16 – 35
2.5wt% Pd-TiO ₂ -500C F-127	16 – 22
5.0wt% Pd-TiO ₂ -500C F-127	13 – 25

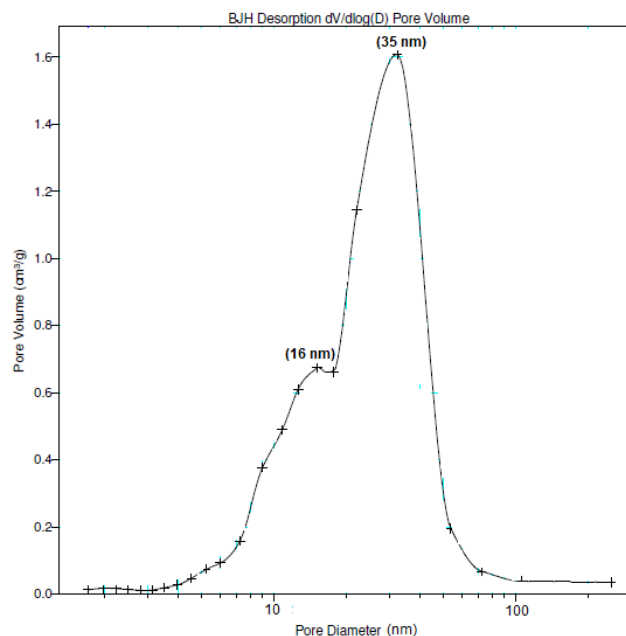


Figure 21 BJH pore size distribution plot for 1.0wt%Pd-TiO₂-500°C F-127

4.2 Pulse Hydrogen Chemisorption

By using the Micromeritics AutoChem II Analyzer for pulse chemisorption, one can calculate the fraction of dispersed metal and average active metal crystallite size[146]. Using this method, a series of 10% hydrogen in argon pulses is contacted with the photocatalyst sample. It is the goal of the hydrogen chemisorption method to chemisorb hydrogen on every active single site of the photocatalyst sample, until all sites are occupied by hydrogen[147]. Furthermore, and on the basis of the difference between the total volume of hydrogen injected as a train of pulses and the cumulative volume of all hydrogen eluted from the photocatalyst sample, the total amount of chemisorbed hydrogen or V_s is calculated.

Thus, according to Pulse Hydrogen Chemisorption assumptions, a hydrogen molecule chemisorbs on a single Pt site or Pd site. On this basis, one was able to calculate the metal percent dispersion using Equation 6 as follows.

$$PD = 100 \times \left(\frac{V_s \times SF_{calc}}{SW \times 22414} \right) \times MW_{calc} \quad \text{Equation 6[146]}$$

PD represents the percental metal dispersion, V_s is the hydrogen volume adsorbed expressed in cm^3 at STP, SF_{calc} stands for the adopted stoichiometry factor, SW denotes the photocatalyst sample weight in grams and MW_{calc} is the molecular weight of the noble metal dopant in g/g-mole.

To perform this analysis, a U-tube was filled with 0.15 g of the catalyst and then purged with argon at a rate of 50mL/min to remove the remaining air. Before this, a Temperature-Programmed Reduction (TPR) was carried out to determine the total number of reducible species present and the temperature at which the reduction occurs (500°C)[148].

Once the metal dispersion was established, it was also possible to calculate the metal crystallite size using the following equation:

$$D_{\text{cr}} = \frac{6}{PD\% S_p \rho_{\text{cr}}} \times 100 \text{ (nm)} \quad \text{Equation 7}$$

With PD being the percental metal dispersion, S_p representing the specific surface area in nm^2/g and ρ_{cr} denoting the density of metal crystallites (g/nm^3).

Crystallite size is determined by the use of the volumetric hydrogen chemisorption given that this methodology considers the stoichiometry and it has high reliability [149].

By reviewing Table 13 and Equation 7, one can see that increasing the metal loading decreases the metal dispersion and augments therefore, the metal crystallite size. Thus, higher metal loadings do not necessarily enhance metal crystallites as electron traps.

Table 13 Chemisorption analysis. Metal dispersion and crystallite size

Photocatalyst	Metal dispersion (%)	Crystallite Size (nm)
1.0wt%Pt-TiO ₂ -500°C F-127	44.67	2.53
2.5wt%Pt-TiO ₂ -500°C F-127	31.30	3.61
5.0wt%Pt-TiO ₂ -500°C F-127	11.87	9.55

Photocatalyst	Metal dispersion (%)	Crystallite Size (nm)
1.0wt%Pd-TiO ₂ -500°C F-127	27.48	4.07
2.5wt%Pd-TiO ₂ -500°C F-127	11.49	9.74
5.0wt%Pd-TiO ₂ -500°C F-127	7.68	14.60

In summary, the best anticipated results in terms of providing the higher metal dispersion are the ones with the lower loadings of 1.0wt% of both Pt and Pd.

4.3 X-Ray Diffraction

X-ray diffraction (XRD) is an analytical technique used to identify the phases of a crystalline material. X-rays are generated by a cathode ray tube and directed towards the sample. The X-rays pass through the material to be analyzed and are scattered by the electron clouds around the atoms. The contact of the incident rays with the sample generates a constructive interference (and a diffracted ray). The relationship between the wavelength of electromagnetic radiation to the diffraction angle (2θ) and the lattice spacing in a crystalline sample is the Bragg's law as follows[150].

$$n\lambda = 2d_{hkl}\sin \theta \quad \text{Equation 8}$$

Where, n represents the order of diffraction, λ =wavelength in nm, d_{hkl} = distance between lattice planes in nm and θ =angle of the incoming light in deg.

The XRD spectra in the present study was analyzed in a Rigaku Rotating Anode X-Ray diffractometer operated at 45 kV and 160 mA. The scans were taken between 20-80°, with a step size of 0.02 degrees and with a dwell time of 2s/step for the characterization of the atomic structure in the photocatalysts.

Figure 22 Figure 23 report the diffractogram patterns for TiO₂ using the template F-127 for different loadings of platinum and palladium. Anatase, rutile and metal peaks are shown. Anatase peaks are at the 2θ diffraction angles of 25, 38, 48, 54, 63, 69, 70.5 and 75 corresponding to the planes (101), (004), (200), (105), (204), (116), (220) and (215)

[JCPDS No. 73-1764]. For rutile, there are couple noticeable peaks at 54 and 67 corresponding to the planes (201) and (301) [JCPDS No. 34-0180].

When analyzing the sample with XRD, a significant anatase XRD peak was observed in the synthesized photocatalysts. The nature of these anatase was confirmed with a 99.7 % anatase from Aldrich reference sample, free of rutile. This is ideal given anatase is reported to display a better photocatalytic performance than rutile [151].

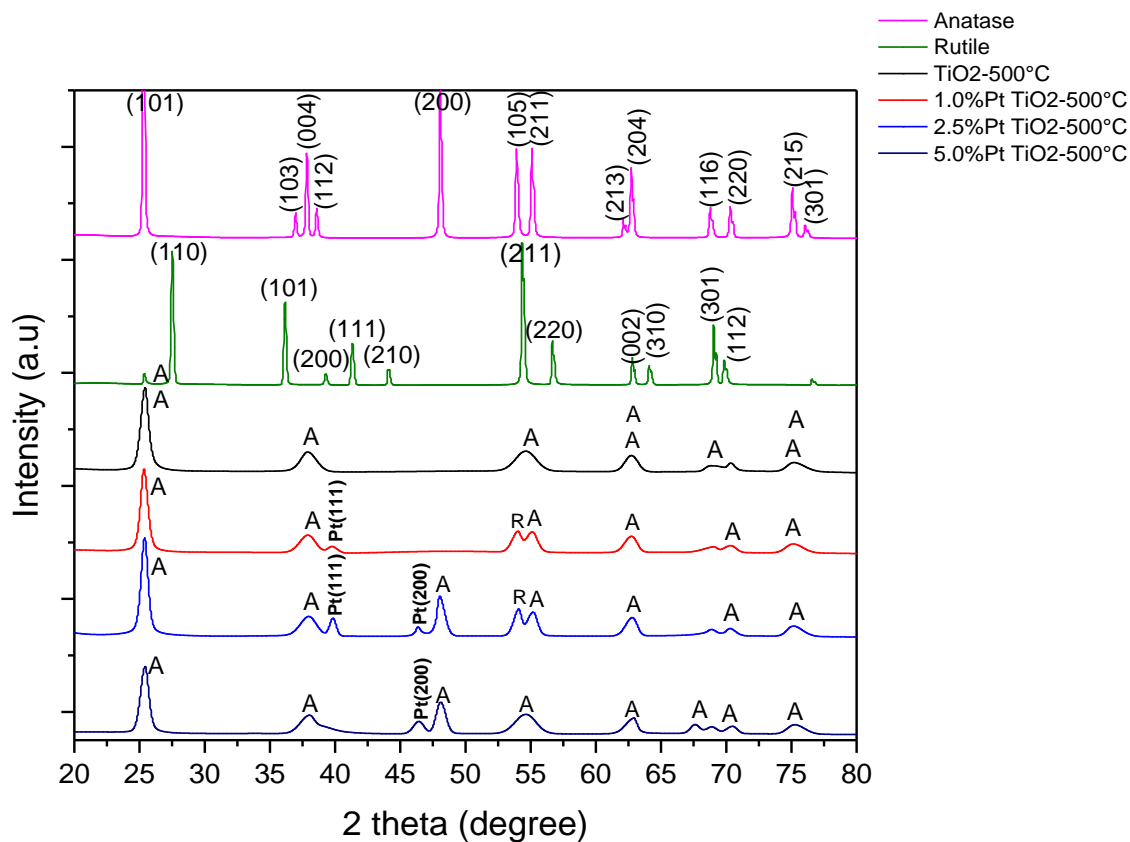


Figure 22 XRD Diffractograms of catalyst doped by Pt. XRD overlapped for comparison. A = anatase, R= Rutile, Pt=Platinum

Pt and Pd species were studied using XRD. In the case of Pt, the peaks at 39.7° (111) and 46° (200) in the 2θ angle scale confirmed the presence of Pt [JCPDS No. 01-1194] in the face-centered cubic structure. For Pd, there were peaks recorded at 40.12° (111) and 46.66° (200) angle [JCPDS No. 87-0638]. One should observe that in principle, a third peak at 2θ

= 68.1° (220) should be recorded for Pd. However, this peak may overlap with anatase and as a result, cannot be used for Pd identification[152].

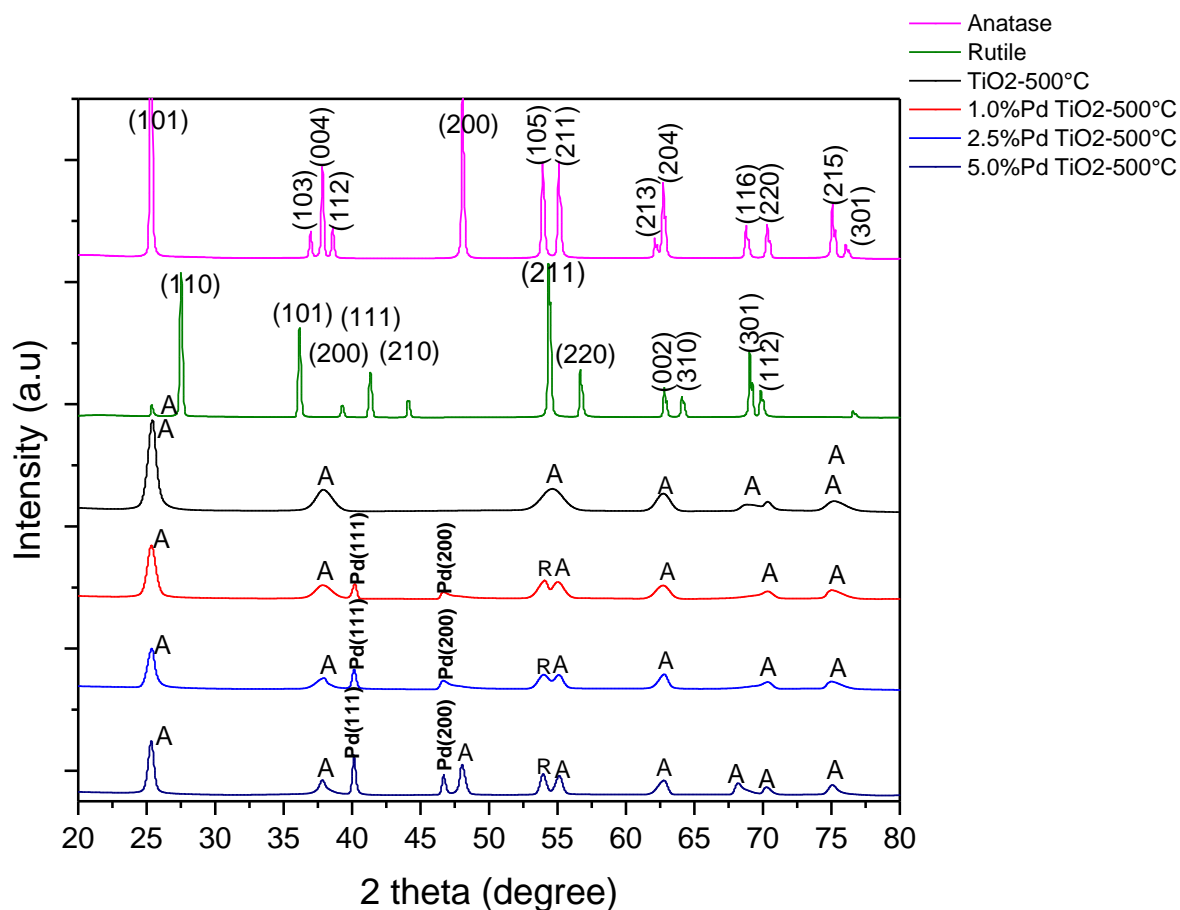


Figure 23 XRD Diffractograms of catalyst with Pd. XRD for anatase, rutile and undoped TiO₂ are reported as a reference for comparison. XRD overlapped for comparison. A = anatase, R= Rutile, Pd=Palladium

The weight fraction of rutile can be calculated using Equation 9:

$$X = 1 / (1 + 0.8I_A / I_R) \quad \text{Equation 9}$$

Where, X represents the weight fraction of rutile, I_A the X-ray intensity of the strongest peak of anatase at the $2\theta=25.3^\circ$, (101) plane) and I_R the X-ray intensity of the strongest peak of rutile ($2\theta=54^\circ$, (211) plane).

Table 14 reports the average calculated weight fractions of rutile determined by using Equation 9.

Table 14 Anatase and rutile content in the photoactive materials

Photocatalyst	Anatase content (%)	Rutile Content (%)
TiO ₂ -500°C F-127	100	0
1.0wt%Pt-TiO ₂ 500°C F-127	76.75	23.25
2.5wt%Pt-TiO ₂ 500°C F-127	74.80	25.20
5.0wt%Pt-TiO ₂ 500°C F-127	75.77	24.22
1.0wt%Pd-TiO ₂ -500°C F-127	70.59	29.41
2.5wt%Pd-TiO ₂ -500°C F-127	68.90	31.10
5.0wt%Pd-TiO ₂ -500°C F-127	65.99	34.01

As well, and as shown in Table 14, photocatalysts doped with platinum display a moderately larger anatase/rutile ratio than the photocatalyst doped with Pd, with the percental anatase/rutile ratio being 74-77% for Pt doped TiO₂ versus the 65-70% for Pd. This is in clear contrast with the essentially free of rutile phase of TiO₂ mesoporous photocatalysts.

Furthermore, XRD was also performed to determine if there were changes in the photocatalyst crystalline structure during photocatalyst water-splitting reaction runs. This was particularly important for Pd doped TiO₂, given that there were concerns that Pd would change its valence state during extended photocatalyst usage. It was in this respect observed, that after a 6 hour of photocatalytic water-splitting run, anatase was still the predominant TiO₂ phase with a percentage of 70-71% over rutile. Pd species were still present with their characteristic peak at a 40.12° angle (111) band. However, the 46.66° (200) angle band was no longer observed as shown in Figure 24.

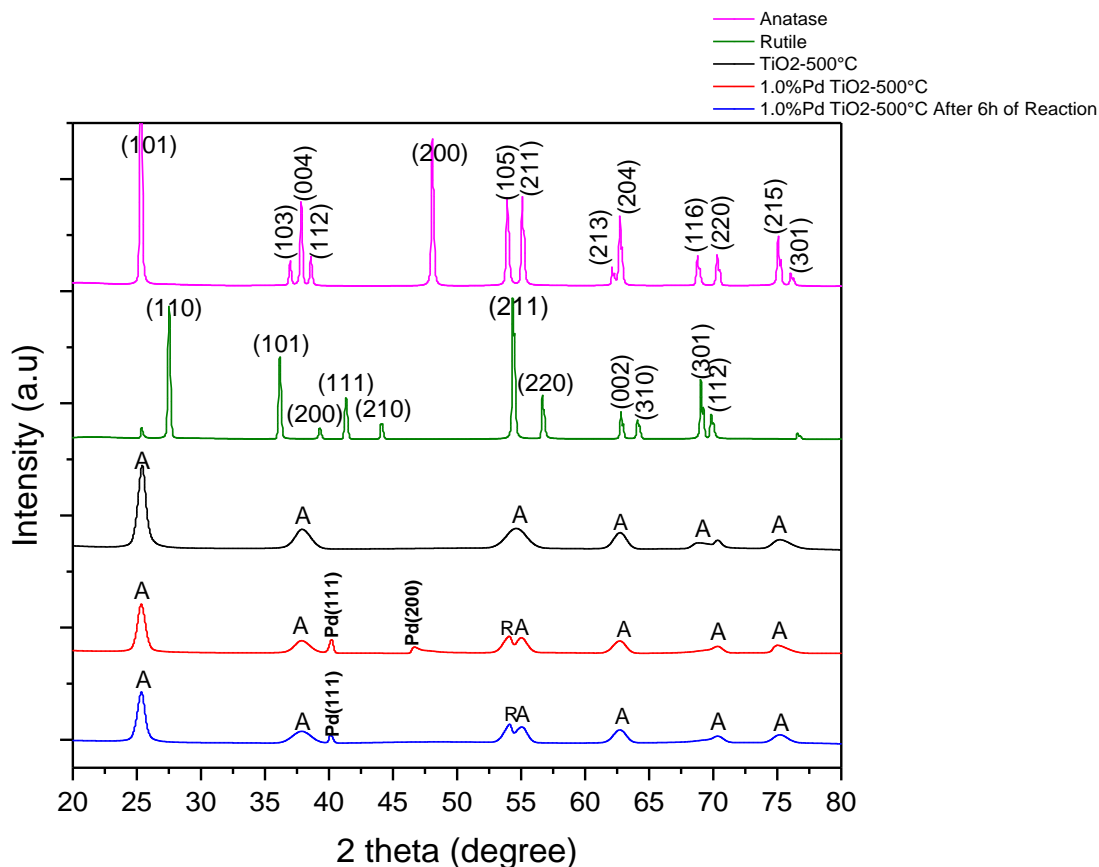


Figure 24 XRD Diffractograms for the Pd Doped TiO_2 after 6h of Photocatalytic Water Splitting. XRD for anatase, rutile and undoped TiO_2 are reported as a reference for comparison: A = anatase, R= Rutile, Pd=Palladium

4.4 Band gap

Photocatalysts display a characteristic band gap associated to a wavelength at which they achieve excitation. UV-visible absorption is used to determine these characteristic excitation wavelengths from diffuse reflectance spectra[153]. UV-Vis spectra of the photocatalysts of this study were measured using a UV-Vis-NIR spectrophotometer (Shimadzu UV-3600) equipped with an integrating sphere. BaSO_4 was used as a reference.

Figure 25 Figure 26 display absorbance changes as function of the wavelength for platinum and palladium. It is observed in these figures that increasing the metal loading reduces the absorbance.

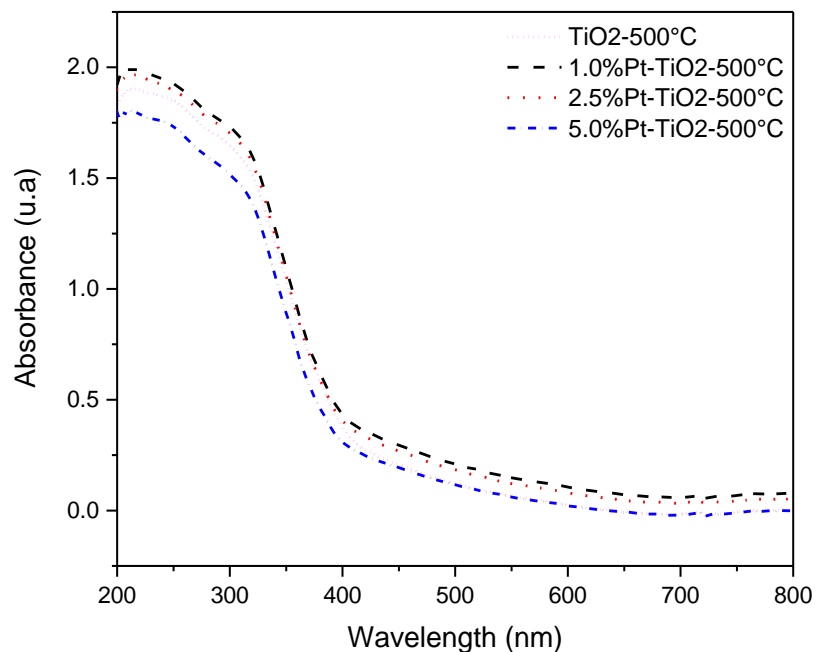


Figure 25 UV-vis absorption spectra Mesoporous materials at 1.0, 2.5 and 5.0wt%Pt

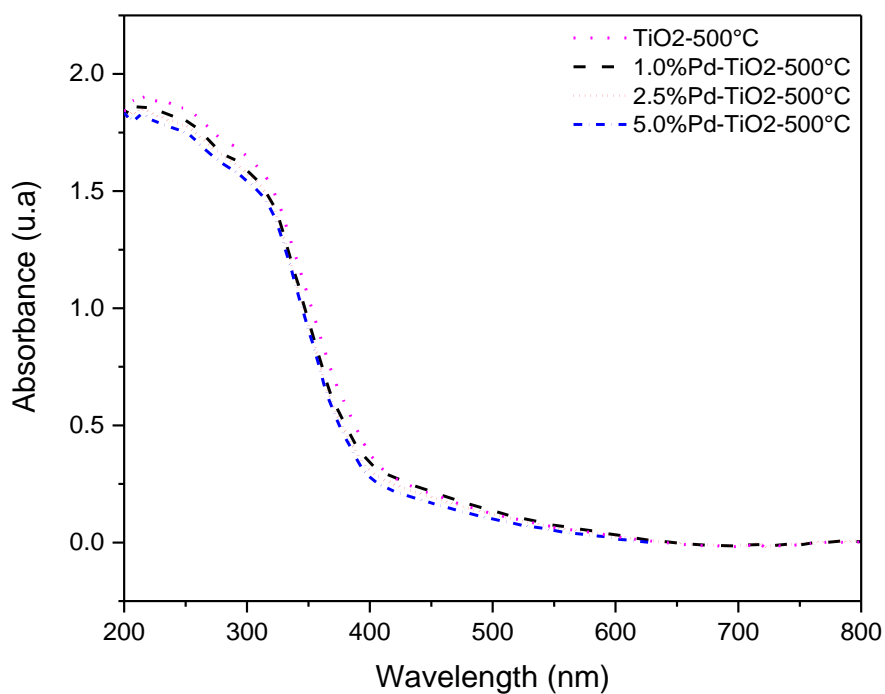


Figure 26 UV-vis absorption spectra Mesoporous materials at 1.0, 2.5 and 5.0wt%Pd

Kubelka-Munk (K-M) developed a Tauc plot methodology to establish band gaps as follows [154].

$$\alpha h\nu = A (h\nu - E_g)^m \quad \text{Equation 10}$$

With A being the optical constant, α representing the absorption coefficient, E_g denoting the optical band gap in eV, m standing for a value equal to 2 for indirect transitions, h being the Planck constant ($6.34\text{E-}34$ J s/photon) and ν representing the radiation frequency. It should be noted that in $\nu = c/\lambda$, where c is the speed of light under vacuum ($3.00\text{E}8$ m/s²) and λ is the corresponding wavelength in nm.

Figure 27 and Figure 28 report the changes of the " $(\alpha h\nu)^{1/2}$ " function versus the photon energy " $h\nu$ ". If the straight-line methodology is applied for the band gap calculation as shown with the red line, one can see that the intersection of this line with the x-axis provides the wavelength corresponding to the semiconductor band gap.

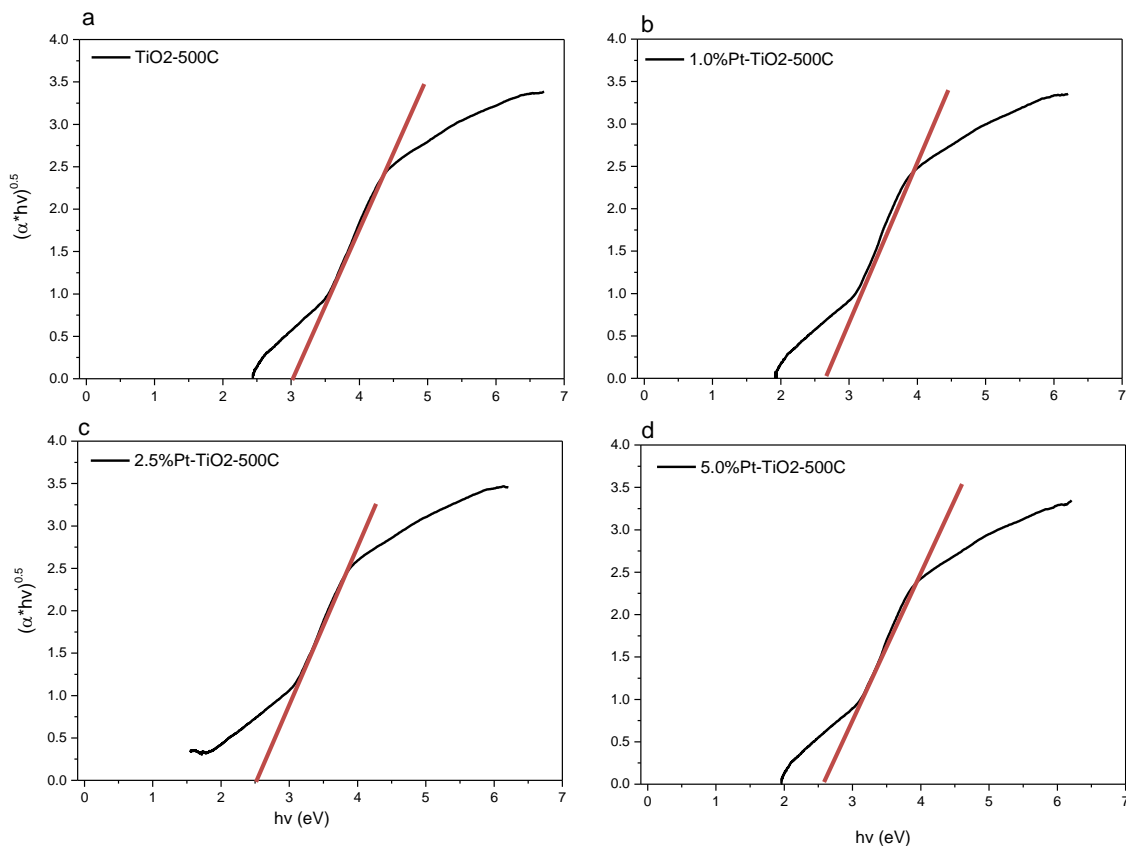


Figure 27 Band Gap Calculation using the Tauc Plot Methodology and the Straight Line Extrapolation for the following Photocatalysts: a) TiO₂, b) 1.0wt%Pt- TiO₂, c) 2.5wt%Pt-TiO₂ and d) 5.0wt%Pt-TiO₂

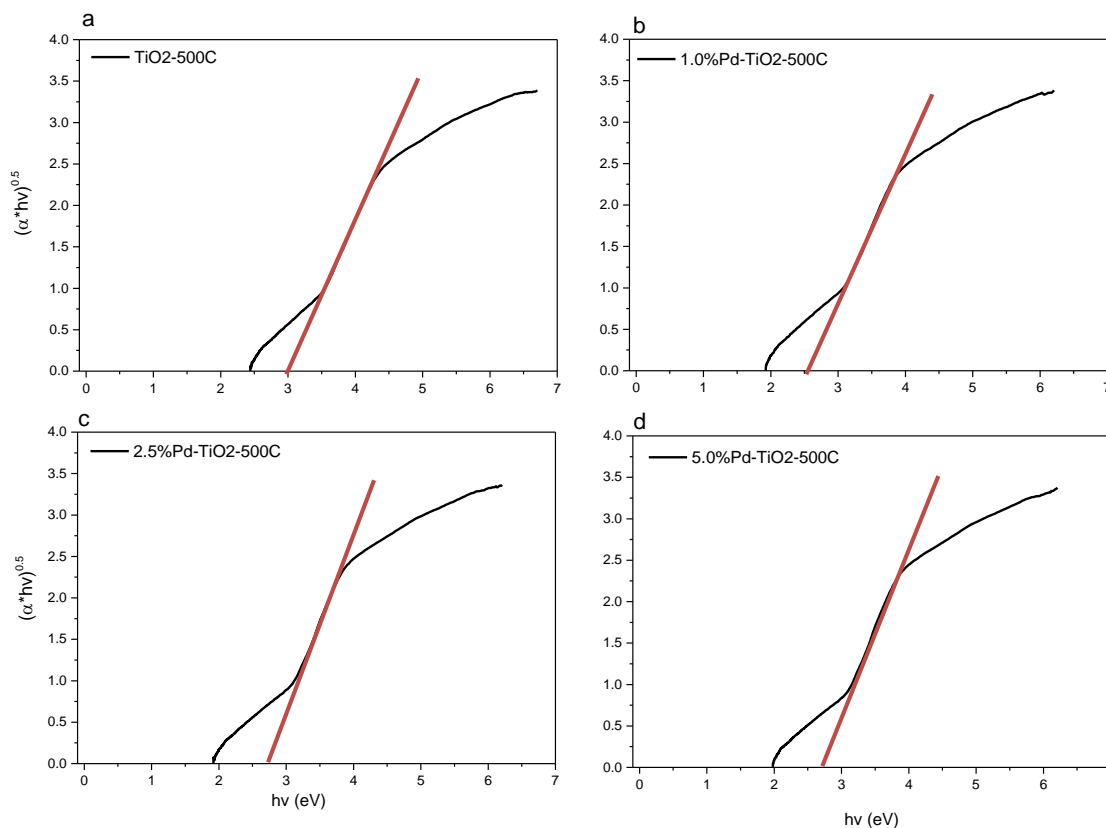


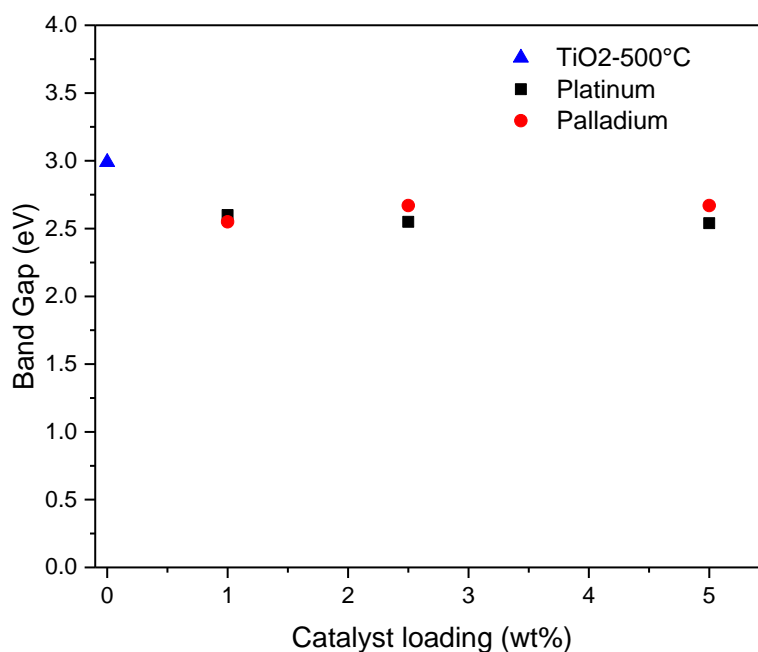
Figure 28 Band Gap Calculation Using the Tauc Plot Methodology and the Straight Line Extrapolation for the following Photocatalysts: a) TiO₂, b) 1.0wt%Pd- TiO₂, c) 2.5wt%Pd-TiO₂ and d) 5.0wt%Pd-TiO₂

Furthermore, the Tauc plots were developed for both Pt and Pd doped TiO₂ photocatalysts using the F-127 template and a 500°C calcination temperature. Table 15 reports that the band gaps for the TiO₂ doped with Pt and Pd display the following trends: a) Higher Pt loadings reduce the band gap, b) Increased Pd content slightly augments the band gap. Thus, and regarding the observed results, one can see a significant reduction in band gaps for TiO₂ doped with Pd and Pt.

Table 15 Optical band gap for photocatalyst modified by Pt and Pd

	Band gap (eV)	Wavelength (nm)	% of absorbed visible light
TiO ₂ -500C	2.99	415	4.91
1.0wt%Pt-500C-TiO ₂	2.60	477	25.64
2.5wt%Pt-500C-TiO ₂	2.55	486	28.75
5.0wt%Pt-500C-TiO ₂	2.54	488	29.39
1.0wt%Pd-500C-TiO ₂	2.55	486	28.75
2.5wt%Pd-500C-TiO ₂	2.67	464	21.47
5.0wt%Pd-500C-TiO ₂	2.67	464	21.47

Figure 29 Effect of metal loading on the optical band gap displays the changes of the band gap as assessed with the Tauc plot methodology with the noble metal loading. Thus, the addition of Pt and Pd in the mesoporous TiO₂ photocatalyst significantly reduces the band gap compared to the undoped TiO₂.

**Figure 29** Effect of metal loading on the optical band gap

As a result, one can forecast that more visible light is absorbed while using the noble metal doped photocatalysts.

Furthermore, and to quantify this effect, one can use Equation 11, which calculates the fraction of absorbed light:

$$\%VUI = \frac{\int_{\lambda_{\min}}^{\lambda_{bg}} I d\lambda}{\int_{\lambda_{\min}}^{\lambda_{\max}} I d\lambda} \times 100\% \quad \text{Equation 11[108]}$$

where, VUI is the visible utilized irradiation, I is the irradiance in photon/s, λ_{min} and λ_{max} denote the minimum and maximum wavelengths of solar irradiation and λ_{bg} stands for the wavelength related to the band gap measured in nm.

In summary, when using Equation 11, one can see that an increment of VUI in the range of 21-29% was reached with the addition of Pt and Pd noble metals. It could be due to the size of palladium crystals, these are larger than the ones from Platinum exhibiting an enhanced ability to absorb visible light[155].

For Pd, over passing 1.0wt% the visible light absorption diminishes. The increase of the noble metal loading could promote agglomeration and poor metal dispersion reducing the electron-hole pair generation and therefore affect the photoactivity [156].

4.5 Conclusions

The following are the main conclusions of the present chapter:

- a) The developed metal-loaded mesoporous TiO₂ photocatalyst requires a characterization using BET analysis. BET isotherms are generated and provide valuable information about the isotherm type as well as the specific surface area.
- b) XRD analysis is required to characterize the noble metal-doped TiO₂ photocatalysts. This is relevant to establish the various crystalline phases.
- c) H₂ chemisorption is necessary to determine metal crystallite sizing as well as establishing noble metal dispersion.
- d) To analyze the effect of noble metal addition on the TiO₂ photocatalyst, requires band gaps determination. This is essential to fully assess the impact of Pt and Pd under visible and near UV light on photocatalysts performance.

Chapter 5

5 Macroscopic Radiation Energy Balance (MREB)

Photocatalytic reactors operate based on emitted photons, from either near-UV or visible light lamps. These photons are absorbed by a circulating semiconductor slurry suspension. To be able to establish the absorbed radiation in the Photo-CREC Water-II Reactor, one must develop a macroscopic radiation balance as is described in the upcoming sections of this chapter.

5.1 Methodology

Various photocatalytic processes including water splitting for hydrogen production require an estimation of the photo-absorption rates for accurate energy efficiency calculations[157].

As it was mentioned in Chapter 4, the Photo-CREC Water-II reactor (PCW-II), is a slurry concentric unit which its irradiated energy is provided by an inner central lamp. This reactor allows the downflow circulation, as well as the suspended photocatalyst recirculation in the PCW-II annular section (space between the Pyrex glass and the polyethylene outer tube). The reactor unit is equipped with seven (7) silica windows located on the outer reactor surface. Irradiation measurements are taken along the reactor axis by using these windows.

Furthermore, a fibre optic spectrometer StellarNet EPP2000-25 calculates the radiation spectra emitted by the lamp. The spectrometer detects transmitted photons in the 300 nm to 720 nm range at a set scanning time of 300 ms, avoiding in this manner, sensor reading saturation.

Figure 30 describes the optical fibre spectroradiometer sensor system as when placed in one of the possible 7 equally spaced axial locations. By using the optical fibre spectroradiometer system, transmitted radiation can be measured in the PCW-II with the lamp turned on under different conditions: a) the PCW-II Reactor empty, b) the PCW-II filled with water, c) the PCW-II with suspended photocatalyst, d) the PCW-II Reactor filled

with water only and this after extended photocatalytic runs. All these transmission measurements provide valuable data required to accurately perform macroscopic radiation balances at various times-on-stream of photocatalyst usage.

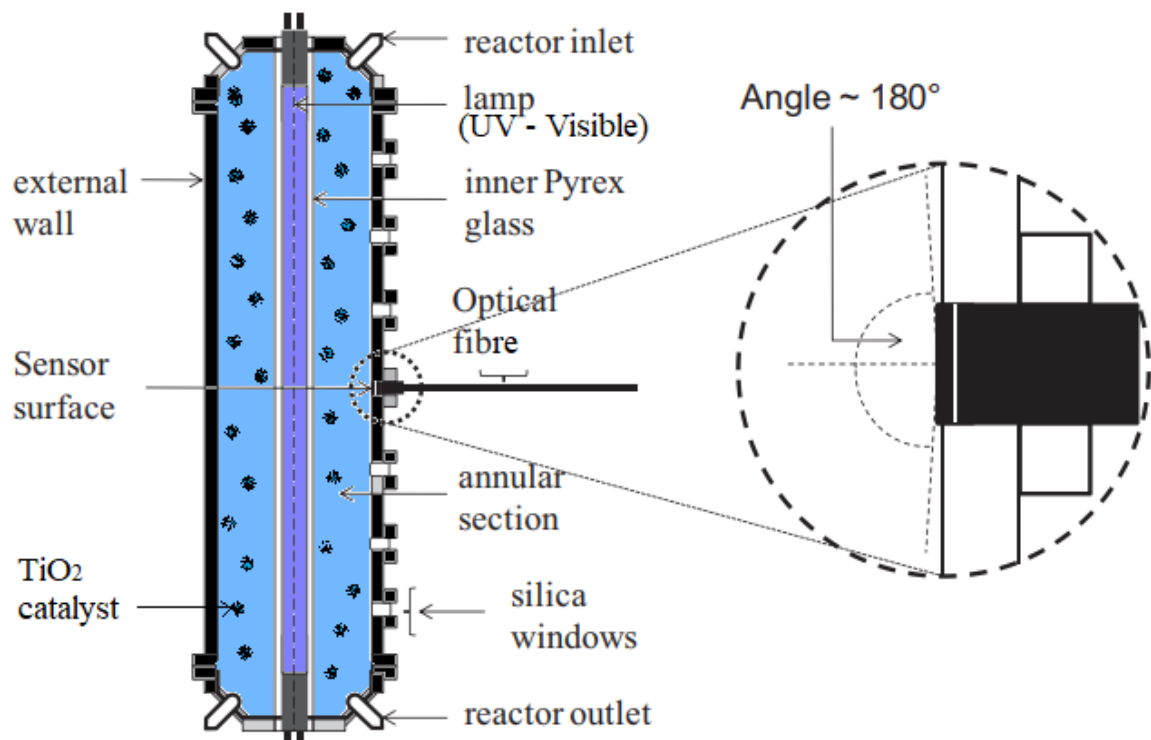


Figure 30 Photo-CREC Water-II Reactor with Optical Fibre Sensors in Place for Transmitted Radiation Measurements [158]

5.2 Macroscopic Radiation Balance

Establishing the absorbed radiation in a Photo-CREC Water-II Reactor is critical to determine energy efficiencies [159]. Figure 31 describes the various radiation terms involved in macroscopic radiation balances.

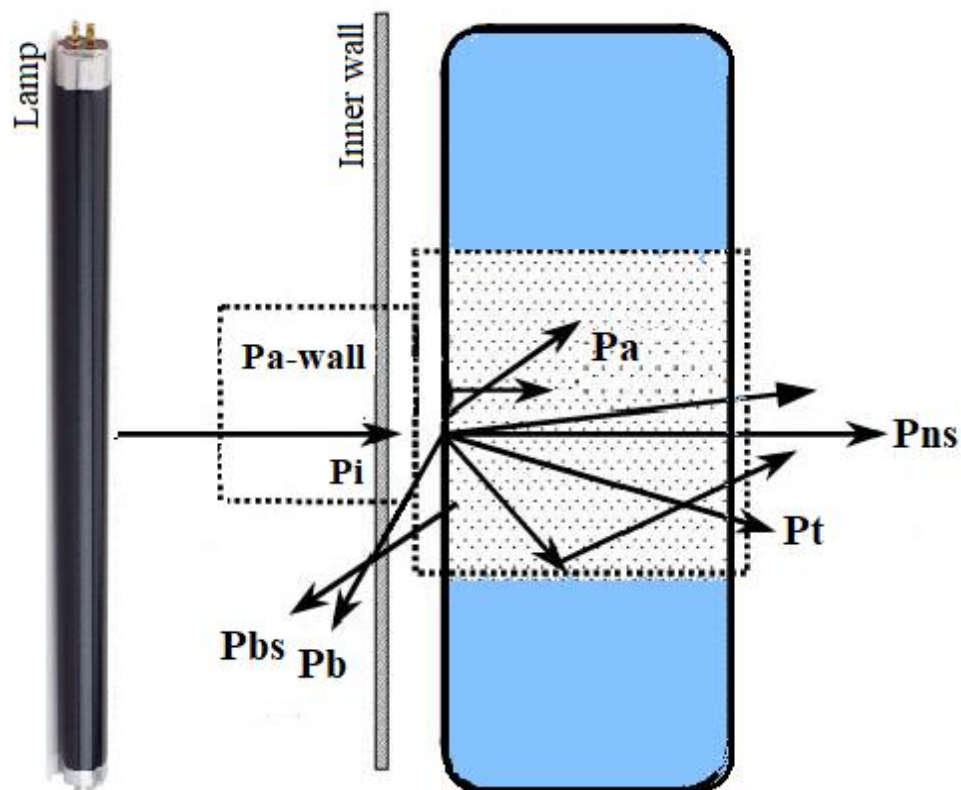


Figure 31 Macroscopic radiation balance around TiO_2 [116]

To accomplish this, a macroscopic radiant energy balance as proposed by Salaiques, Serrano and de Lasa[160], can be considered in a “photocatalyst control volume” . This macroscopic balance estimates the photons absorbed as the difference between the incident photons and the combined scattered and transmitted photons.

$$P_a = P_i - P_{bs} - P_t \quad \text{Equation 12}$$

Where P_a is the rate of absorbed photons; P_i is the rate of photons reaching the reactor at the inner Pyrex glass surface and is calculated according to Equation 13 in Einstein s^{-1} ; P_{bs} is the rate of backscattered photons; and P_t is the rate of transmitted photons. All these variables can be expressed using the Einstein s^{-1} units.

And

$$P_i = P_0 - P_{a-wall} \quad \text{Equation 13}$$

with P_o in Einstein s^{-1} , being this the rate of photons emitted by the lamps as per Equation 14 and P_{a-wall} in Einstein s^{-1} the rate of backscattered photons absorbed by the Pyrex glass walls.

$$P_o = \int_{\lambda_1}^{\lambda_2} \lambda \int_0^L \int_0^{2\pi} q(\theta, z, \lambda) r d\theta dz d\lambda \quad \text{Equation 14}$$

where $q(\theta, z, \lambda)$ is the radiative flux ($J s^{-1} m^{-3}$), λ represents the wavelength (nm), r stands for the radial coordinate (m), z denotes the axial coordinate (m), h is the Planck's constant (J s), and c represents the speed of light ($m s^{-1}$). The term $q(\theta, z, \lambda)$ is determined using the spectrometer.

Furthermore, when photocatalytic experiments are performed in the PCW-II Reactor, photons are absorbed and scattered in the reacting medium. Therefore, a backscattering has to be accounted for. A possible approach to calculate backscattering is to establish the difference between P_i and the rate of photons transmitted when the catalyst concentration approaches zero ($P_t|_{c \rightarrow 0^+}$).

$$P_{bs} = P_i - P_t|_{c \rightarrow 0^+} \quad \text{Equation 15}$$

Equation 15 assumes that most backscattered photons are the result of backscattering centres located in the TiO_2 particle layer close to the inner surface of the transparent Pyrex walls. Other than this, it is hypothesized that no other photons backscattered contribute to P_{bs} .

Additionally, for P_t determination, equation 15 is used. It considers that transmitted radiation can be defined as the addition of normal scattered photons and forward scattered photons.

$$P_t = P_{ns} + P_{fs} \quad \text{Equation 16}$$

One should note that ($P_{fs} + P_{ns}$) can be measured employing aluminium polished collimators capturing radiation reaching the measuring point, with large view angles.

5.3 Near-UV-light MREB

Macroscopic balances using near-UV light were established at the central axial position using a 0.15g/L photocatalyst.

Table 16 reports measurements for TiO₂ photocatalysts with different metal loadings.

Table 16 Absorbed Photon Rates on TiO₂ Photocatalysts, at Different Metal Loadings, under UV-Light. Notes: Photocatalyst Concentration: 0.15g/L, $P_0 = 8.46E-06$ Einstein/s with 96% radiation transmitted through Pyrex glass tube. All reported data are average values of 3 repeats. Standard deviation: $\pm 3.5\%$.

UV Light	Pt (Einstein/s)	Pt $c \rightarrow 0^+$ (Einstein/s)	Pbs (Einstein/s)	Pa (Einstein/s)	% Abs. Efficiency
TiO ₂	3.09E-06	5.94E-06	1.70E-06	2.92E-06	37.8
1.0wt% Pt	1.22E-06	5.81E-06	2.24E-06	4.99E-06	59.1
2.5wt% Pt	8.65E-07	5.67E-06	2.38E-06	5.21E-06	61.6
5.0wt% Pt	5.03E-07	5.54E-06	2.51E-06	5.44E-06	64.3
1.0wt% Pd	1.85E-06	6.69E-06	1.50E-06	5.11E-06	60.4
2.5wt% Pd	1.67E-06	5.18E-06	3.01E-06	3.77E-06	44.6
5.0wt% Pd	1.18E-06	4.68E-06	3.51E-06	3.76E-06	44.5

One can notice that additions of Pt and Pd on TiO₂ show different trends. In the case of Pt, higher Pt levels lead to an increased P_a . However, higher Pd levels lead to P_a reduction. For Pd, these findings are in line with an increased photon backscattering.

Considering that the 1.0wt%Pd-TiO₂ showed the best performance in terms of photon absorption, changes of photocatalyst concentration were also considered. Table 17 reports the rates of absorbed photons at different catalyst weights of 0.15, 0.30, 0.50 and 1.00g/L.

Table 17 Rate of absorbed photons at different catalyst concentrations under UV-Light. Notes: Photocatalyst: 1.0wt%Pd-TiO₂, P₀ =8.46E-06 Einstein/s with 96% radiation transmitted through Pyrex glass tube. All reported data are average values of 3 repeats. Standard deviation: ±4.0%.

Catalyst (g/L) concentration	Pt (Einstein/s)	Pt $c \rightarrow 0^+$ (Einstein/s)	Pbs (Einstein/s)	Pa (Einstein/s)	% Abs. Efficiency
0.15	8.74E-07	5.77E-06	2.28E-06	5.30E-06	63
0.30	6.61E-07	4.46E-06	3.59E-06	4.20E-06	50
0.50	1.25E-07	2.90E-06	5.15E-06	3.18E-06	38
1.00	2.70E-08	2.19E-06	5.86E-06	2.57E-06	30

Figure 32 and Table 17 show that the measured irradiance decreases when the photocatalyst concentration increases. This phenomenon was assigned to an augmented backscattering at the near inner Pyrex glass tube region. Increasing the catalyst concentration over 0.15g/L does not ensure that all the radiation will be absorbed in the slurry medium and most of it will be lost as backscattering.

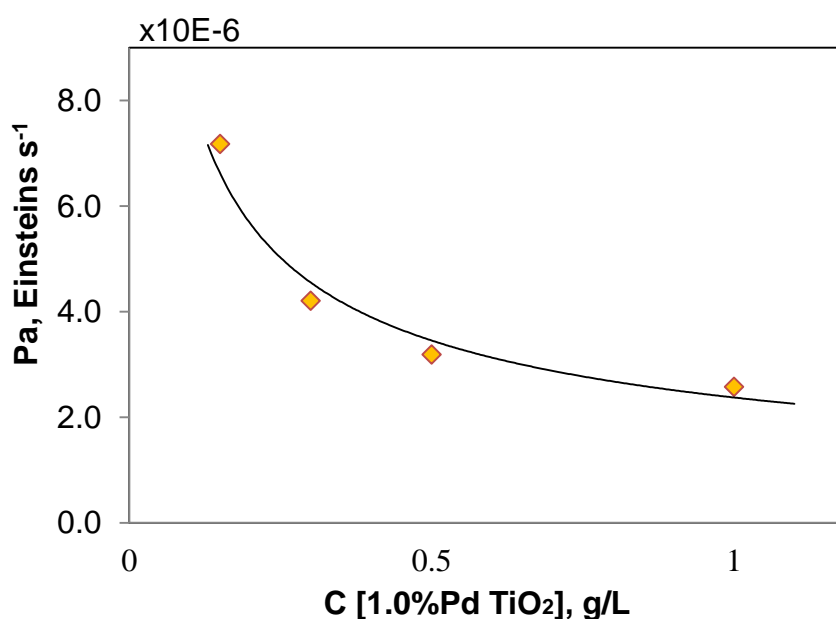


Figure 32 Transmitted radiation at different catalyst concentrations. TiO₂ doped with 1.0wt%Pd

An increment in the catalyst concentration can also lead to the formation of agglomerates in the near Pyrex glass wall region. The presence of these in the slurry medium might

explain the decreasing Pa irradiation. This thus, result on reduced radiation transmission with enhanced backscattering [161].

5.4 Visible light MREB

The photocatalyst developed in the present study was also evaluated using visible light. With this end, macroscopic radiation energy balances were developed for the Pd and Pt doped TiO₂ at the central axial position. Table 18 describes the rate of absorbed photons reaching the reactor inner surface.

Table 18 Absorbed Photon Rates on TiO₂ Photocatalysts, at Different Metal Loadings, under Visible light. Notes: Photocatalyst Concentration: 0.15g/L, P_o = 9.56E-06 Einstein/s with 96% radiation transmitted through Pyrex glass tube. All reported data are average values of 3 repeats. Standard deviation: ±2.4%.

Visible Light	Pt (Einstein/s)	Pi c-0 (Einstein/s)	Pbs (Einstein/s)	Pa (Einstein/s)	% Abs. Efficiency
TiO ₂	5.66E-06	7.78E-06	1.42E-06	2.48E-06	25.9
1.0wt% Pt	1.44E-06	4.25E-06	4.96E-06	3.16E-06	33.1
2.5wt% Pt	1.68E-06	5.30E-06	3.91E-06	4.01E-06	41.9
5.0wt% Pt	2.37E-06	7.09E-06	2.12E-06	5.08E-06	53.1
1.0wt% Pd	2.68E-06	7.94E-06	1.26E-06	5.62E-06	58.8
2.5wt% Pd	2.57E-06	7.19E-06	2.01E-06	4.89E-06	52.1
5.0wt% Pd	1.73E-06	6.18E-06	3.02E-06	4.81E-06	50.3

One can see that noble metal doped TiO₂ photocatalysts under visible light are effective on increasing the absorbed radiation in the visible range, from 25% for the undoped TiO₂ to 53%-59% for the Pd and Pt doped TiO₂. This is as well consistent with the observations under near-UV irradiation[155].

5.5 Conclusions

This chapter analyzes the Macroscopic Energy Balance for photocatalyst at different Platinum and Palladium loadings as well as variable concentrations under UV light and Visible light. Below the most important conclusions:

- a) Doping photocatalysts with Pt and Pd leads to higher radiation absorption efficiencies.
- b) Pt- and Pd-doped TiO₂ photocatalysts display however, different trends at increased noble metal loadings. In this respect, the P_a becomes moderately higher at higher Pt loadings while the P_a decreases with increasing Pd concentrations. These trends are consistent for both near-UV light and visible light and appear to reflect the increased influence of backscattering at higher metal loadings.
- c) Photocatalyst concentrations above 0.15g/L do not enhance photon absorption. This detrimental effect observed at the higher photocatalyst concentrations, was assigned to an increased radiation backscattering in the slurry layer close to the reactor walls.

Chapter 6

6 Hydrogen Production Yields and By-products

Hydrogen production experiments were performed using the Photo CREC Water-II Reactor under near-UV irradiation and visible light under an argon atmosphere via water splitting. Two modified photocatalysts, x-Pt /TiO₂ and x-Pd /TiO₂ (x= 1.0, 2.5, 5.0% w/w) with reduced band gaps were employed. As well ethanol, was used as an OH radical scavenger to limit recombination of electron-hole pairs. Photoreaction by-products such as methane, ethane and CO₂ were analyzed and quantified. The photocatalytic reaction was also studied under a CO₂ atmosphere to determine its influence on hydrogen production and on the ethanol sacrificial agent.

Hydrogen production is reported in all cases as cumulative hydrogen produced in volumetric units at standard conditions (cm³ STP or cubic centimeters at atmospheric pressure and room temperature).

6.1 Photocatalytic Mechanism

The dissociation of water using ethanol as a scavenger proceeds with the band gaps previously determined in Chapter 4. In this case, a semiconductor is irradiated, and electron-holes are formed. Furthermore, redox reactions take place.

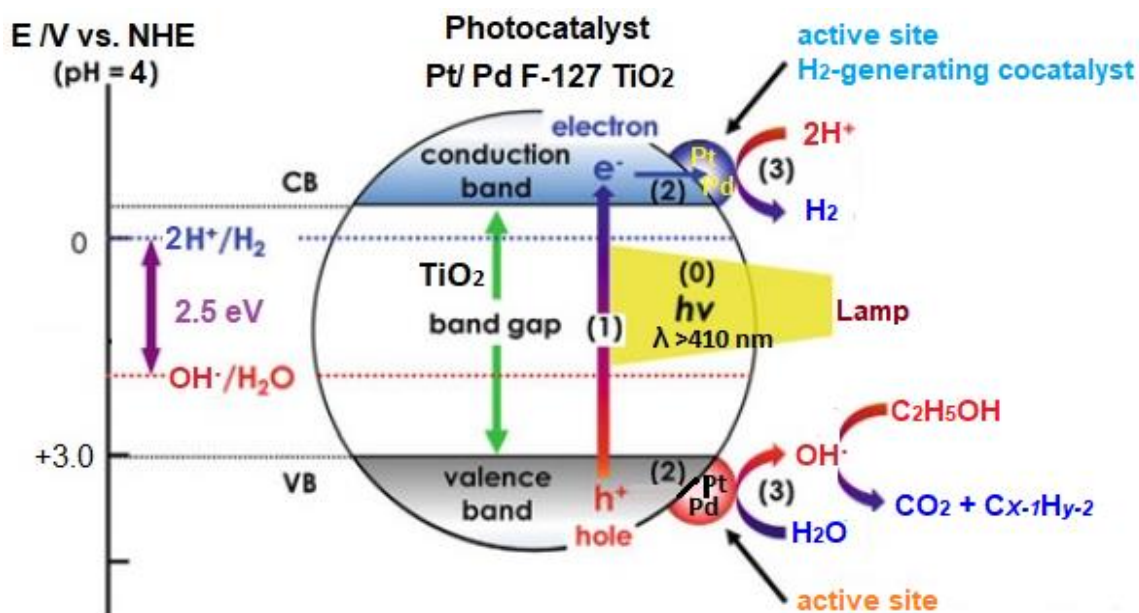


Figure 33 Hydrogen Reactions Steps using TiO_2 as Photocatalyst and Ethanol as Scavenger

Figure 33 describes schematically a sequence of events that occur on the TiO_2 surface for the $\text{H}\cdot$ and $\text{OH}\cdot$ formation [162]:

- 0) Photons coming from a near- UV or visible light source to reach the photocatalyst surface
- (1) An electron is promoted from the valence band to the conduction band creating an oxidation and reduction site. If the electron carries a higher energy level than the difference between the VB and the CB, it leads to hydroxyl radical ($\text{OH}\cdot$) formation. An organic scavenger such as ethanol initiates an oxidation process leading to the production of CO_2 and water. In this way, electrons (e^-) from the hole (h^+) pairs are separated.
- (2) Platinum or palladium captures excited electrons moving on the semiconductor surface.
- (3) Captured electrons interact with the formed H^+ from water, yielding $\text{H}\cdot$ radicals which can be coupled forming molecular hydrogen.

Escobedo et al, proposed a photocatalytic hydrogen production. This mechanism describes the various redox reactions, following water dissociation and, while ethanol was being used as an OH· radical scavenger (Table 19 and Figure 34). Main products reported were acetaldehyde, methane, ethane, CO₂ and hydrogen peroxide [163].

Table 19 Redox Reactions for Water Splitting over TiO₂

Reaction	Description
$h\nu \xrightarrow{\text{TiO}_2\text{-Pt/Pd}} h^+ + e^-$	Photogeneration of electron / hole pairs by the irradiation of the catalyst
$\text{H}_2\text{O}_{(\text{ads})} \xrightarrow{\text{TiO}_2\text{-Pt/Pd}} \text{H}_{(\text{ads})}^+ + \text{OH}_{(\text{ads})}^-$	Dissociation of water
$\text{H}_{(\text{ads})}^+ + e^- \xrightarrow{\text{TiO}_2\text{-Pt/Pd}} \text{H} \cdot$	Proton generation Proton reduction by the electrons to generate hydrogen radicals.
$\text{H} \cdot \xrightarrow{\text{TiO}_2\text{-Pt/Pd}} \frac{1}{2} \text{H}_2(\text{g})$	Covalent bonding between hydrogen radicals to form hydrogen molecules
$\text{OH}_{(\text{ads})}^- + h^+ \xrightarrow{\text{TiO}_2\text{-Pt/Pd}} \text{OH} \cdot$	OH ⁻ oxidation for OH· formation
Parallel Reactions	
$\text{C}_2\text{H}_5\text{OH} + \text{OH} \cdot \xrightarrow{\text{TiO}_2\text{-Pt/Pd}} \text{C}_2\text{H}_5\text{O}^- + \text{H}_2\text{O}$	Acetaldehyde production by radical OH· consumption reacting with ethanol
$h\nu + \text{H}_2\text{O} + \text{C}_2\text{H}_5\text{O}^- \xrightarrow{\text{TiO}_2\text{-Pt/Pd}} \frac{1}{2} \text{H}_2(\text{g}) + \text{C}_2\text{H}_4\text{O} + \text{H}_2\text{O}$	
$\text{C}_2\text{H}_4\text{O} + \text{OH} \cdot \xrightarrow{\text{TiO}_2\text{-Pt/Pd}} \text{C}_2\text{H}_3\text{O}^- + \text{H}_2\text{O}$	Acetaldehyde dissociation into acetic acid and methane. 3 OH· radicals are consumed
$h\nu + \text{C}_2\text{H}_3\text{O}^- + \text{H}_2\text{O} \xrightarrow{\text{TiO}_2\text{-Pt/Pd}} \frac{1}{2} \text{H}_2(\text{g}) + \text{CH}_3\text{COOH}$	
$\text{CH}_3\text{COOH} + \text{OH} \cdot \xrightarrow{\text{TiO}_2\text{-Pt/Pd}} \text{C}_2\text{H}_3\text{O}_2^-$	
$\text{C}_2\text{H}_3\text{O}_2^- + \text{H} \cdot \xrightarrow{\text{TiO}_2\text{-Pt/Pd}} \text{CH}_4 + \text{CO}_2$	
$2\text{CH}_3\text{COOH} + 2\text{OH} \cdot \xrightarrow{\text{TiO}_2\text{-Pt/Pd}} 2\text{CH}_3^- + 2\text{HCO}_2^-$	Acetic acid dissociation into ethane. 2 OH· radicals are consumed
$2\text{CH}_3^- + 2\text{HCO}_2^- \xrightarrow{\text{TiO}_2\text{-Pt/Pd}} \text{H}_2(\text{g}) + \text{C}_2\text{H}_6 + 2\text{CO}_2$	
$\text{OH} \cdot + \text{OH} \cdot \xrightarrow{\text{TiO}_2\text{-Pt/Pd}} \text{H}_2\text{O}_2$	Hydrogen peroxide production due to a reaction of OH· radicals

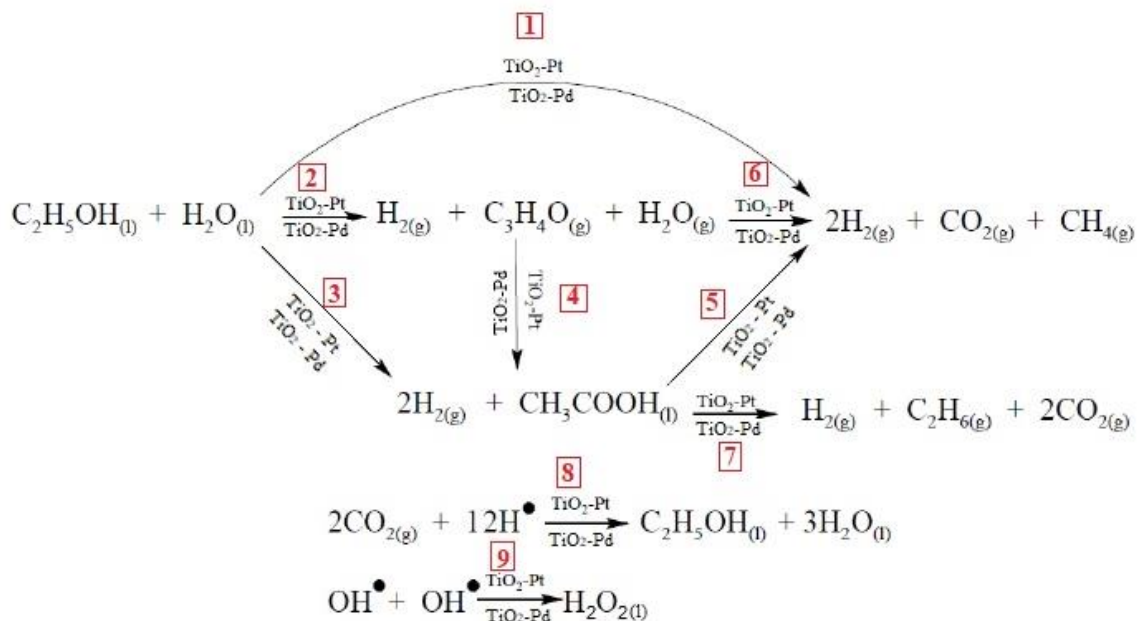


Figure 34 “In Series-Parallel” Reaction Network for Hydrogen Production using Ethanol as Scavenger

6.2 Hydrogen Production under Near-UV Light

Noble metal doped TiO₂ photocatalysts were evaluated in the present study, using the Photo CREC Water II Reactor equipped with a BLB UV Lamp during six (6) hours of continuous irradiation. This lamp was turned on 30 min before initiating photoreaction. The hydrogen storage/mixing tank was loaded with 6000 ml of water. Ethanol was used as a scavenger and the pH was adjusted to 4 ± 0.05 with H₂SO₄ [2M] keeping the photoreaction under acidic conditions. Favouring available H⁺ for water splitting process[102].

Following this step, the photocatalyst was loaded at a specific weight concentration ensuring that most of the radiation was absorbed in the slurry medium. The photocatalyst was subjected to sonification reducing the formation of particle agglomerates and promoting homogeneous mixing. An argon flow was circulated to guarantee an inert atmosphere at the beginning of the reaction. 1 ml of gas and 5 ml of liquid samples were

taken manually and evaluated using a GC (gas chromatograph) and a HPLC (liquid chromatograph) respectively.

The gas phase was analyzed with a Shimadzu GC2010 gas chromatograph using argon (Praxair 99.999%) as gas carrier. It had two (2) detectors, a flame ionization detector (FID) and a thermal conductivity detector (TCD). This unit was equipped with a HayeSepD 100/120 mesh packed column (9.1m x 2mm x 2 μ m nominal SS) used for the separation of hydrogen from air. This packed column detects carbon monoxide (CO), carbon dioxide (CO₂) and methane (CH₄). Likewise, the FID detects all hydrocarbon species such as CO and CO₂ and the TCD measures the produced hydrogen.

UFLC Ultra-Fast Liquid Chromatography System was utilized to characterize the liquid phase. This analytic technique allows the liquid mobile phase (0.1% H₃PO₄) to transport the sample through a column (Supelcogel C-610H 30cm x 7.8mm ID) containing a stationary phase and selectively separating individual compounds (Ethanol) from water for further detection. This quantitative analysis is performed by employing the RID 10A (Refractive Index Detector) due to polar nature of ethanol.

Both analytical techniques, the GC and the HPLC were used simultaneously. Samples were taken at different irradiation times.

It was anticipated that formed hydronium ions could be adsorbed on TiO₂, interacting with formed and stored electrons, promoting the formation of hydrogen radicals. Coupling of hydrogen radicals yielded molecular hydrogen.

6.2.1 Effect of Copolymer P-123 and F-127 on Hydrogen Production

Two non-ionic surfactants were used as templates (precursors) to modify the structure of the photocatalyst. These surfactants were Pluronic P-123 and F-127. They were utilized due to the positive impact they have on the morphology, porosity, surface area, particle size and crystallinity of TiO₂.

Figure 35 displays the influence of using both Pluronic P-123 and Pluronic F-127 on the cumulative volume of hydrogen produced, and this when the TiO₂ photocatalyst was doped with platinum.

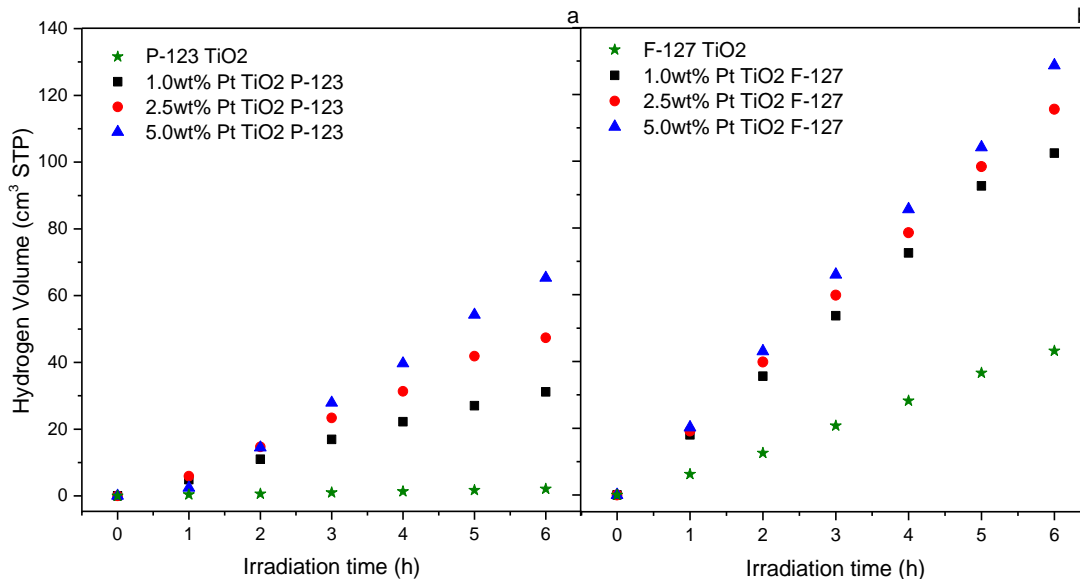


Figure 35 Cumulative Hydrogen Volume using Templates (a) P-123 and (b) F-127 at different Platinum Loadings (1.0, 2.5 and 5.0wt%). Conditions: Photocatalyst concentration 0.15g/L, 2.0 v/v% ethanol, pH=4 ± 0.05 and near-UV Light. Standard deviation: (a) ±5.0% and (b)±4.0%.

Figure 35 shows that the Pluronic F-127 template has a greater impact than the Pluronic P-123 template, on the photoactivity, increasing the hydrogen production up to 86%. This agrees with the enhanced surface area and porosity of the mesoporous TiO₂ synthesized with Pluronic F-127, as reported in Chapter 4.

One can notice that in all cases, the cumulative hydrogen production for Pt-TiO₂ photocatalyst synthesized using Pluronic F-127 and Pluronic P-12 templates, follow during the 6 hours of irradiation a zero-order reaction, showing a very stable photocatalytic performance.

Thus, considering the Pluronic F-127 advantage over Pluronic P-123 for hydrogen production, further experiments of the present study were carried out using only copolymer Pluronic F-127.

6.2.2 Effect of Platinum and Palladium on Hydrogen production

Two noble metals (platinum and palladium) were used as co-catalyst to dope the structure of the TiO₂ photocatalyst. These metals enhance the hydrogen production, as compared to the undoped mesoporous TiO₂. Nobel metal crystallites reduce the band gap and facilitate electron capture[164]. As a result, Pt and Pd reduce the recombination between holes and electrons, promoting better photocatalytic water splitting performances[165].

Figure 36 reports the influence of Pt and Pd on TiO₂ in terms of cumulative hydrogen volume.

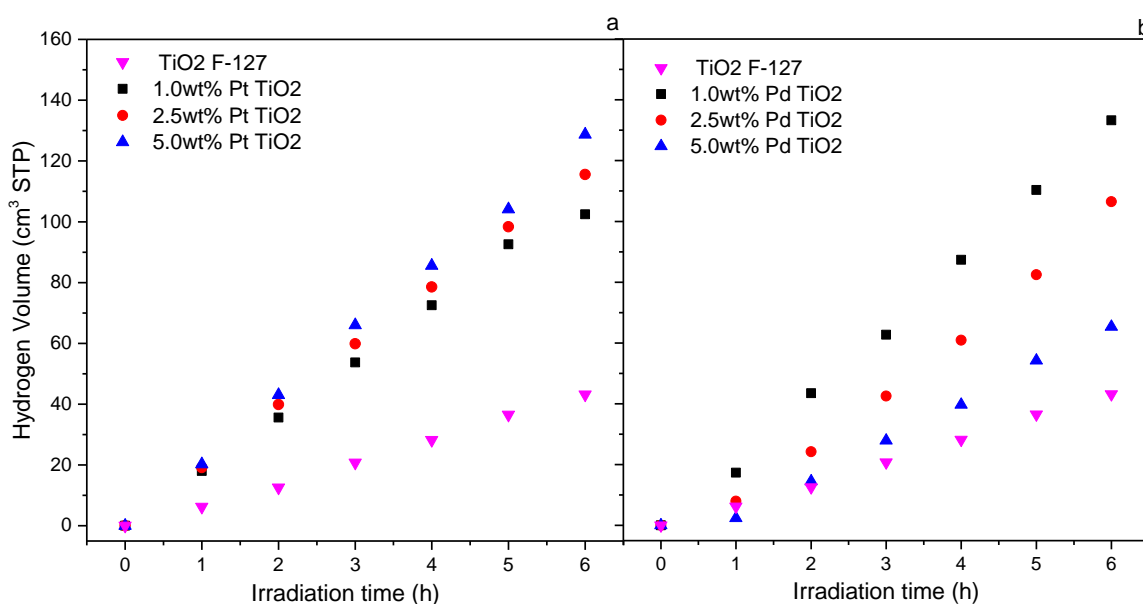


Figure 36 Cumulative Hydrogen Volume using Co-Catalysts (a) Pt and (b) Pd at Different Platinum Loadings (1.0, 2.5 and 5.0wt%). Conditions: Photocatalyst concentration 0.15g/L, 2.0 v/v% ethanol, pH=4 ± 0.05 and near-UV Light. Standard deviation: (a)±4.0% (b)±3.0% respectively.

Figure 36 shows that for platinum, there is a maximum volume of hydrogen produced using 5.0wt%Pt on TiO₂ (130 cm³). However, this result is only slightly higher than the maximum volume of hydrogen produced when using 2.5wt% and 1.0wt%Pt-TiO₂, and 3 times the volume of hydrogen with undoped TiO₂.

Contrary to platinum, palladium displays a different trend. The smallest 1.0wt% Pd on TiO₂ showed comparable performance to the highest 5.0wt% Pt on TiO₂. These favourable hydrogen production rates with Pd are decreased however, at higher Pd loadings. The Irradiation Macroscopic Energy Balance provides an explanation showing that at the higher Pd loadings, there is more important irradiation backscattering, with greater irradiation reflection and reduced light absorption. This diminished irradiation absorption negatively affect the photocatalyst performance[166].

In agreement with this, at the lowest palladium loadings (1.0wt%) good metal dispersion, good specific surface area and adequate pore structure were observed [167]. Contrary to this at 2.5 and 5.0wt% Pd-TiO₂, poorer metal dispersion with larger metal crystallite sizes were noticed, with this leading to a lower photocatalytic activity [168].

In all cases, platinum and palladium doped TiO₂ showed a steady linear trend. The hydrogen production rate displayed consistent zero-order kinetics, with no noticeable photocatalytic decay. This showed that both materials are stable for extended irradiation periods and no apparent deactivation for 24 hours[163].

These results demonstrate that palladium at 1.0wt% loading; can reach valuable hydrogen yields, showing to be an excellent replacement for Pt. As well, Pd use can be considered more advantageous than Pt, given that Pd is less expensive (only 20-25% of the cost of platinum). Furthermore, and given the premise of nominal 1.0wt% Pd-TiO₂, Pd loadings were confirmed with X-Ray-Fluorescence Spectrometry (XRF), with 1.17wt% Pd onto mesoporous TiO₂ was obtained.

6.2.3 Effect of Catalyst Concentration on Hydrogen Production

Considering that 1.0wt%Pd-TiO₂ showed the best performance in terms of hydrogen production, additional experiments were carried out to determine the influence of the catalyst concentration during photoreaction.

Figure 37 displays four different concentrations of catalyst: 0.15, 0.30, 0.50 and 1.00 g/L, studied during 6 hours of irradiation. One can observe that the runs with 1.00g/L showed the highest hydrogen production. Thus, it can be considered that when higher photocatalyst concentrations in the slurry are used, more photocatalyst electron-holes are provided, with this promoting better hydrogen production.

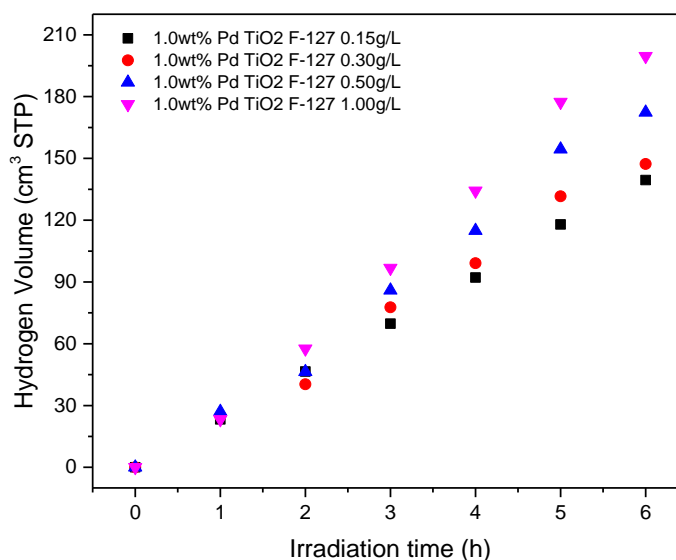


Figure 37 Cumulative Hydrogen Production using 1.0wt% Pd-TiO₂ at Different Catalyst Concentrations (0.15, 0.30, 0.50 and 1.0 g/L). Conditions: 2.0 v/v% ethanol, pH=4 ± 0.05 and UV Light. Standard deviation: ±4.0%

As a result, it was observed that the hydrogen production rate increased 54% when photocatalyst concentration was augmented seven (7) times from 0.15 to 1.00 g/L. However, and despite this hydrogen production increase, it could be considered a modest improvement given the photocatalyst cost was augmented 7 times as well. Therefore, a photocatalyst concentration of 0.15g/L was kept as the best choice for photocatalyst concentration for further experimentation.

6.2.4 Effect of Photo-CREC Water II Atmosphere. Argon and CO₂.

Before starting water splitting runs, the reactor gas chamber was purged with inert gas to remove oxygen from air, avoiding combustion reactions. Argon was used initially as the inert gas due to Ar is heavier than oxygen and facilitates its displacement [169]. On the other hand, CO₂ was also used in separate runs in the reactor gas chamber to determine its possible influence on water dissociation reactions.

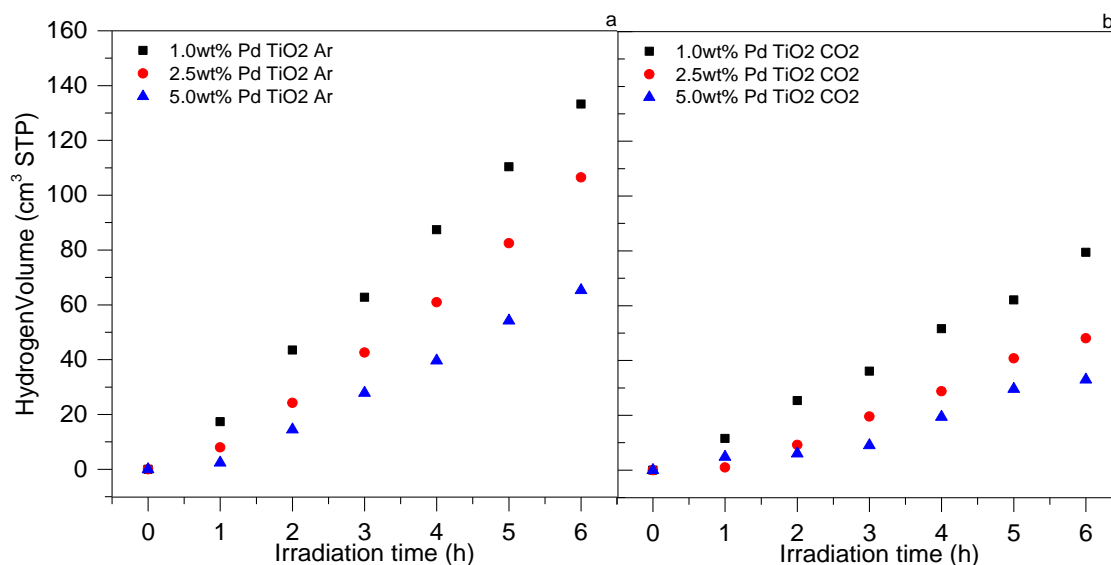


Figure 38 Cumulative Hydrogen Production using xPd-TiO₂ (x=1.0, 2.5 And 5.0wt%) and Under: Two Atmospheres a) argon and (b) CO₂. Conditions: Photocatalyst concentration 0.15g/L, 2.0 v/v% ethanol, pH=4 ± 0.05 and near-UV Light. Standard Deviation: (a) ±3.0%, (b)±3.4% respectively.

According to Figure 38, using argon as an inert gas and utilizing 1.0wt% Pd-TiO₂, yielded 130 STP cm³ of hydrogen after 6 hours of irradiation. On the other hand, a CO₂ atmosphere was employed, only 80 STP cm³ of hydrogen were obtained.

One should note that under a CO₂ atmosphere and due to the competition of the CO₂ photoreduction with hydrogen production, a lower net hydrogen formation was obtained.

Figure 39 reports the CO₂ evolution during the 6 hours of irradiation. CO₂ increases steadily under an argon atmosphere, while remaining essentially unchanged under a CO₂

atmosphere. These findings support the view that there is competition between CO₂ photoreduction and CO₂ formation via ethanol OH[•] radical scavenging.

It is assumed, that these gas phase CO₂ findings could be also be influenced by the enhanced CO₂ solubility in water-ethanol as reported by others[170].

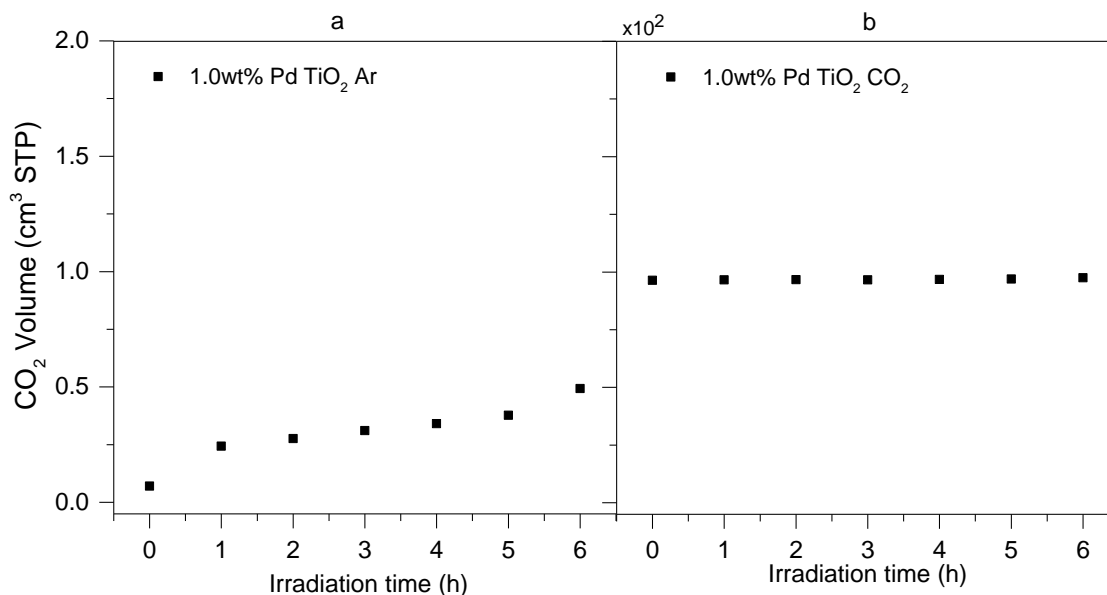


Figure 39 CO₂ Production using 1.0wt% Pd-TiO₂ and Under Two Atmospheres: (a) Argon (b)CO₂. Conditions: Photocatalyst concentration 0.15g/L, 2.0 v/v% ethanol, pH=4 ± 0.05 and UV Light. Standard Deviation: (a) ±4.6%, (b) ±3.5%.

Additional experimentation was performed under a CO₂ atmosphere by doubling the ethanol concentration from 2.0% to 4.0% v/v. It was anticipated that the use of higher ethanol concentrations may further enhance CO₂ solubility, influencing the gas phase CO₂ reduction. To study these effects, methane main byproduct of CO₂ photoreduction was carefully monitored [171].

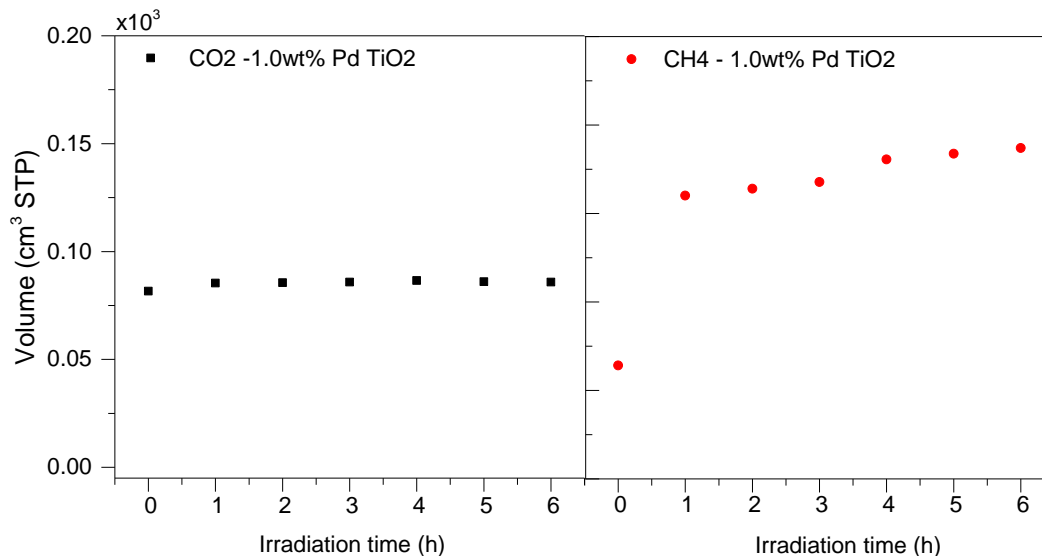


Figure 40 CO₂ and CH₄ Volume using 1.0wt% Pd-TiO₂ under a CO₂ atmosphere. Reaction Conditions: Photocatalyst concentration 0.15g/L, 4.0 v/v% ethanol, pH=4 ± 0.05 and UV Light. Standard Deviation: (a) ±4.6%, (b) 4.2%.

Figure 40 reports both the CO₂ changes, showing that CO₂ remains essentially unchanged while irradiation time is progressing. This indicates that both the formation and the consumption of CO₂ are in balance. However, if near UV irradiation is extended to 24 h, a slight 6.0% drop of CO₂ was observed. Nonetheless and regarding methane, it was noticed that methane increased significantly from 0.00011 cm³ up to 0.28 cm³ after this irradiation time.

These results are in agreement with Pd on TiO₂ as illustrated in Figure 40, having both CO₂ reduction and ethanol scavenger OH radical activity, with its positive and negative redox potentials in the VB and CB, minimizing e⁻ and h⁺ recombination [172].

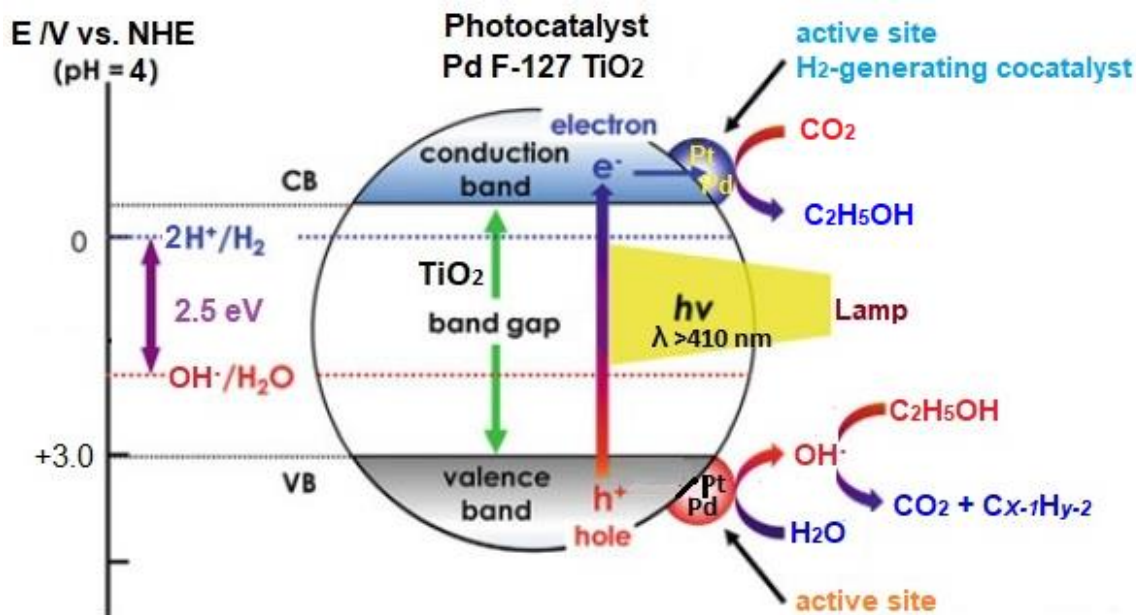


Figure 41 Schematic of TiO₂ photocatalyzed reaction for CO₂ photoreduction

Two main reactions can contribute to CO₂ photoreduction: a) CO₂ deoxygenation and b) CO₂ hydrogenation (Table 20). If CO₂ deoxygenation occurs, methane is most likely to be the chemical species to be formed. This phenomenon encompasses the generation of C radicals that recombine with the hydrogen. However, once CO₂ is absorbed in water, CO₂ can be reduced forming acetaldehyde and ethanol, as is shown in Figure 42[173].

Table 20 Proposed reaction mechanism of CO₂ reduction [174]

Reaction
$\text{H}_2\text{O}_{(\text{ads})} \xrightarrow{\text{TiO}_2\text{-Pd}} \text{H}_{(\text{ads})}^+ + \text{OH}_{(\text{ads})}^-$
$\text{H}_{(\text{ads})}^+ + \text{e}^- \xrightarrow{\text{TiO}_2\text{-Pd}} \text{H}\cdot$
$\text{H}\cdot \xrightarrow{\text{TiO}_2\text{-Pd}} \frac{1}{2} \text{H}_2(\text{g})$
$\text{CO}_2 \xrightarrow{\text{deoxygenation}} \text{C}\cdot + \text{O}_2 \xrightarrow{\text{H}^+} \text{CH}_4$
$\text{CO}_2 + \text{e}^- \xrightarrow{\text{TiO}_2\text{-Pd}} \text{CO}_2^-$

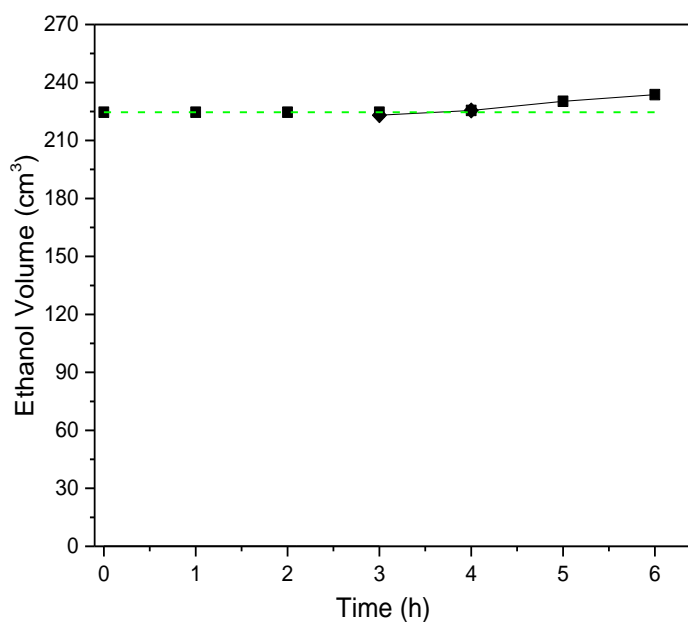
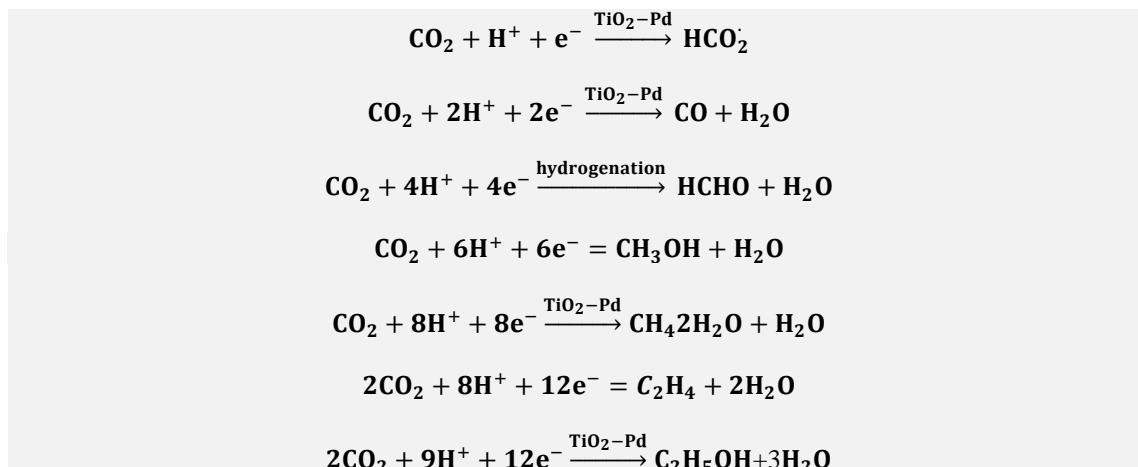


Figure 42 Ethanol Volume in the Liquid Phase under a CO₂ Atmosphere using 1.0wt% Pd-TiO₂. Conditions: Photocatalyst concentration 0.15g/L, 4.0 v/v% ethanol, pH=4 ± 0.05 and near-UV Light. Standard deviation: ±6.5%

6.2.5 Effect of Sacrificial Agent Concentration on Hydrogen Production

Ethanol as a scavenger offers important advantages such as photogeneration of electron-holes, limiting electron-site recombination and improving photocatalytical activity. Ethanol can donate electrons to scavenge the valence holes and suppress the reverse reaction[175].

Experiments were performed at 1.0wt% Pd and three (3) ethanol concentrations (1, 2, 4% v/v) under an argon atmosphere and with 0.15g/L of photocatalyst concentration. This was done to evaluate the effect of the ethanol concentration on hydrogen production. Figure 43 reports the influence of increasing ethanol from 2.0 – 4.0% on hydrogen production rates.

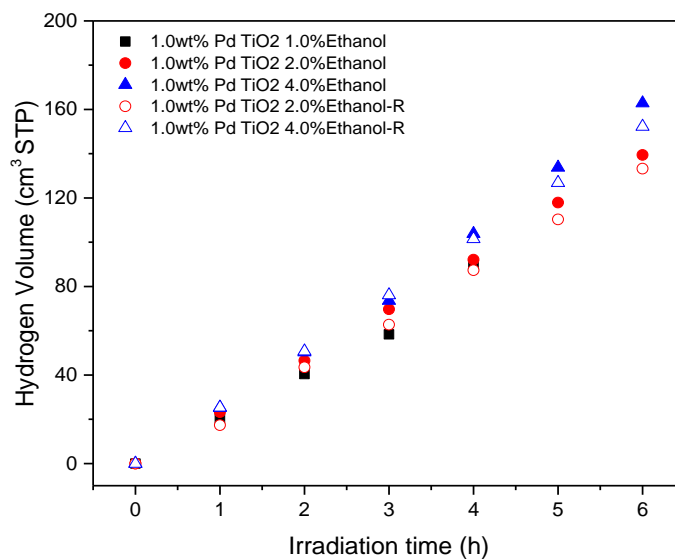


Figure 43 Hydrogen Volume Using 1.0wt% Pd at 1.0, 2.0 and 4.0%v/v Ethanol. Conditions: Photocatalyst concentration 0.15g/L, argon atmosphere, pH=4 ± 0.05 and UV Light, R= repeat. Standard deviation: ±6.5%.

As shown in Figure 43, the highest hydrogen formation rate was obtained at the highest ethanol concentration. However, these important ethanol concentrations changes, did not influence hydrogen production significantly. This was particularly true between 2.0 and 4.0% v/v/ ethanol concentration. Therefore, 2.0% v/v was considered fully adequate and was the selected concentration of the ethanol scavenger used for further studies.

6.2.6 By-products Formation during the Photocatalytic Hydrogen Production

There are several by-products generated from the water splitting reaction in the gas phase. By-products include methane, ethane, acetaldehyde and CO₂. To quantify these by-products gas samples were taken hourly from the gas port located in the storage tank. They

were analyzed using a gas chromatograph unit (GC). All the experiments were repeated three (3) times to secure reproducibility.

One can thus see, that as soon as the photo-redox reaction starts, all these by-products together with hydrogen increase progressively as is shown in Figure 44.

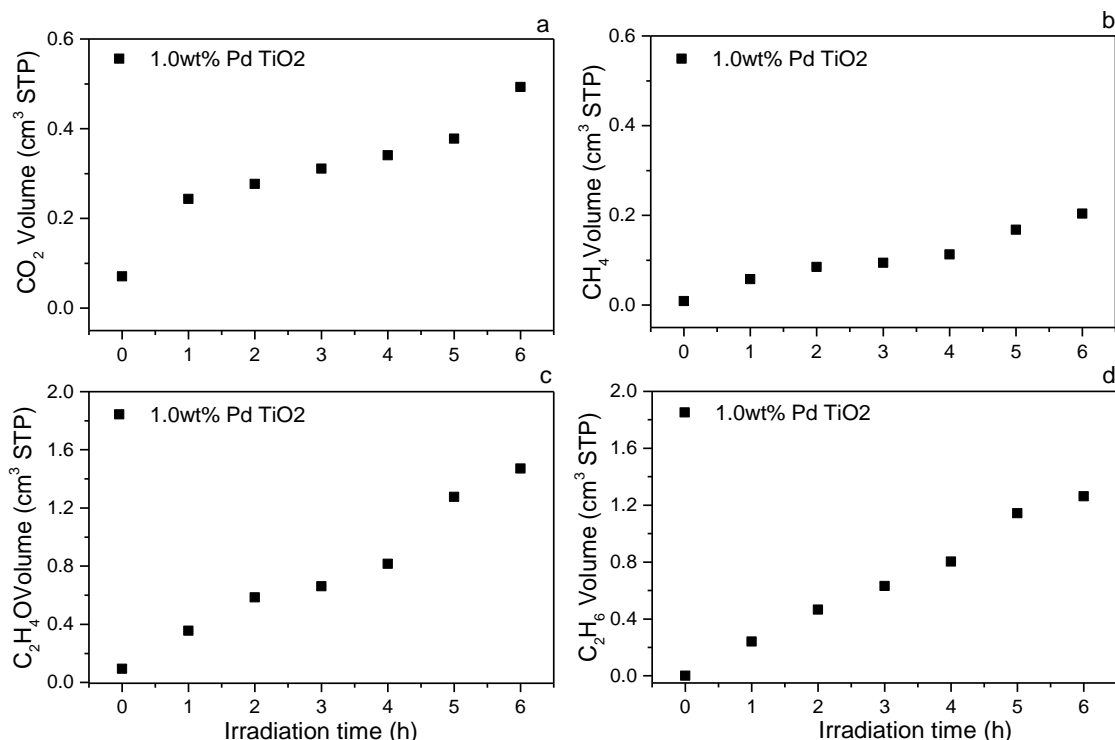


Figure 44 Hydrocarbon Profiles of a) Carbon dioxide (CO₂), b) Methane (CH₄), c) Acetaldehyde (C₂H₄O) and d) Ethane (C₂H₆) at 1.0wt% Pd. Conditions: Photocatalyst concentration 0.15g/L, 2.0 v/v% ethanol, argon Atmosphere, pH=4 ± 0.05 and UV Light. Standard Deviation: (a)±4.1%, (b) ±4.7%, (c) ±5.1%, (d) ±6.3%.

The formation of various chemical species produced, as a result of water splitting using ethanol as a scavenger, can be described using a series-parallel reaction network as shown in Figure 34 and Table 19.

In the liquid phase, ethanol was also measured using the UFLC (Ultra-Fast Liquid Chromatography). Figure 45 displays the essentially unchanged ethanol concentration during the 6 hours of irradiation. Thus, one can observe a balanced consumption-formation of ethanol, with a net stable ethanol concentration. This is the case while hydrogen is being produced using the 1.0wt% Pd-TiO₂ photocatalyst.

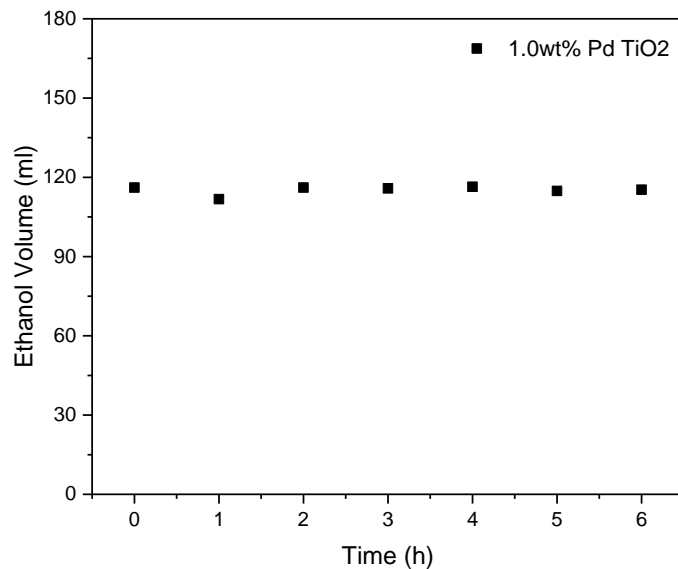


Figure 45 Ethanol Changes with Irradiation Time. Conditions: Photocatalyst concentration 0.15g/L, argon atmosphere, 2.0 v/v% ethanol, pH=4 \pm 0.05 and UV Light. Standard deviation: \pm 3.0%.

In our view, this is a promising result of the study, showing that no additional scavenger is required once the initial ethanol is fed to the Photo-CREC Water II unit.

6.3 Hydrogen Production under Visible Light

Considering that the sun is a renewable and inexhaustible source of energy, it is advantageous to use it for photocatalytic processes. Until today, platinum has been the metal most widely used for this purpose. Metals such as palladium are also under investigation. This is due to its similarity to platinum, in terms of chemical properties, with the advantage of being less expensive[176].

TiO₂-based photocatalysts have been considered to increase the visible light absorption and to improve the production of hydrogen as an energy carrier. Doping noble metals such as platinum and palladium appeared to provide this window of opportunity.

Noble metals can be incorporated in a titanium precursor sol gel, yielding a semiconductor that can be activated under visible light for hydrogen production. Figure 46 reports the

cumulative hydrogen volume produced when using TiO₂ doped by Pt and Pd at different metal loadings.

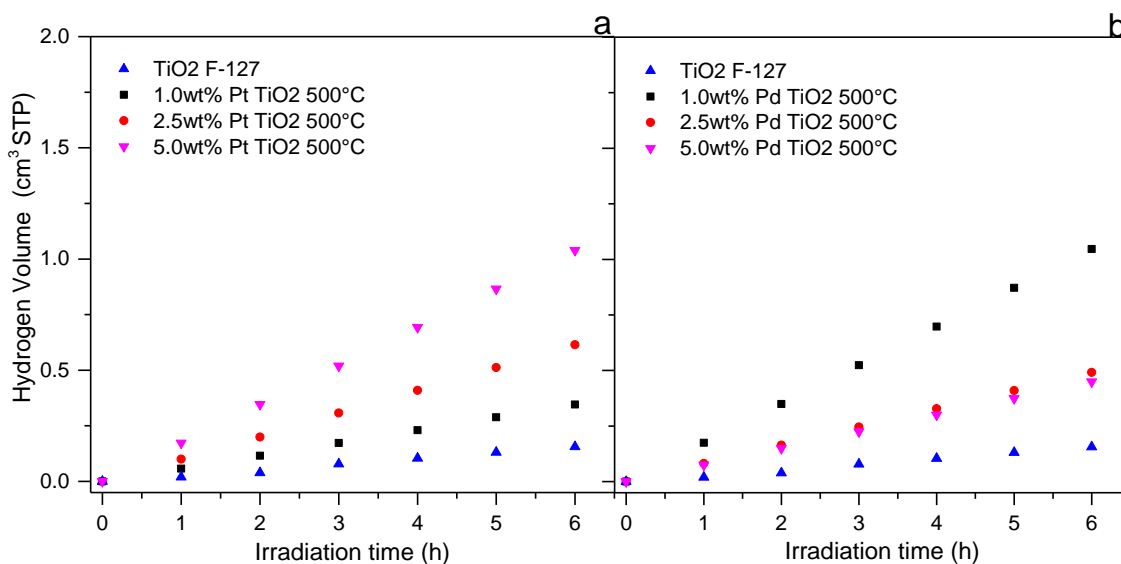


Figure 46 Cumulative Hydrogen Volume Produced when using Co-Catalysts (a) Pt and (b) Pd at Different Loadings (1.0, 2.5 and 5.0wt%). Conditions: Photocatalyst concentration: 0.15g/L, 2.0 v/v% ethanol, pH=4 ± 0.05 and visible light. Standard deviation: ±3.0%

Figure 46 reports that Pt-TiO₂ exhibits a substantial visible light photoactivity enhancement for hydrogen production. This is the case while compared to undoped TiO₂. The best performance is given by 5.0wt% Pt. This mesoporous semiconductor may have increased the scavenging effect of photogenerated electrons and therefore, prevented the recombination of electron-hole pairs[177].

For Pd-TiO₂, when metal loading is increased from 1 to 2.5 and 5.0wt% Pd, a decreased rate of hydrogen produced is obtained. This suggests that the trap of electrons from the 2.5 and 5.0wt% Pd semiconductors is not as effective as that for the 1.0wt%Pd-TiO₂. One should notice as well, that the Radiation Macroscopic Energy Balances for the irradiation slurries using these photocatalysts, show a reduced visible light absorption at the higher Pd loadings. This consequently causes less electrons and holes pairs to be generated.

Therefore, there is a lesser number of available electrons to combine with H^+ , and as a result a smaller possible contribution from the first hydrogen radical formation step [178].

6.3.1 Photocatalysts Photoreduction

Platinum and palladium are both present in a metallic state during the sol-gel photocatalyst preparation. However, they are oxidised during the calcination step. As a result, the noble metal doping the semiconductor, must be reduced again evolving from PtO_2 or Pt_3O_4 to Pt^0 in the case of platinum. Nevertheless, palladium metal reduction is not fully achieved under the temperature and conditions selected (refer to Chapter 3).

Furthermore, in the case of the $Pd-TiO_2$ powder, it showed a reddish colour after the photocatalyst preparation indicating the presence of palladium oxide. A X-Ray Diffraction Analysis was carried out and a peak at 33.5° (111) in the 2θ angle confirmed the presence of PdO .

As a result, a different methodology must be considered to ensure that both platinum and palladium were appropriately reduced. A BLB UV-Lamp was employed for 1 hour to photoreduce the semiconductors. Following this, the near-UV lamp was replaced by a visible light lamp. It was then observed, that when photocatalysts were first photoreduced using near-UV, they led under visible light irradiation to an important increase in hydrogen production.

It is speculated that photocatalyst photoreduction takes place very efficiently when photogenerated electrons migrates to the TiO_2 surface. They reduce PdO into Pd^0 yielding O_2 . The process continues until all PdO is reduced to Pd^0 [179].

Figure 47 displays an enhanced cumulative hydrogen production under visible light using a pre-photoreduced (using near UV-light) noble metal loaded mesoporous photocatalysts. One can notice a stable zero-order reaction rate through the entire irradiation period.

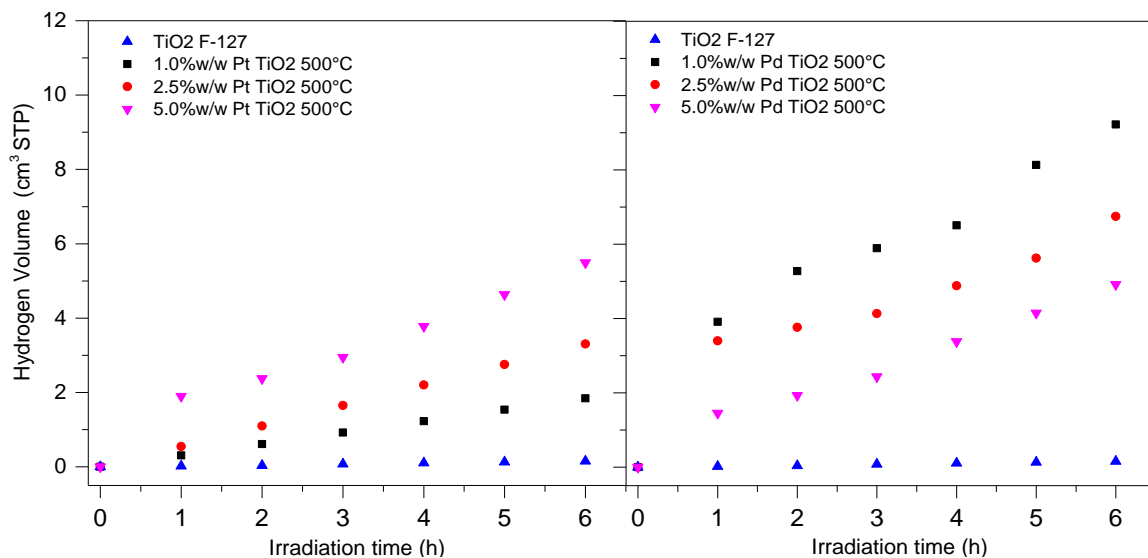


Figure 47 Cumulative Hydrogen Volume using Co-Catalysts (a) Pt and (b) Pd at Different Platinum Loadings (1.0, 2.5 and 5.0wt%). Conditions: Photocatalyst concentration: 0.15g/L, 2.0 v/v% ethanol, pH=4 ± 0.05, visible light and near-UV photoreduction. Standard deviation: ±2.4%

Furthermore, one can observe that when Pt/Pd-TiO₂ photocatalysts were photoreduced, and subsequently used in the Photo-CREC Water Reactor-II at different loadings (1.0, 2.5 and 5.0wt%) under visible light, the 5.0wt% Pt-TiO₂ and the 1.0wt% Pd-TiO₂ showed optimum cumulative hydrogen values. It was interesting to see that the same consistent trend, as observed with near-UV light in section 6.2.2, was now recorded with visible light: a) The higher the Pt loadings, the higher hydrogen production, b) The lower Pd the loadings, the higher hydrogen production.

When comparing Figure 46 and Figure 47, it can be observed that both Pt-TiO₂ and Pd-TiO₂ require noble metal photoreduction to achieve increased hydrogen production rates. In particular and for 1.0wt% Pd-TiO₂ the maximum hydrogen volume produced reached 9.2 cm³.

To explain these results, one can consider that under visible light and using a Pd-TiO₂ photocatalyst, photons are both absorbed and scattered. The irradiation macroscopic energy balance as reported in Chapter 5, showed that higher Pd loadings (2.5 and 5.0wt%- Pd) do

not enhance the absorption of visible light but diminish it. This phenomenon observed for Pd at the higher metal loadings can be assigned to the presence of larger metal crystallites and TiO₂ particle agglomeration, limiting light absorption from reaching the active metallic sites[180].

On the other hand, it can be hypothesized as well that less effective photoreduction of palladium may have happened for 2.5 and 5.0wt% Pd. This could be due to the oversupply of the noble metal. Layers of PdO could still be present on TiO₂ decreasing as a result, the light absorption. Formation of such sites may increase the photocatalyst reflectivity leading to a visible light scattering [181].

As well as hydrogen production under visible light, the photogenerated holes created by the noble metals (Pt and Pd) reacted with the organic scavenger ethanol forming acetaldehyde, ethane, CO₂ and methane as it is shown in Figure 48.

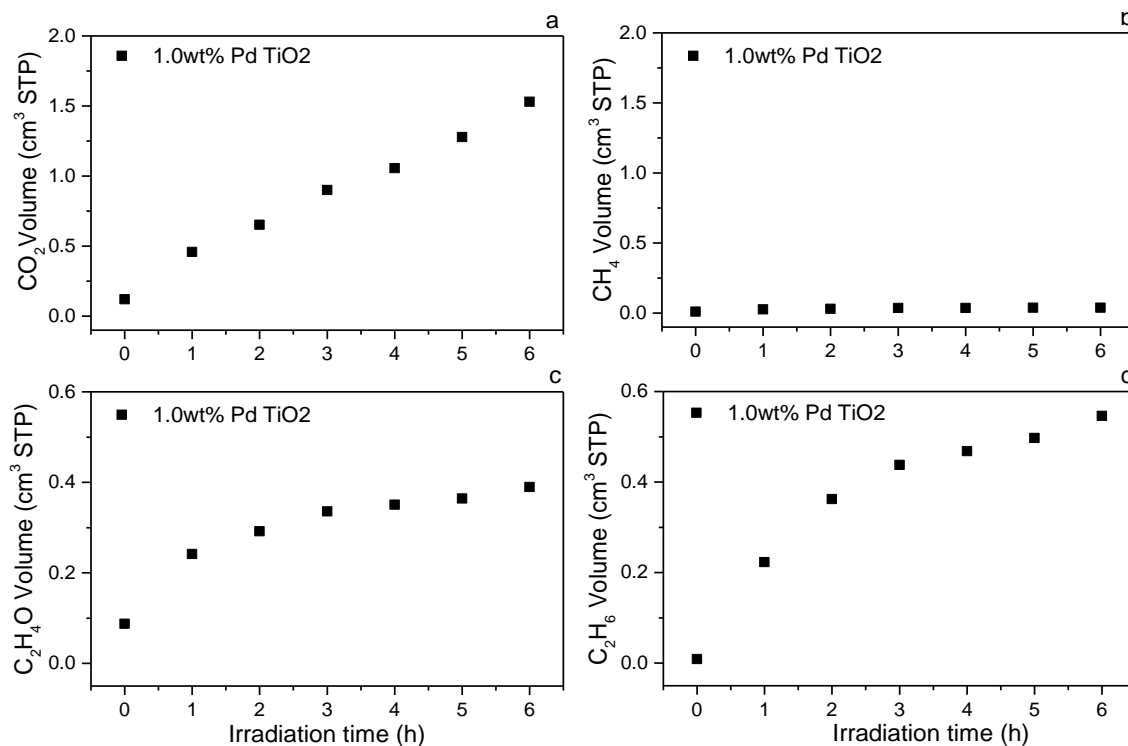


Figure 48 By-product Changes with Irradiation Time: a) Carbon dioxide (CO₂), b) Methane (CH₄), c) Ethane (C₂H₆) and d) Acetaldehyde(C₂H₄O) at 1.0% w/w Pd. Conditions: Photocatalyst concentration: 0.15g/L, 2.0 v/v% ethanol, argon atmosphere, pH=4 ± 0.05 and visible light. Standard deviation: (a) ±7.0%, (b) ±5.5%, (c) ±5.2%, (d) ±6.3%.

In this case as well, the liquid phase was analyzed during the 6-hour irradiation period using the UFLC (Ultra fast liquid chromatography). Under visible light, the ethanol scavenger showed a similar trend as under near-UV light, with its concentration remaining essentially unchanged. The data reported in Figure 49 suggests again a balanced generation-consumption of the ethanol scavenger.

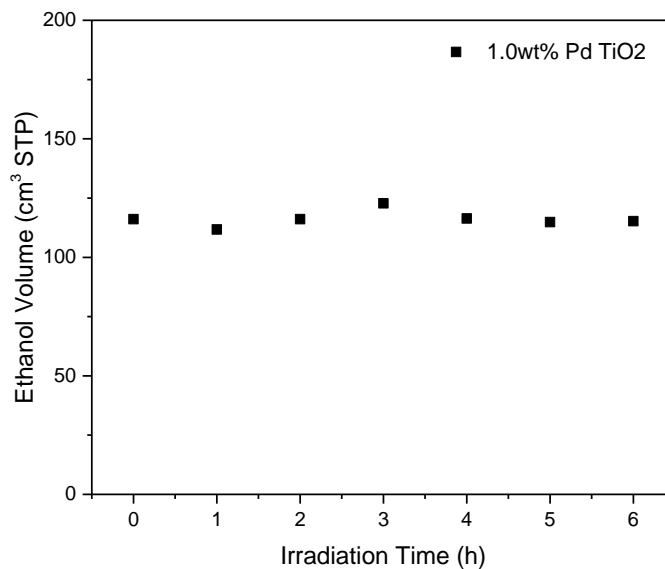


Figure 49 Ethanol Concentration Changes with Irradiation Time. Conditions: Photocatalyst concentration: 0.15g/L, argon atmosphere, 2.0 v/v% ethanol, pH=4 ± 0.05 and visible light. Standard deviation: ±3.5%

6.4 Conclusions

This chapter describes the effect of different parameters for photocatalytic hydrogen production via water splitting. The following are the most important conclusions:

- a) The Pluronic F-127 copolymer precursor provides a semiconductor with superior hydrogen production performance and this with respect to the one synthesized with the Pluronic P-123 copolymer. The hydrogen production difference is assigned to the more adequate physical properties of the resulting mesoporous TiO₂.
- b) Addition of noble metals (platinum and palladium) enhances hydrogen formation with palladium showing the best performance at the lowest metal loading.
- c) Ethanol is an effective OH radical scavenger for photocatalytic hydrogen production, with methane, ethane, CO₂ and acetaldehyde were the main resulting by-products.
- d) Hydrogen production displays in all cases a stable and zero-order kinetics.
- e) Composition of the gas chamber has a significant influence on hydrogen formation with an Ar inert atmosphere providing the best option. An initial CO₂ atmosphere favours higher methane formation.
- f) Increase of photocatalyst concentration up to 1.0g/L yields only a modest improvement in the hydrogen formation rates.
- g) Both Pd and Pt on TiO₂ require a prior photoreduction, to enhance their photocatalytic performance when exposed to visible light.

Chapter 7

7 Quantum Yield (QY) evaluation

The Quantum Yield (QY) is the most important parameter to establish the energy utilization efficiency in photocatalytic reactors. This efficiency can be assessed using the ratio of the photogenerated radical rate over the absorbed photon rate [182].

In terms of hydrogen production, a quantum yield can be defined as the hydrogen radical production rate over the absorbed photon rate on the photocatalyst surface. According to this definition, a QY can be determined as follows:

$$QY_{H\bullet} = \frac{\text{moles of } H\bullet/s}{\text{moles of photons absorbed by the photocatalyst/s}} \quad \text{Equation 17}$$

Equation 15 is equivalent to;

$$\%QY = \frac{\left[\frac{dN_{H\bullet}}{dt} \right]}{Pa} \times 100 \quad \text{Equation 18}$$

where $\frac{dN_{H\bullet}}{dt}$ represents the rate of moles of hydrogen radicals formed at any time during the photocatalyst irradiation.

To use Equation 18, the rate of moles of photons absorbed by the photocatalyst, require the assessment of Pa . This can be accomplished using Irradiation Macroscopic Energy Balance (IMEB) in the Photo CREC Water Reactor II as proposed by Escobedo, et al[102]. Appendix B provides a calculation sample to assess the QY.

7.1 Effect of noble metals (Pt and Pd) on Quantum Yields under UV light

The Quantum Yield evaluation for the different TiO₂ photocatalysts of the present study involved rigorous macroscopic irradiation balances. These calculations require the assessment of the P_t transmitted, the P_i incident, and the P_{bs} backscattered photons using

the IMEB. With this information and using Equation 12 from Chapter 5, the P_a was calculated.

Furthermore, for every experiment and once the lamp (either near-UV or visible) is turned on, the rate of moles of hydrogen, $\frac{dN_{H_2}}{dt}$ can be established using $\frac{dN_{H_2}}{dt}$. On this basis, the QY% can be calculated using Equation 18.

Table 21 and Figure 50 report the QYs% for the mesoporous photocatalysts doped with platinum or palladium at different metal loadings (1.0, 2.5 and 5.0wt %) under the following conditions: a) Photocatalyst slurry concentrations of 0.15g/L, b) 2.0 v/v% Ethanol, c) pH=4 \pm 0.05 and d) Near-UV Light.

Table 21 Quantum Yield for the Pd/Pt-TiO₂ photocatalyst when using 0.15g/L.

All reported data are average values of 3 repeats. Standard deviation: \pm 4.5%.

Semiconductor	QY (%)
TiO ₂ F-127	5.02
1.0wt% Pt TiO ₂	8.49
2.5wt% Pt TiO ₂	9.16
5.0wt% Pt TiO ₂	10.20
1.0wt% Pd TiO ₂	10.88
2.5wt% Pd TiO ₂	9.59
5.0wt% Pd TiO ₂	8.48

One can observe in Table 21, that Pt addition produces a QY% increase from 5.02% to 8.5-10.2%. These results are in line with the QY% of 7.9% reported by Escobedo[102] for DP25 doped with 1.0wt% Pt. Additionally, it was noticed that further Pt addition, up to 5.0wt%, led to a higher QY% of 10.2%.

On the other hand, regarding Pd addition, a different trend was observed. First, there was a significant increase of QY% with 1.0wt% Pd TiO₂, higher Pd levels led to a decrease of QY% ranging from 10.88% to 8.48%.

Figure 50 reports that QY% changes were consistent for both Pt-doped and Pd-doped TiO₂ photocatalysts: a) During the first hour of irradiation, the QY% increased progressively

until it reached a stable value, b) During the following 5 hours of irradiation, the QY% remained unchanged, with this showing a steady performance of the photocatalysts under study.

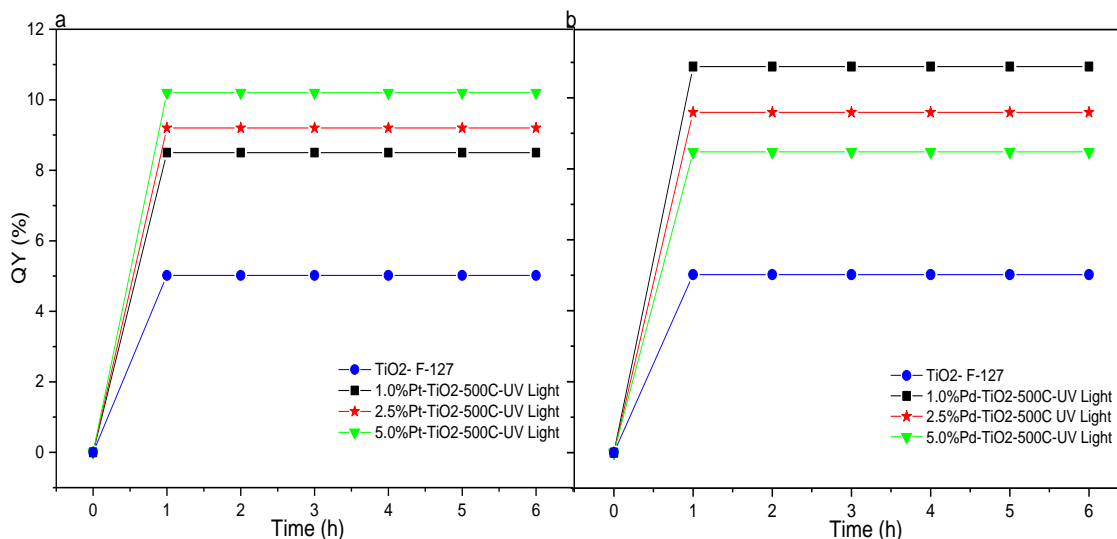


Figure 50 QY% at various irradiation times under UV light and 0.15g/L of photocatalyst concentration using co-catalysts Pt (a) and Pd (b) at different Platinum loadings (1.0, 2.5 and 5.0wt%). Standard deviation on repeats: $\pm 4.5\%$.

7.2 Effect of catalyst concentration on Quantum Yields under Near UV light

Considering the promising QY% observed for 1.0wt% Pd-TiO₂ during hydrogen production, further QY% evaluations were developed, by changing the photocatalyst concentration in the slurry. Table 22 and Figure 51 report the QY% obtained, by augmenting the photocatalyst concentration, under the following conditions: a) 2.0 v/v% ethanol as scavenger compound, b) pH=4 \pm 0.05 and c) Near-UV light irradiation.

Table 22 Quantum Yield for 1.0wt% Pd -TiO₂ photocatalyst at different photocatalyst concentrations. All reported data are average values of 3 repeats. Standard deviation: $\pm 4.0\%$.

Catalyst concentration (g/L)	QY (%)
0.15	10.88
0.30	14.49
0.50	22.38
1.00	30.80

Figure 51 provides additional details of the QY% for different photocatalyst concentrations. Here, it was again observed that there was a noticeable increase of the QY% in the first hour of irradiation, followed by a stable QY% in the next 5 hours of irradiation. These constant QYs% during the 1 to 6-hour irradiation period were assigned to the steady hydrogen formation rate, linked to a zero-order reaction kinetics.

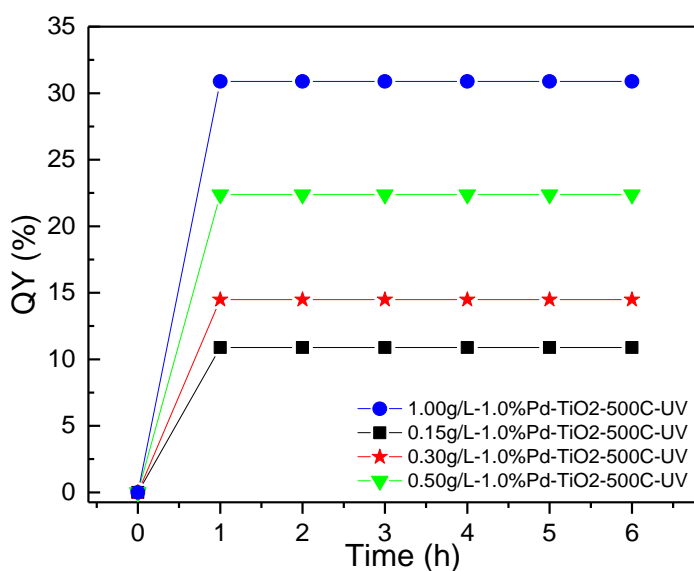


Figure 51 QY% at Various Irradiation Times using Near-UV irradiation and 0.15, 0.30, 0.50 and 1.00 g/L of photocatalyst Concentrations. Note: a) 1.0wt%-Pd on TiO₂. Standard deviation on repeats: $\pm 4.0\%$.

7.1 Effect of noble metals (Pt and Pd) on Quantum Yields under Visible light

There is still controversy about the possible TiO₂ activation using visible light. This is significant given that solar light contains only 4.0% of near-UV light. This unquestionably represents an obstacle in the production of hydrogen using visible light[183]. Different alternatives have been investigated using dopants to activate semiconductors, such as N-TiO₂, TiO₂: Ni/(Ta, Nb) and CaIn₂S₄[184] [185][186]. However, our approach has been addressed using noble metals such as Pt and Pd, given their anticipated stability for hydrogen production in acidulated water with a pH=4.

Table 23 and Figure 52 report the QYs% under visible light, for Pd-TiO₂ and Pt-TiO₂. Regarding these QY% evaluations, two approaches were considered: a) The photocatalyst was irradiated with visible light from the very beginning, and b) The photocatalyst was pre-reduced under near-UV light for 1 hour prior to the irradiation with visible light. For both cases, the reaction conditions selected for the photocatalyst evaluation were as follows: a) noble metal loadings (1.0, 2.5 and 5.0wt%), b) photocatalyst concentration in the slurry at 0.15g/L, c) 2.0 v/v% ethanol and d) pH=4 ± 0.05.

Table 23 QYs% for Pd-TiO₂ and Pt-TiO₂ Photocatalysts at Different Metal Loadings (1.0, 2.5, and 5.0wt%) under: a) Visible light irradiation only, b) Using Near-UV Light followed by Visible Light irradiation. All reported data are average values of 3 repeats. Standard deviation: a) ±3.0% and b) ±2.4%

Photocatalyst	(a) QY (%) (Visible Light Irradiation only)	(b) QY (%) (Near UV Light first followed by Visible Light Irradiation)
TiO ₂ F-127	0.11	0.11
1.0wt% Pt TiO ₂	0.13	0.73
2.5wt% Pt TiO ₂	0.15	0.81
5.0wt% Pt TiO ₂	0.16	0.85
1.0wt% Pd TiO ₂	0.09	1.16
2.5wt% Pd TiO ₂	0.07	1.08
5.0wt% Pd TiO ₂	0.07	0.84

One can observe in Table 23, that for all prepared Pt-TiO₂ and Pd-TiO₂ photocatalysts, the QYs% obtained while being irradiated with visible light were low QYs% in the 0.07-0.16% range and comparable to those for undoped TiO₂. These very low QYs% were assigned to the lack of ability of the Pt-TiO₂ and Pd-TiO₂ photocatalyst to produce hydrogen under visible light.

However, Table 23 and Figure 53 also show that when the photocatalysts were pre-reduced with near-UV irradiation, the QYs% significantly increased, reaching QY% values as high as 1.16%. These results demonstrate the critical importance of the noble metal pre-reduction using near UV irradiation (photoreduction). One should note that pre-reduction was critical for both the Pt-TiO₂ and Pd-TiO₂ photocatalysts, making them active under visible light for hydrogen production.

In this respect, few papers in the technical literature report quantum yields of similar magnitude. Fontelles et al, used, platinum supported on Nb-TiO₂ (2.89 wt% Nb on TiO₂) as a photocatalyst, achieving a maximum quantum yield of 3.0% [187]. One should note that this quantum yield was reported using a QY% definition from IUPAC, which involves the rate of hydrogen produced over the number of absorbed photons [105]. Thus, this QY% is about to 3-5 times the QY% of the present study, based on moles of H[•] produced.

However, one should consider Fontelles et al [187] results with caution, given that the absorbed photon rates were not measured directly but calculated using a numerical solution of a radiation equation. These modeled absorption rates could involve significant errors. As stated before and in contrast to this, in the present study the QYs% were determined using an experimentally evaluated P_a , determined from IMEB macroscopic balances, as reported in Chapter 5.

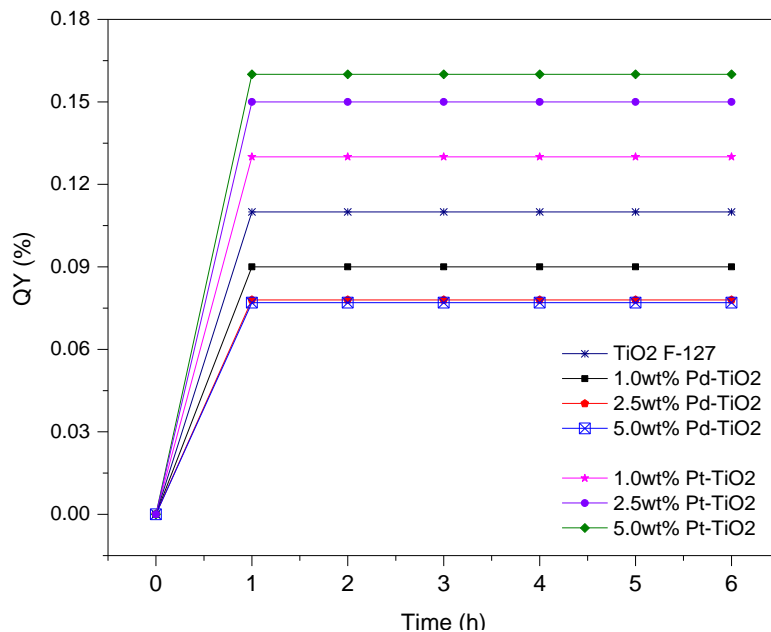


Figure 52 QY% at various irradiation times using a 0.15g/L of photocatalyst concentration under Visible Light only. Note: Photocatalyst involved Pt and Pd on TiO₂ at Different metal loadings (1.0, 2.5 and 5.0wt%). All reported data are average values of 3 repeats. Standard deviation on repeats: 3.0%

It is also interesting to see that in Figure 53, the photo-reduced semiconductors of the present study display good and stable QYs%, showing their significant ability to produce hydrogen.

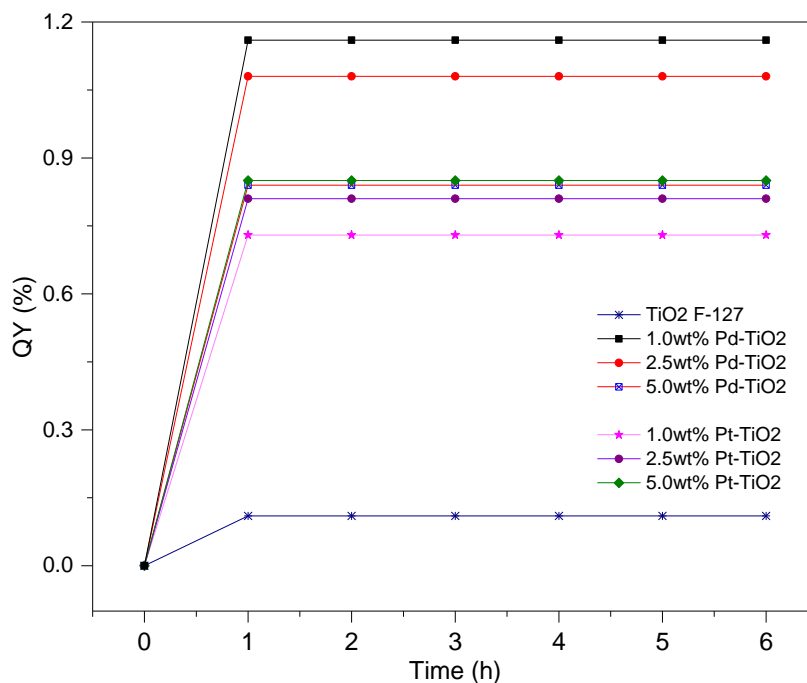


Figure 53 QY% at various irradiation times, under Visible Light, and using a 0.15g/L of photocatalyst concentration. Notes: a) Pt and Pd on TiO₂, studied with different noble metal loadings (1.0, 2.5 and 5.0wt%) and b) Photocatalysts were photoreduced using Near-UV for 1 hour. All reported data are average values of 3 repeats. Standard deviation on repeats: 2.4%

Based on the reported results is thus anticipated, that further research with mesoporous TiO₂ photocatalysts doped with noble metals will be valuable particularly on Pd-doped TiO₂ using ethanol as a scavenger. This will likely lead to stable and efficient photocatalytic processes for hydrogen production via water splitting. These Pd-TiO₂ photocatalysts may also present significant cost advantages versus other noble metal dopants such as Ta, Nb or even Pt.

7.2 Conclusions

From the various QY% values reported in this chapter the following can be concluded:

- a) The QY% determines the energy usage efficiency when using a Photo-CREC Water Reactor II for hydrogen production.
- b) The calculated QYs% at different metals loadings (1.0, 2.5 and 5.0wt%) on TiO₂ were in the 10-11% range when using 1.0wt% Pd-TiO₂ and 5.0wt% Pt-TiO₂ under near-UV Light.
- c) The determined QYs% for various doped photocatalysts at different concentrations in the water slurry, gave a maximum QY% value of 30.8% for 1.0 g/L of Pd-TiO₂.
- d) The QY% for noble metal doped-TiO₂ displayed very low efficiencies in the 0.07-0.16% range while being irradiated with visible light. This proved the very modest ability of these noble metal doped TiO₂ photocatalysts to produce hydrogen under these conditions.
- e) The QY% for the Near-UV photo-reduced Pt-TiO₂ and Pd-TiO₂ photocatalysts, increased significantly up to 0.7-1.2% under visible light. These positive findings have favourable prospects for further developments in hydrogen production, using a photoreduced Pd-TiO₂ photocatalyst under visible light.

Chapter 8

8 Conclusions and recommendations

Photocatalytic water splitting is an environmentally friendly and promising technology with significant potential for hydrogen production. This technology requires suitable photocatalysts along with solar irradiation for highly efficient hydrogen production. Manufactured hydrogen can be considered as an energy vector that can be stored and used to produce thermal energy and electricity with near-zero carbon emissions.

This MEdSc thesis addresses some of the challenges in photocatalytic water splitting to enhance the efficiency of hydrogen production for energy such as: a) limiting electron-hole pair recombination, b) reducing the semiconductor band gaps, c) activating the prepared semiconductors using near-UV and visible light.

To accomplish this, a noble metal doped titanium oxide photocatalyst was synthesized and evaluated in the Photo-CREC Water Reactor-II to produce hydrogen under both near-UV and visible light using ethanol as organic scavenger.

8.1 Conclusions

The main findings and conclusions of this MEdSc thesis can be summarized as follows:

- A TiO₂ mesoporous photocatalyst material was prepared using the sol-gel methodology and two soft templates: Pluronic P-123 and Pluronic F-127. It was found that the mesoporous TiO₂ prepared using a F-127 template displayed a better performance.
- XRD, BET, H₂-chemisorption and UV-Vis spectra were used to establish the specific surface areas, crystalline phases and band gaps of the noble metal doped TiO₂ photocatalysts.

- Macroscopic Irradiation Energy Balances were successfully employed to establish photon absorption rates and radiation absorption efficiencies. For the Pt-TiO₂ and the Pd-TiO₂ semiconductors, photon absorption efficiencies in the 60 and 64%, range under near-UV, and in the 53 and 58% range under visible light, were determined.
- Photocatalytic hydrogen production with ethanol as scavenger under an inert atmosphere, displayed an “in series-parallel” reaction network, with the formation of ethane, methane, CO₂ and acetaldehyde. The formation of hydrogen followed a steady zero-order kinetics with no apparent photoactivity decay, a small CO₂ increase and a negligible decrease of ethanol.
- Photocatalytic hydrogen production with ethanol as a scavenger and under a CO₂ atmosphere showed that in this case, hydrogen also follows a zero-order kinetics with no apparent photoactivity decay. This also led to a small CO₂ consumption and a minor increase of ethanol.
- Prepared Pt-TiO₂ and Pd-TiO₂ photocatalysts proved being adequate for hydrogen production under near-UV with the 1.0wt%-Pd on TiO₂ showing a best QY% of 30.8%.
- Near UV photo-reduced Pt-TiO₂ and Pd-TiO₂ displayed significant hydrogen production rates under visible irradiation. The best QY% for the 1.0wt%-Pd on TiO₂ were 1.16%.

8.2 Future work

Based on the valuable results of this research, several activities are proposed to be considered in the near future:

- To develop radiation models accounting for: a) irradiation absorption, b) forward and backward scattering for different Pt/Pd loadings on TiO₂. These models could

include suitable reaction kinetics and be valuable to consider various photocatalyst loadings in the slurry, and reactor scales.

- To evaluate the Pd-TiO₂ photocatalyst at noble metal loadings lower than 1.0%, where this material showed best performance.
- To establish the Pd-TiO₂ photocatalyst performance at semiconductor slurry concentrations larger than 0.15g/L. The purpose of this would be to further enhance hydrogen production and QY% efficiencies.
- To carry out a detailed analysis of the reaction kinetics of the water splitting process under CO₂ atmospheres.
- To develop accurate H₂O₂ measurements and this to better understand the role of OH• and H• radicals, while developing photocatalysis using ethanol as a scavenger.

Bibliography

- [1] United Nations Development Programme, *World energy assessment: energy and the challenge of sustainability*. 2003.
- [2] T. Chang, H.-P. Chu, and W.-Y. Chen, “Energy consumption and economic growth in 12 Asian countries: panel data analysis,” *Appl. Econ. Lett.*, vol. 20, no. 3, pp. 282–287, 2013.
- [3] “World Overview-Renewable Energy,” *IRENA International Renewable Energy Agency*, 2018. [Online]. Available: <http://www.irena.org/publications/2018/Mar/Renewable-Capacity-Statistics-2018>. [Accessed: 02-Aug-2018].
- [4] “Renewable energy facts,” *Government of Canada*, 2018. [Online]. Available: <https://www.nrcan.gc.ca/energy/facts/renewable-energy/20069>. [Accessed: 31-Jul-2018].
- [5] J. Mohtasham, “Review Article-Renewable Energies,” *Energy Procedia*, vol. 74, pp. 1289–1297, 2015.
- [6] Z. Huang, Hailun, Yan, “Renewable & Sustainable Energy Reviews,” 2009.
- [7] S. R. Bull, “Renewable Energy Today and Tomorrow.”
- [8] M. A. Delucchi and M. Z. Jacobson, “Providing all global energy with wind, water, and solar power, Part II: Reliability, system and transmission costs, and policies,” *Energy Policy*, vol. 39, no. 3, pp. 1170–1190, 2011.
- [9] C. Monteiro *et al.*, “Wind power forecasting : state-of-the-art 2009.,” 2009.
- [10] M. Z. Jacobson and M. A. Delucchi, “Providing all global energy with wind, water, and solar power, Part I: Technologies, energy resources, quantities and areas of infrastructure, and materials,” *Energy Policy*, vol. 39, no. 3, pp. 1154–1169, 2011.
- [11] M. Hoogwijk, A. Faaij, R. Van Den Broek, G. Berndes, D. Gielen, and W. Turkenburg, “Exploration of the ranges of the global potential of biomass for energy,” *Biomass and Bioenergy*, vol. 25, no. 2, pp. 119–133, 2003.
- [12] S. H. Jensen, P. H. Larsen, and M. Mogensen, “Hydrogen and synthetic fuel production from renewable energy sources,” *Int. J. Hydrogen Energy*, vol. 32, no. 15 SPEC. ISS., pp. 3253–3257, 2007.
- [13] K. Mazloomi and C. Gomes, “Hydrogen as an energy carrier: Prospects and challenges,” *Renew. Sustain. Energy Rev.*, vol. 16, no. 5, pp. 3024–3033, 2012.
- [14] D. Ipsakis, S. Voutetakis, P. Seferlis, F. Stergiopoulos, and C. Elmasides, “Power management strategies for a stand-alone power system using renewable energy sources and hydrogen storage,” *Int. J. Hydrogen Energy*, vol. 34, no. 16, pp. 7081–7095, 2009.
- [15] M. Momirlan and T. N. Veziroglu, “The properties of hydrogen as fuel tomorrow in sustainable energy system for a cleaner planet,” *Int. J. Hydrogen Energy*, vol.

- 30, no. 7, pp. 795–802, 2005.
- [16] J. Bockris, *Comments on: Hydrogen futures: toward a sustainable energy system*, vol. 28. 2003.
- [17] M. M. Rashid, M. K. Al Mesfer, H. Naseem, and M. Danish, “Hydrogen Production by Water Electrolysis: A Review of Alkaline Water Electrolysis, PEM Water Electrolysis and High Temperature Water Electrolysis,” *Int. J. Eng. Adv. Technol.*, no. 3, pp. 2249–8958, 2015.
- [18] X. Chen, S. Shen, L. Guo, and S. S. Mao, “Semiconductor-based photocatalytic hydrogen generation,” *Chem. Rev.*, vol. 110, no. 11, pp. 6503–70, 2010.
- [19] C. Acar, “Review of photocatalytic water-splitting methods for sustainable hydrogen production,” *Energy Res.*, vol. 40, pp. 1449–1473, 2016.
- [20] S. K. Cushing *et al.*, “Photocatalytic activity enhanced by plasmonic resonant energy transfer from metal to semiconductor,” *J. Am. Chem. Soc.*, vol. 134, no. 36, pp. 15033–15041, 2012.
- [21] C. Change, “G w a p h c d i a,” vol. 11, no. 2, pp. 44–58, 2007.
- [22] S. Ramesohl and F. Merten, “Energy system aspects of hydrogen as an alternative fuel in transport,” *Energy Policy*, vol. 34, no. 11, pp. 1251–1259, 2006.
- [23] L. Barreto, A. Makihira, and K. Riahi, “The hydrogen economy in the 21st century: A sustainable development scenario,” *Int. J. Hydrogen Energy*, vol. 28, no. 3, pp. 267–284, 2003.
- [24] K. Maeda *et al.*, “Photocatalyst releasing hydrogen from water,” *Nature*, vol. 440, no. 7082, p. 295, 2006.
- [25] I. Dincer, “Green methods for hydrogen production,” *Int. J. Hydrogen Energy*, vol. 37, no. 2, pp. 1954–1971, 2012.
- [26] I. Dincer, “Sustainable hydrogen production options and the role of IAHE,” *Int. J. Hydrogen Energy*, vol. 37, no. 21, pp. 16266–16286, 2012.
- [27] O. M. Yardimci, “Employing plasma as catalyst in hydrogen production,” *Int. J. Hydrogen Energy*, vol. 23, no. 12, pp. 1109–1111, 1998.
- [28] A. . Adesina, “Thermolysis of hydrogen sulphide in an open tubular reacto,” *Int. J. Hydrogen Energy*, vol. 20, no. 10, pp. 777–783, 1995.
- [29] E. Kao, “Electropolymerized polythiophene photoelectrodes for photocatalytic water splitting and hydrogen production,” *Sensors Actuators A Phys.*, vol. 277, no. 1, pp. 18–25, 2018.
- [30] J. Wang, “Fermentative hydrogen production using various biomass-based materials as feedstock,” *Renew. Sustain. Energy Rev.*, vol. 92, pp. 284–306, 2018.
- [31] P. Parthasarathy, “Hydrogen production from steam gasification of biomass: Influence of process parameters on hydrogen yield – A review,” *Renew. Energy*, vol. 66, pp. 570–579, 2014.
- [32] J. Kennedy, “Hydrogen generation by photocatalytic reforming of potential

- biofuels: Polyols, cyclic alcohols, and saccharides,” *J. Photochem. Photobiol. A Chem.*, vol. 356, no. 1, pp. 451–456, 2018.
- [33] H. Tebibel, “Comparative performance analysis of a grid connected PV system for hydrogen production using PEM water, methanol and hybrid sulfur electrolysis,” *Int. J. Hydrogen Energy*, vol. 43, no. 6, pp. 3482–3498, 2018.
- [34] P. Nikolaidis and A. Poullikkas, “A comparative overview of hydrogen production processes,” *Renew. Sustain. Energy Rev.*, vol. 67, pp. 597–611, 2017.
- [35] M. Ni, M. K. H. Leung, K. Sumathy, and D. Y. C. Leung, “Potential of renewable hydrogen production for energy supply in Hong Kong,” *Int. J. Hydrogen Energy*, vol. 31, no. 10, pp. 1401–1412, 2006.
- [36] F. Khalid, “Model development and analysis of a novel high-temperature electrolyser for gas phase electrolysis of hydrogen chloride for hydrogen production,” *Int. J. Hydrogen Energy*, vol. 43, no. 19, pp. 9112–9118, 2018.
- [37] H. Ozcan, “Performance investigation of magnesium–chloride hybrid thermochemical cycle for hydrogen production,” *Int. J. Hydrogen Energy*, vol. 39, no. 1, pp. 76–85, 2018.
- [38] V. Kyriakou, “A protonic ceramic membrane reactor for the production of hydrogen from coal steam gasification,” *J. Memb. Sci.*, vol. 553, no. 1, pp. 163–170, 2018.
- [39] N. Muradov, “Low to near-zero CO₂ production of hydrogen from fossil fuels: Status and perspectives,” *Int. J. Hydrogen Energy*, vol. 42, no. 20, pp. 14058–14088, 2018.
- [40] D. Sengmee, “Biophotolysis-based hydrogen and lipid production by oleaginous microalgae using crude glycerol as exogenous carbon source,” *Int. J. Hydrogen Energy*, vol. 42, no. 4, pp. 1970–1976, 2017.
- [41] R. García-Sánchez, “Photofermentation of tequila vinasses by *Rhodospseudomonas pseudopalustris* to produce hydrogen,” *Int. J. Hydrogen Energy*, 2018.
- [42] S. Fukuzumi, “Artificial photosynthesis for production of hydrogen peroxide and its fuel cells,” *Biochim. Biophys. Acta - Bioenerg.*, vol. 1857, no. 5, pp. 604–611, 2016.
- [43] I. Dincer, “Photonic Energy Production,” in *Comprehensive Energy Systems*, 2018, pp. 707–754.
- [44] A. V Puga, “Photocatalytic production of hydrogen from biomass-derived feedstocks,” *Coord. Chem. Rev.*, vol. 315, pp. 1–65, 2016.
- [45] C. a Linkous *et al.*, “Solar Photocatalytic Hydrogen Production From Water Using a Dual Bed Photosystem,” *Chem. Commun.*, vol. 47, no. 33, 2011.
- [46] C. Byrne, “Recent advances in photocatalysis for environmental applications,” *J. Environ. Chem. Eng.*, vol. 6, no. 3, pp. 3531–3555, 2018.
- [47] H. Wang, “Recent progress in ultrathin two-dimensional semiconductors for photocatalysis,” *Mater. Sci. Eng. R Reports*, vol. 130, pp. 1–39, 2018.

- [48] M. Imase, "Estimating the viability of *Chlorella* exposed to oxidative stresses based around photocatalysis," *Int. Biodeterior. Biodegradation*, vol. 78, pp. 1–6, 2013.
- [49] J. . Moulijin, *Catalysis. An integrated approach to homogeneous, heterogenous and industrial catalysis*. Amsterdam, The Netherlands: Elsevier, 1993.
- [50] Y. L. Can Li, *Bridging Heterogeneous and Homogeneous Catalysis: Concepts, Strategies, and applications*. 2014.
- [51] N. Ahmed, "Heterogeneous photocatalysis and its potential applications in water and wastewater treatment: a review," *Nanotechnology*, vol. 29, no. 34, 2018.
- [52] R. de Fátima, "Mass transfer and photocatalytic degradation of leather dye using TiO₂/UV," *J. Appl. Electrochem.*, vol. 35, no. 7–8, pp. 821–829, 2005.
- [53] K. Takanabe, "Photocatalytic Water Splitting: Quantitative Approaches toward Photocatalyst by Design," *ACS Catal.*, vol. 7, no. 11, pp. 8006–8022, 2017.
- [54] T. Li Hsiung, "Chemical structure of photocatalytic active sites in nanosize TiO₂," *J. Phys. Chem. Solids*, vol. 69, no. 2–3, pp. 383–385, 2018.
- [55] W.-N. Zhao, "Mechanism and active site of photocatalytic water splitting on titania in aqueous surroundings," *Chem. Sci.*, no. 6, 2014.
- [56] S. Zhu, "Photocatalysis: Basic Principles, Diverse Forms of Implementations and Emerging Scientific Opportunities," *Advanve Energy Mater.*, vol. 7, no. 23, 2017.
- [57] S. Somiya, *Handbook of Advanced Ceramics*, 2nd ed. Academic Press Inc, 2013.
- [58] A. Currao, "Photoelectrochemical Water Splitting," *Chim. Int. J. Chem.*, vol. 61, no. 12, pp. 815–819, 2007.
- [59] M. G. Walter *et al.*, "Solar water splitting cells," *Chem. Rev.*, vol. 110, no. 11, pp. 6446–6473, 2010.
- [60] H. Ahmad, S. K. Kamarudin, L. J. Minggu, and M. Kassim, "Hydrogen from photo-catalytic water splitting process: A review," *Renew. Sustain. Energy Rev.*, vol. 43, pp. 599–610, 2015.
- [61] A. Galińska, "Photocatalytic Water Splitting over Pt–TiO₂ in the Presence of Sacrificial Reagents," *Energy & Fuels*, vol. 19, no. 3, pp. 1143–1147, 2005.
- [62] A. Mills, "An overview of semiconductor photocatalysis," *J. Photochem. Photobiol. A Chem.*, vol. 108, no. 1, pp. 1–35, 1997.
- [63] R. Abe, "Significant effect of iodide addition on water splitting into H₂ and O₂ over Pt-loaded TiO₂ photocatalyst: suppression of backward reaction," *Chem. Phys. Lett.*, vol. 371, no. 3–4, pp. 360–364, 2003.
- [64] A. Mills, "Photosensitised dissociation of water using dispersed suspensions of n-type semiconductors," *J. Chem. Soc. Faraday Trans. 1 Phys. Chem. Condens. Phases*, vol. 12, no. 78, pp. 3659–3669, 1982.
- [65] M. M. Khan, S. F. Adil, and A. Al-Mayouf, "Metal oxides as photocatalysts," *J. Saudi Chem. Soc.*, vol. 19, no. 5, pp. 462–464, 2015.

- [66] P. Holloway and G. McGuire, *Handbook of Compound Semiconductor*. New Jersey, USA: Noyes Publications, 1995.
- [67] L. Forni, "Mass and heat transfer in catalytic reactions," *Catal. Today*, vol. 52, no. 2–3, pp. 147–152, 1999.
- [68] B. D. Zdravkov, J. J. Čermák, M. Šefara, and J. Janků, "Pore classification in the characterization of porous materials: A perspective," *Cent. Eur. J. Chem.*, vol. 5, no. 2, pp. 385–395, 2007.
- [69] S. Cho, J. W. Jang, K. H. Lee, and J. S. Lee, "Research update: Strategies for efficient photoelectrochemical water splitting using metal oxide photoanodes," *APL Mater.*, vol. 2, no. 1, 2014.
- [70] R. H. Gonçalves, B. H. R. Lima, and E. R. Leite, "Magnetite colloidal nanocrystals: A facile pathway to prepare mesoporous hematite thin films for photoelectrochemical water splitting," *J. Am. Chem. Soc.*, vol. 133, no. 15, pp. 6012–6019, 2011.
- [71] G. Wang, Y. Ling, and Y. Li, "Oxygen-deficient metal oxide nanostructures for photoelectrochemical water oxidation and other applications," *Nanoscale*, vol. 4, no. 21, pp. 6682–6691, 2012.
- [72] Y. Li, "Hydrogen generation from photoelectrochemical water splitting based on nanomaterials," *Laser Photonics Rev.*, vol. 4, no. 4, pp. 517–528, 2010.
- [73] M. . Cauqui, "Application of the sol-gel methods to catalyst preparation," *J. Non. Cryst. Solids*, vol. 147, pp. 724–738, 1992.
- [74] J. Brinker and G. W. Schere, *Sol-Gel Science: The Physics and Chemistry of Sol-Gel Processing*. San Diego, California: Academic Press Inc, 1990.
- [75] D. A. Ward, "Preparing Catalytic Materials by the Sol-Gel Method," *I&EC Res.*, vol. 34, no. 2, pp. 421–433, 1995.
- [76] S. Thiagarajan, A. Sanmugam, and D. Vikraman, "Facile Methodology of Sol-Gel Synthesis for Metal Oxide Nanostructures," *Recent Appl. Sol-Gel Synth.*, pp. 1–16, 2017.
- [77] D. Levy, *Part One Sol – Gel Chemistry and Methods*. 2015.
- [78] A. J. Haider, "Exploring potential Environmental applications of TiO₂ Nanoparticles," *Energy Procedia*, vol. 119, pp. 332–345, 2017.
- [79] S. Y. Lee and S. J. Park, "TiO₂ photocatalyst for water treatment applications," *J. Ind. Eng. Chem.*, vol. 19, no. 6, pp. 1761–1769, 2013.
- [80] A. L. Castro, "Synthesis of anatase TiO₂ nanoparticles with high temperature stability and photocatalytic activity," *Solid State Sci.*, vol. 10, no. 5, pp. 602–606, 2008.
- [81] P. C. Ricci *et al.*, "Anatase-to-rutile phase transition in TiO₂ nanoparticles irradiated by visible light," *J. Phys. Chem. C*, vol. 117, no. 15, pp. 7850–7857, 2013.
- [82] W. L. Chin, F. Wah Low, S. Weng Chong, and S. Bee Abd Hamid, "An Overview:

- Recent Development of Titanium Dioxide Loaded Graphene Nanocomposite Film for Solar Application,” *Curr. Org. Chem.*, vol. 19, 2015.
- [83] Y. Zhang, J. Liu, G. Wu, and W. Chen, “Porous graphitic carbon nitride synthesized via direct polymerization of urea for efficient sunlight-driven photocatalytic hydrogen production,” *Nanoscale*, vol. 4, no. 17, pp. 5300–5303, 2012.
- [84] G. Hasegawa, *Studies on Porous Monolithic Materials Prepared via Sol–Gel Processes*. Japan: Springer Science, 2013.
- [85] B. Guo, H. Shen, K. Shu, Y. Zeng, and W. Ning, “The study of the relationship between pore structure and photocatalysis of mesoporous TiO₂,” *J. Chem. Sci.*, vol. 121, no. 3, pp. 317–321, 2009.
- [86] X. He, *Recent Progress in Fabrication of Nanostructured Carbon Monolithic Materials*. 2017.
- [87] C.-H. Liao, C.-W. Huang, and J. C. S. Wu, “Hydrogen Production from Semiconductor-based Photocatalysis via Water Splitting,” *Catalysts*, vol. 2, no. 4, pp. 490–516, 2012.
- [88] D. Jing *et al.*, “Efficient solar hydrogen production by photocatalytic water splitting: From fundamental study to pilot demonstration,” *Int. J. Hydrogen Energy*, vol. 35, no. 13, pp. 7087–7097, 2010.
- [89] J. Schneider, “Understanding TiO₂ Photocatalysis: Mechanisms and Materials,” *Chem. Rev.*, vol. 114, no. 19, pp. 9919–9986, 2014.
- [90] K. Nakata and A. Fujishima, “TiO₂ photocatalysis: Design and applications,” *J. Photochem. Photobiol. C Photochem. Rev.*, vol. 13, no. 3, pp. 169–189, 2012.
- [91] J. Yang, “Roles of Cocatalysts in Photocatalysis and Photoelectrocatalysis,” *Acc. Chem. Res.*, vol. 46, no. 8, pp. 1900–1909, 2013.
- [92] P. V. Kamat, “Manipulation of charge transfer across semiconductor interface. A criterion that cannot be ignored in photocatalyst design,” *J. Phys. Chem. Lett.*, vol. 3, no. 5, pp. 663–672, 2012.
- [93] P. D. Vaidya and A. E. Rodrigues, “Glycerol reforming for hydrogen production: A review,” *Chem. Eng. Technol.*, vol. 32, no. 10, pp. 1463–1469, 2009.
- [94] V. Etacheri, C. Di Valentin, J. Schneider, D. Bahnemann, and S. C. Pillai, “Visible-light activation of TiO₂ photocatalysts: Advances in theory and experiments,” *J. Photochem. Photobiol. C Photochem. Rev.*, vol. 25, pp. 1–29, 2015.
- [95] B. J. Clark, *UV Spectroscopy: Techniques, instrumentation and data handling*. London, England, 1993.
- [96] V.-H. Nguyen, “Recent developments in the design of photoreactors for solar energy conversion from water splitting and CO₂ reduction,” *Appl. Catal. A Gen.*, vol. 550, pp. 122–141, 2018.
- [97] T. Jafari, E. Moharrerri, A. S. Amin, R. Miao, W. Song, and S. L. Suib,

- “Photocatalytic water splitting - The untamed dream: A review of recent advances,” *Molecules*, vol. 21, no. 7, 2016.
- [98] A. K. Seferlis and S. G. Neophytides, “On the kinetics of photoelectrocatalytic water splitting on nanocrystalline TiO₂ films,” *Appl. Catal. B Environ.*, vol. 132–133, pp. 543–552, 2013.
- [99] M. Wang, S. Shen, L. Li, Z. Tang, and J. Yang, “Effects of sacrificial reagents on photocatalytic hydrogen evolution over different photocatalysts,” *J. Mater. Sci.*, vol. 52, no. 9, pp. 5155–5164, 2017.
- [100] C. R. López, E. P. Melián, J. A. Ortega Méndez, D. E. Santiago, J. M. Doña Rodríguez, and O. González Díaz, “Comparative study of alcohols as sacrificial agents in H₂ production by heterogeneous photocatalysis using Pt/TiO₂ catalysts,” *J. Photochem. Photobiol. A Chem.*, vol. 312, pp. 45–54, 2015.
- [101] K. C. Christoforidis and P. Fornasiero, “Photocatalytic Hydrogen Production: A Rift into the Future Energy Supply,” *ChemCatChem*, vol. 9, no. 9, pp. 1523–1544, 2017.
- [102] S. E. Salas and S. Hugo De Lasa, “Photocatalytic Water Splitting using a Modified Pt- TiO₂. Kinetic Modeling and Hydrogen Production Efficiency,” August, 2013.
- [103] S. Escobedo and H. De Lasa, “Photocatalytic Water Splitting using a Modified Pt-TiO₂. Kinetic Modeling and Hydrogen Production Efficiency,” The University of Western Ontario, 2013.
- [104] H. De Lasa, B. S. Rosales, J. Moreira, and P. Valades-Pelayo, “Efficiency Factors in Photocatalytic Reactors: Quantum Yield and Photochemical Thermodynamic Efficiency Factor,” *Chem. Eng. Technol.*, vol. 39, no. 1, pp. 51–65, 2016.
- [105] S. E. Braslavsky, “Glossary of terms used in photochemistry, 3rd edition (IUPAC Recommendations 2006),” *Pure Appl. Chem.*, vol. 79, no. 3, pp. 293–465, 2007.
- [106] A. E. Cassano, C. A. Martin, R. J. Brandi, and O. M. Alfano, “Photoreactor Analysis and Design: Fundamentals and Applications,” *Ind. Eng. Chem. Res.*, vol. 34, no. 7, pp. 2155–2201, 1995.
- [107] M. R. Hoffmann, S. T. Martin, W. Choi, and D. W. Bahnemann, “Environmental Applications of Semiconductor Photocatalysis,” *Chem. Rev.*, vol. 95, no. 1, pp. 69–96, 1995.
- [108] J. F. Guayaquil-Sosa, B. Serrano-Rosales, P. J. Valadés-Pelayo, and H. de Lasa, “Photocatalytic hydrogen production using mesoporous TiO₂ doped with Pt,” *Appl. Catal. B Environ.*, vol. 211, pp. 337–348, 2017.
- [109] H. de Lasa, B. Serrano, and M. Salaiques, *Photocatalytic Reaction Engineering*. USA: Springer Science, 2005.
- [110] B. S. Rosales, J. Moreira Del Rio, J. F. Guayaquil, and H. De Lasa, “Photodegradation Efficiencies in a Photo-CREC Water-II Reactor Using Several TiO₂Based Catalysts,” *Int. J. Chem. React. Eng.*, vol. 14, no. 3, pp. 685–701, 2016.

- [111] Y.-L. He, S.-Z. Qin, C. J. Lim, and J. R. Grace, "Particle velocity profiles and solid flow patterns in spouted beds," *Can. J. Chem. Eng.*, vol. 72, no. 4, pp. 561–568, 1994.
- [112] S. M. Systems, M. Fiber, O. Spectrometers, L. Sources, F. O. Cables, and S. Accessories, "eXtreme Spectrometer Instrumentation S tellar N et C atalog," *Spectroscopy*, 1931.
- [113] S. Coated and L. O. W. Pressure, "Uv-b, bl & blb."
- [114] B. Serrano, A. Ortíz, J. Moreira, and H. I. De Lasa, "Energy efficiency in photocatalytic reactors for the full span of reaction times," *Ind. Eng. Chem. Res.*, vol. 48, no. 22, pp. 9864–9876, 2009.
- [115] M. J. Garcia, "Photocatalytic Reactors for Air Treatment : Energy Efficiencies and Kinetic Modeling," no. April, p. 147, 2012.
- [116] H. De Lasa, B. Serrano, and M. Salaices, *Photocatalytic Reaction Engineering*. London, Ontario, 2004.
- [117] S. P. Guo, J. C. Li, Q. T. Xu, Z. Ma, and H. G. Xue, "Recent achievements on polyanion-type compounds for sodium-ion batteries: Syntheses, crystal chemistry and electrochemical performance," *J. Power Sources*, vol. 361, pp. 285–299, 2017.
- [118] D. Ficai and A. Mihai Grumezescu, *Nanostructures for Novel Therapy*. Bucharest, Romania: Elsevier Inc, 2017.
- [119] H. Luo, C. Wang, and Y. Yan, "Synthesis of mesostructured titania with controlled crystalline framework," *Chem. Mater.*, vol. 15, no. 20, pp. 3841–3846, 2003.
- [120] D. V. Aware and S. S. Jadhav, "Synthesis, characterization and photocatalytic applications of Zn-doped TiO₂ nanoparticles by sol–gel method," *Appl. Nanosci.*, vol. 6, no. 7, pp. 965–972, 2016.
- [121] D. Y. Zhao, P. D. Yang, N. Melosh, J. L. Feng, B. F. Chmelka, and G. D. Stucky, "Continuous mesoporous silica films with highly ordered large pore structures," *Adv. Mater.*, vol. 10, no. 16, pp. 1380–1385, 1998.
- [122] T. Křížek, P. Coufal, E. Tesařová, J. Sobotníková, and Z. Bosáková, "Pluronic F-127 as the buffer additive in capillary entangled polymer electrophoresis: Some fundamental aspects," *J. Sep. Sci.*, vol. 33, no. 16, pp. 2458–2464, 2010.
- [123] E. M. Samsudin, S. B. A. Hamid, J. C. Juan, and W. J. Basirun, "Influence of triblock copolymer (pluronic F127) on enhancing the physico-chemical properties and photocatalytic response of mesoporous TiO₂," *Appl. Surf. Sci.*, vol. 355, pp. 959–968, 2015.
- [124] E. H. D. Donkers, *Block copolymers with polar and non-polar blocks : combination of living anionic polymerization and RAFT- mediated polymerization*. 2018.
- [125] T. Wang, D. Chen, J. Ma, S. Wen, and Q. Liu, "Synthesis and characterisation of pore-expanded mesoporous silica materials," *Micro & Nano Lett.*, vol. 10, no. 2, pp. 140–144, 2015.

- [126] J. Wang, H. Li, H. Li, C. Zou, H. Wang, and D. Li, "Mesoporous TiO₂ thin films exhibiting enhanced thermal stability and controllable pore size: Preparation and photocatalyzed destruction of Cationic Dyes," *ACS Appl. Mater. Interfaces*, vol. 6, no. 3, pp. 1623–1631, 2014.
- [127] J. Wang, J. Wu, and L. Hongyi, "A Review of Mesoporous TiO₂ Thin Films," *Key Lab Adv. Funct. Mater. Sch. Mater. Sci. Eng. Beijing Univ. Technol. Beijing 100124, China*.
- [128] J. C. Yu, X. Wang, and X. Fu, "Pore-Wall Chemistry and Photocatalytic Activity of Mesoporous Titania Molecular Sieve Films," *Chem. Mater.*, vol. 16, no. 8, pp. 1523–1530, 2004.
- [129] E. Gioffredia *et al.*, "Pluronic F127 hydrogel characterization and biofabrication in cellularized constructs for tissue engineering applications," *Elsevier B.V.*, 2015.
- [130] R. Ivanova, B. Lindman, and P. Alexandridis, "Evolution in structural polymorphism of Pluronic F127 poly(ethylene oxide)-poly(propylene oxide) block copolymer in ternary systems with water and pharmaceutically acceptable organic solvents: From 'glycols' to 'oils'," *Langmuir*, vol. 16, no. 23, pp. 9058–9069, 2000.
- [131] H. Oveisi, N. Suzuki, A. Beitollahi, and Y. Yamauchi, "Aerosol-assisted fabrication of mesoporous titania spheres with crystallized anatase structures and investigation of their photocatalytic properties," *J. Sol-Gel Sci. Technol.*, vol. 56, no. 2, pp. 212–218, 2010.
- [132] "Sigma Aldrich," 2018. [Online]. Available: <https://www.sigmaaldrich.com/catalog/product/aldrich/435465?lang=en®ion=CA>. [Accessed: 30-May-2018].
- [133] Z. He and P. Alexandridis, "Micellization thermodynamics of Pluronic P123 (EO₂₀PO₇₀EO₂₀) amphiphilic block copolymer in aqueous Ethylammonium nitrate (EAN) solutions," *Polymers (Basel)*, vol. 10, no. 1, 2017.
- [134] M. Zhu *et al.*, "Preparation of PA6/nano titanium dioxide (TiO₂) composites and their spinnability," *Macromol. Symp.*, vol. 210, pp. 251–261, 2004.
- [135] Z. Xiao and D. Ma, "Probing the Use of Small-Angle Light Scattering," *Wiley Intersci.*, 2005.
- [136] M. Yoshida, M. Lal, N. Kumar, and P. Prasad, "TiO₂ nano-particle-dispersed polyimide composite optical waveguide materials through reverse micelles," *J. Mater. Sci.*, vol. 2, pp. 4047–4051, 1997.
- [137] R. J. Nussbaumer, W. R. Caseri, P. Smith, and T. Tervoort, "Polymer-TiO₂ nanocomposites: A route towards visually transparent broadband UV filters and high refractive index materials," *Macromol. Mater. Eng.*, vol. 288, no. 1, pp. 44–49, 2003.
- [138] K. J. Rao, *Structural Chemistry of Glasses*. Elsevier Science, 2002.
- [139] J. F. Guayaquil-sosa, "Photocatalytic Hydrogen Production using a Mesoporous TiO₂ Doped with Pt : Semiconductor Synthesis , Oxidation-Reduction Network

and Quantum Efficiencies .,” no. February, 2018.

- [140] M. Cargnello, T. R. Gordon, and C. B. Murray, “Solution-phase synthesis of titanium dioxide nanoparticles and nanocrystals,” *Chem. Rev.*, vol. 114, no. 19, pp. 9319–9345, 2014.
- [141] G. Fagerlund, “Determination of specific surface by the BET method,” *Matériaux Constr.*, vol. 6, no. 3, pp. 239–245, 1973.
- [142] Micromeritics Instrument Corporation, “Gas Adsorption Theory,” http://www.micromeritics.com/Repository/Files/Gas_Adsorption_Theory_poster.pdf, p. 1, 1AD.
- [143] Micromeritics, *ASAP 2020 Operator’s Manual*, October. 2006.
- [144] A. T. Hubbard, *Encyclopedia of Surface and Colloid Scienc*, Volume 1. New York, USA: Marcel Dekker, Inc, 2002.
- [145] X. Pan and Y. J. Xu, “Defect-mediated growth of noble-metal (Ag, Pt, and Pd) nanoparticles on TiO₂ with oxygen vacancies for photocatalytic redox reactions under visible light,” *J. Phys. Chem. C*, vol. 117, no. 35, pp. 17996–18005, 2013.
- [146] *AutoChem 2920 Automated Catalyst Characterization System Operator’s Manual*, no. July. 2014.
- [147] W. F. Bleam, *Soil and Environmental Chemistry*. Elsevier, 2012.
- [148] S. Kuhaudomlap, O. Mekasuwandumrong, P. Prasertthdam, S.-I. Fujita, M. Arai, and J. Panpranot, “The H₂-Treated TiO₂ Supported Pt Catalysts Prepared by Strong Electrostatic Adsorption for Liquid-Phase Selective Hydrogenation,” *Catalysts*, vol. 8, no. 2, p. 87, 2018.
- [149] R. Geyer, J. Hunold, M. Keck, P. Kraak, A. Pachulski, and R. Schödel, “Methods for determining the metal crystallite size of Ni supported catalysts,” *Chemie-Ingenieur-Technik*, vol. 84, no. 1–2, pp. 160–164, 2012.
- [150] B. E. Warren, *X-Ray Diffraction*. United States: Dover publications, 1990.
- [151] J. Zhang, P. Zhou, J. Liu, and J. Yu, “New understanding of the difference of photocatalytic activity among anatase, rutile and brookite TiO₂,” *Phys. Chem. Chem. Phys.*, vol. 16, no. 38, pp. 20382–20386, 2014.
- [152] D. Rodri´guez-Vindas, “Synthesis of palladium with different nanoscale structures by sputtering deposition onto fiber templates,” *J. Nanophotonics*, vol. 2, no. 1, p. 021925, 2008.
- [153] Na, “Ultraviolet -Visible Spectroscopy (UV),” *Rsc*, p. 68, 2014.
- [154] A. Slav, “Optical characterization of TiO₂ -Ge Nanocomposite Films Obtained by Reactive Magnetron Sputtering,” *J. Nanomater. Biostructures.*, vol. 6, no. 3, pp. 915–920, 2011.
- [155] Y. Xiong, J. Chen, B. Wiley, Y. Xia, Y. Yin, and Z. Y. Li, “Size-dependence of surface plasmon resonance and oxidation for Pd nanocubes synthesized via a seed etching process,” *Nano Lett.*, vol. 5, no. 7, pp. 1237–1242, 2005.

- [156] F. Gomes *et al.*, “Effect of Noble Metals (Ag , Pd , Pt) Loading over the Efficiency of TiO₂ during Photocatalytic Ozonation on the Toxicity of Parabens †,” pp. 1–14, 2018.
- [157] J. Moreira, B. Serrano, A. Ortiz, H. de Lasa, and H. De Lasa, “Evaluation of Photon Absorption in an Aqueous TiO₂ Slurry Reactor Using Monte Carlo Simulations and Macroscopic Balance,” *Ind. Eng. Chem. Res.*, vol. 49, no. 21, pp. 10524–10534, 2010.
- [158] P. J. Valades-Pelayo, J. Moreira, B. Serrano, and H. De Lasa, “Boundary conditions and phase functions in a photo-crec water-II reactor radiation field,” *Chem. Eng. Sci.*, vol. 107, pp. 123–136, 2014.
- [159] C. Minero and D. Vione, “A quantitative evaluation of the photocatalytic performance of TiO₂ slurries,” *Appl. Catal. B Environ.*, vol. 67, no. 3–4, pp. 257–269, 2006.
- [160] M. Salaices, B. Serrano, and H. I. De Lasa, “Experimental evaluation of photon absorption in an aqueous TiO₂ slurry reactor,” *Chem. Eng. J.*, vol. 90, no. 3, pp. 219–229, 2002.
- [161] V. Gombac *et al.*, “CuO_x-TiO₂ Photocatalysts for H₂ Production from Ethanol and Glycerol Solutions †,” *J. Phys. Chem. A*, vol. 114, no. 11, pp. 3916–3925, 2010.
- [162] M. Watanabe, “Dye-sensitized photocatalyst for effective water splitting catalyst,” *Sci. Technol. Adv. Mater.*, vol. 18, no. 1, pp. 705–723, 2017.
- [163] S. Escobedo, B. Serrano, A. Calzada, J. Moreira, and H. De Lasa, “Hydrogen production using a platinum modified TiO₂ photocatalyst and an organic scavenger. Kinetic modeling,” *Fuel*, vol. 181, pp. 438–449, 2016.
- [164] J. M. Thornton and D. Raftery, “Efficient photocatalytic hydrogen production by platinum-loaded carbon-doped cadmium indate nanoparticles,” *ACS Appl. Mater. Interfaces*, vol. 4, no. 5, pp. 2426–2431, 2012.
- [165] H. Yoshida *et al.*, “Hydrogen production from methane and water on platinum loaded titanium oxide photocatalysts,” *J. Phys. Chem. C*, vol. 112, no. 14, pp. 5542–5551, 2008.
- [166] N. Zhang, S. Liu, X. Fu, and Y. J. Xu, “Synthesis of M@TiO₂ (M = Au, Pd, Pt) core-shell nanocomposites with tunable photoreactivity,” *J. Phys. Chem. C*, vol. 115, no. 18, pp. 9136–9145, 2011.
- [167] S. Riyapan *et al.*, “Improved catalytic performance of Pd/TiO₂ in the selective hydrogenation of acetylene by using H₂-treated sol-gel TiO₂,” *J. Mol. Catal. A Chem.*, vol. 383–384, pp. 182–187, 2014.
- [168] S. Akbayrak, Y. Tonbul, and S. Özkar, “Nanoceria supported palladium(0) nanoparticles: Superb catalyst in dehydrogenation of formic acid at room temperature,” *Appl. Catal. B Environ.*, vol. 206, pp. 384–392, 2017.
- [169] V. B. Borodin, A. A. Tsygankov, K. K. Rao, and D. O. Hall, “Hydrogen production by *Anabaena variabilis* PK84 under simulated outdoor conditions,”

- Biotechnol. Bioeng.*, vol. 69, no. 5, pp. 478–485, 2000.
- [170] I. Dalmolin, E. Skovroinski, A. Biasi, M. L. Corazza, C. Dariva, and J. V. Oliveira, “Solubility of carbon dioxide in binary and ternary mixtures with ethanol and water,” *Fluid Phase Equilib.*, vol. 245, no. 2, pp. 193–200, 2006.
- [171] O. Ola, M. Maroto-Valer, D. Liu, S. MacKintosh, C. W. Lee, and J. C. S. Wu, “Performance comparison of CO₂ conversion in slurry and monolith photoreactors using Pd and Rh-TiO₂ catalyst under ultraviolet irradiation,” *Appl. Catal. B Environ.*, vol. 126, pp. 172–179, 2012.
- [172] V. P. Indrakanti, J. D. Kubicki, and H. H. Schobert, “Photoinduced activation of CO₂ on Ti-based heterogeneous catalysts: Current state, chemical physics-based insights and outlook,” *Energy Environ. Sci.*, vol. 2, no. 7, pp. 745–758, 2009.
- [173] A. Olivo, E. Ghedini, M. Signoretto, M. Compagnoni, and I. Rossetti, “Liquid vs. Gas Phase CO₂ Photoreduction Process: Which Is the Effect of the Reaction Medium?,” *Energies*, vol. 10, no. 9, p. 1394, 2017.
- [174] O. Ola and M. M. Maroto-Valer, “Review of material design and reactor engineering on TiO₂ photocatalysis for CO₂ reduction,” *J. Photochem. Photobiol. C Photochem. Rev.*, vol. 24, pp. 16–42, 2015.
- [175] T. Puangpetch, T. Sreethawong, S. Yoshikawa, and S. Chavadej, “Hydrogen production from photocatalytic water splitting over mesoporous-assembled SrTiO₃ nanocrystal-based photocatalysts,” *J. Mol. Catal. A Chem.*, vol. 312, no. 1–2, pp. 97–106, 2009.
- [176] Pankaj Chowdhury, “SOLAR AND VISIBLE LIGHT DRIVEN PHOTOCATALYSIS FOR SACRIFICIAL HYDROGEN GENERATION AND WATER DETOXIFICATION WITH CHEMICALLY MODIFIED TiO₂,” *Appl. Sol. Visible Light Driven Photocatal.*, vol. 2, no. August, 2012.
- [177] J. Peng and S. Wang, “Performance and characterization of supported metal catalysts for complete oxidation of formaldehyde at low temperatures,” *Appl. Catal. B Environ.*, vol. 73, no. 3, pp. 282–291, 2007.
- [178] J. F. Gomes *et al.*, “Photocatalytic ozonation using doped TiO₂ catalysts for the removal of parabens in water,” *Sci. Total Environ.*, vol. 609, pp. 329–340, 2017.
- [179] H. Bahruji *et al.*, “Rutile TiO₂–Pd Photocatalysts for Hydrogen Gas Production from Methanol Reforming,” *Top. Catal.*, vol. 58, no. 2–3, pp. 70–76, 2015.
- [180] H. Zhang, J. Sun, V. L. Dagle, B. Halevi, A. K. Datye, and Y. Wang, “Influence of ZnO facets on Pd/ZnO catalysts for methanol steam reforming,” *ACS Catal.*, vol. 4, no. 7, pp. 2379–2386, 2014.
- [181] W. G. Onderwaater, A. Taranovskyy, G. C. Van Baarle, J. W. M. Frenken, and I. M. N. Groot, “In Situ Optical Reflectance Difference Observations of CO Oxidation over Pd(100),” *J. Phys. Chem. C*, vol. 121, no. 21, pp. 11407–11415, 2017.
- [182] H. Ibrahim and H. De Lasa, “Novel photocatalytic reactor for the destruction of airborne pollutants reaction kinetics and quantum yields,” *Ind. Eng. Chem. Res.*,

vol. 38, no. 9, pp. 3211–3217, 1999.

- [183] J. Luan and Y. Li, “Photocatalytic Water Splitting for Hydrogen Production with Gd_2MSbO_7 ($M = Fe, In, Y$) Photocatalysts under Visible Light Irradiation,” *Materials (Basel)*, vol. 8, no. 1, pp. 16–30, 2014.
- [184] V. J. Babu, M. K. Kumar, A. S. Nair, T. L. Kheng, S. I. Allakhverdiev, and S. Ramakrishna, “Visible light photocatalytic water splitting for hydrogen production from N-TiO₂ rice grain shaped electrospun nanostructures,” *Int. J. Hydrogen Energy*, vol. 37, 10, pp. 8897–8904, 2012.
- [185] R. Niishiro, H. Kato, and A. Kudo, “Nickel and either tantalum or niobium-codoped TiO₂ and SrTiO₃ photocatalysts with visible-light response for H₂ or O₂ evolution from aqueous solutions,” *Phys. Chem. Chem. Phys.*, vol. 7, no. 10, p. 2241, 2005.
- [186] J. Ding, S. Sun, W. Yan, J. Bao, and C. Gao, “Photocatalytic H₂ evolution on a novel CaIn₂S₄ photocatalyst under visible light irradiation,” *Int. J. Hydrogen Energy*, vol. 38, no. 30, pp. 13153–13158, 2013.
- [187] O. Fontelles-Carceller, M. J. Muñoz-Batista, J. C. Conesa, M. Fernández-García, and A. Kubacka, “UV and visible hydrogen photo-production using Pt promoted Nb-doped TiO₂ photo-catalysts: Interpreting quantum efficiency,” *Appl. Catal. B Environ.*, vol. 216, pp. 133–145, 2017.

Appendices

Appendix A: E_{av} Average Photon Energy

The average photon energy is defined as the energy required by the photocatalyst to overcome the TiO₂ band gap. This calculation refers to the irradiative lamp spectra given by the near UV and visible light lamps.

As stated in Chapter 3 of the present study an average emitted photon Energy was calculated according to the following mathematical expression:

$$E_{av} = \frac{\int_{\lambda_{min}}^{\lambda_{max}} I(\lambda) E(\lambda) d\lambda}{\int_{\lambda_{min}}^{\lambda_{max}} I(\lambda) d\lambda}$$

Where, I is the intensity of the emitted photons (W/cm²), assessed as $I(\lambda) \approx q(\theta, z, \lambda, t) \Delta\lambda$ and measured with a spectrophotoradiometer. The irradiance is represented by $q(\theta, z, \lambda, t) \Delta\lambda$ and given by the lamps spectra as shown in Figure 54.

Furthermore, $E(\lambda) = \frac{hc}{\lambda}$

Where, h is the Planck constant (6.34E-34 J s/photon), c is the speed of light in a vacuum (3.00E8 m/s²) and λ is the wavelength in nm.

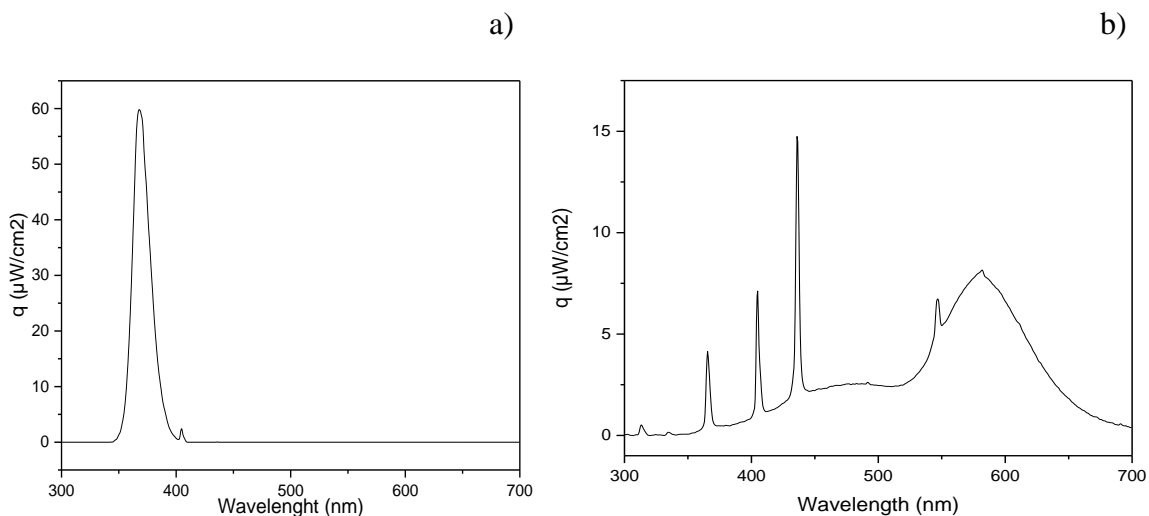


Figure 54 Lamps Irradiation spectrum: a) Near UV light, b) Visible light

Thus, for near UV light $q(\theta, z, \lambda, t) \Delta\lambda = 5.36\text{E-}19$ Einstein/s

$$E_{av} = \frac{\int_{\lambda_{min}}^{\lambda_{max}} I(\lambda) E(\lambda) d\lambda}{\int_{\lambda_{min}}^{\lambda_{max}} I(\lambda) d\lambda} = \frac{\int_{\lambda_{min}}^{\lambda_{max}} \frac{hc}{\lambda} * q(\theta, z, \lambda, t) \Delta\lambda}{\int_{\lambda_{min}}^{\lambda_{max}} q(\theta, z, \lambda, t) \Delta\lambda}$$

$$E_{av} = 5.36 \times 10^{-19} \text{J/mol photon} = 325.1 \text{ kJ/mol photon}$$

Same calculation was carried out for visible light where $q(\theta, z, \lambda, t) \Delta\lambda = 3.79\text{E-}19$ Einstein/s

$$E_{av} = 3.79 \times 10^{-19} \text{J/mol photon} = 274.5 \text{ kJ/mol photon}$$

Appendix B: Quantum Yield calculation

For photocatalytic processes the Quantum Yield (QY) efficiencies are established using the ratio of photogenerated radical molecules over absorbed photons. Specifically, QY% can be defined as the number of moles of hydrogen radical produced per absorbed photons on the photocatalyst surface. The above equation is used to its calculation:

$$\%QY = \frac{\left[\frac{dN_{H\cdot}}{dt}\right]}{Pa} \times 100$$

where $\frac{dN_{H\cdot}}{dt}$ represents the rate of moles of hydrogen radicals formed and Pa the moles of photons absorbed. According to the Irradiation Macroscopic Energy Balances (IMEB) in the Photo CREC Water Reactor II, Pa was calculated as follows:

$$P_a = P_i - P_{bs} - P_t$$

Where,

P_i is the rate of photons reaching the reactor at the inner surface, P_{bs} is the rate of back-scattered photons, and P_t is the rate of transmitted photons (Einstein s^{-1}).

The irradiation measurements were carried out using the fibre optic spectrometer StellarNet EPP2000-25 and applying the equations given in Chapter 5, the Pa values were determined.

A calculation sample is given below considering a hydrogen production rate of 0.2494 $\mu\text{mol}/\text{cm}^3 \text{ h}$ using 1.0wt% Pd-TiO₂, a photocatalyst concentration of 1.0 g/L, Ethanol at 2.0 v/v%, pH=4 \pm 0.05, UV Light, gas phase volume in the reactor of 5716 cm^3 and $Pa=2.57\text{E}-06$ Einstein/s.

$$QY_{H\cdot} = \frac{2 * (0.2494 \times 10^{-6} \text{ mol}/\text{cm}^3 \text{ h}) * (5716 \text{ cm}^3) * (6.022 \times 10^{23} \text{ photon}/\text{mol H}_2) * (1\text{h}/3600\text{s})}{2.57 \times 10^{17} \text{ photon}/\text{s}}$$

$$\%QY_{H\cdot} = 30.8\%$$

Curriculum Vitae

Name: Bianca Rusinque

Post-secondary Education and Degrees:

The University of Western Ontario
London, Ontario, Canada
2016-2018 MEng. Chemical Engineering

Universidad de America
Bogota, Colombia
2007-2015 B.A Petroleum Engineering

Universidad de America
Bogota, Colombia
2007-2013 B.A Chemical Engineering

Related Work Experience

Research/Teaching Assistant
The University of Western Ontario
2016-2018

Project Engineer
Aci Proyectos
2015-2016

Junior Project Engineer
Aci Proyectos
2014-2015

Trainee Development area
Cepsa Colombia
2013-2014

Trainee Research and Development
Carboquimica S.A.S
2011